Richness of dynamics and global bifurcations in systems with a homoclinic figure-eight

S.V. Gonchenko ‡, C. Simó † and A. Vieiro †
‡Institute of Applied Mathematics and Cybernetics, Nizhny Novgorod University, Russia
†Dpt. Matemàtica Aplicada i Anàlisi, Universitat de Barcelona, Spain

Abstract

We consider 2D flows having a homoclinic figure-eight to a dissipative saddle. We study the rich dynamics that such a system exhibits under a periodic forcing. First, we derive the bifurcation diagram using topological techniques. In particular, there is a homoclinic zone in the parameter space which has a non-smooth boundary. We provide a complete explanation of this phenomenon relating it to primary quadratic homoclinic tangency curves which end up at some cubic tangency (cusp) points. We also describe the possible attractors that exist (and may coexist) in the system. A main goal of this work is to show how the previous qualitative description can be complemented with quantitative global information. To this end, we introduce a return map model which can be seen as the simplest one which is "universal" in some sense. We carry out several numerical experiments on the model, to check that all the objects predicted to exist by the theory are found in the model, and also to investigate new properties of the system.

Dedicated to the memory of Leonid Pavlovich Shilnikov,
a Master whose works strongly influenced
the mathematical theory of dynamical systems.

1 Introduction

1.1 Homoclinic figure-eight: the statement of the bifurcation problem.

The bifurcation theory, as a mathematical science, was systematized in the 1930's due to the classical works of Andronov, Leontovich, Mayer, Pontryagin, Van der Pol, etc. At that time, based on the Poincaré idea to study dynamical systems up to topological equivalence, the fundamental notation of roughness (structural stability) of a dynamical system was introduced [1], the class of structurally stable dynamical systems on the plane was defined and principal, codimension 1, bifurcations were studied, see for more detail [2, 3] and references herein.

One of such famous bifurcations was the bifurcation of a limit cycle from a homoclinic loop to a saddle with $\sigma \neq 0$, where

$$\sigma := \gamma - \lambda, \quad \gamma > 0, \quad \lambda > 0, \tag{1}$$

is the sum of the unstable, γ, and stable, $-\lambda$, characteristic roots of the saddle. Andronov and Leontovich proved that if $\sigma \neq 0$, then exactly one limit cycle (asymptotically stable if $\sigma < 0$ and unstable if $\sigma > 0$) is born from the loop at its appropriate splitting, see Fig. 1.

From a physical point of view, such a bifurcation describes one of the main mechanisms for creation/destruction of self-oscillations. Other three main cases, for autonomous systems on the plane, are related to (i) the bifurcation of a double limit cycle, (ii) the Andronov-Hopf bifurcation

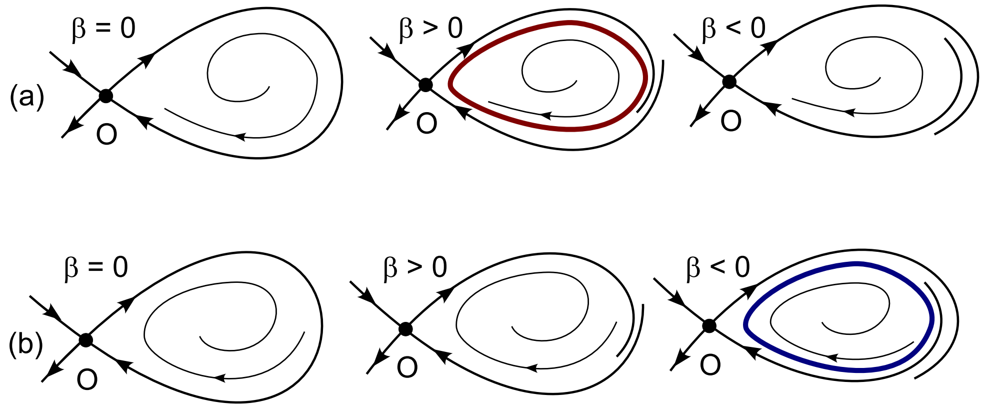

Figure 1: Scenarios giving rise to the bifurcation of a limit cycle from a homoclinic loop to a non-degenerate saddle point: (*a*) $\sigma < 0$; (*b*) $\sigma > 0$. The splitting parameter β accounts for the relative position of the invariant manifolds.

(birth of a limit cycle from a weak focus) and (iii) the Andronov-Vitt bifurcation[1] (birth of a limit cycle from a homoclinic loop of a saddle-node).

On the other hand, the study of bifurcations of saddle homoclinic loops has been one of the most popular problems in the qualitative theory because it is one of a series of famous dynamical problems where an exceptional value is related to changes in the number of limit cycles (it was addressed especially to the case $\sigma = 0$). The corresponding problem has been solved by Dulac [6] for analytical systems, by Leontovich [7, 8] for the smooth case and, independently, by Roussarie [9].

In this paper we study a two dimensional map $T_{\mu,\varepsilon}$, $\mu = (\mu_1, \mu_2)$, which can be seen as the Poincaré map of a non-autonomous (say, 2π-periodic in time) $\mathcal{O}(\varepsilon)$-perturbation of an autonomous family of vector field f_μ. The non-autonomous perturbation is assumed to be fixed and sufficiently small (equivalently, ε is a small given value). The family of systems f_μ is a 2-parameter unfolding of the system f_0, which we assume to posses a *homoclinic figure-eight* to a saddle point. In other words, the system f_0 has a saddle equilibrium O with $\sigma \neq 0$ whose stable and unstable invariants manifolds (separatrices) pairwise coincide, see Fig. 2 for an sketch. More precisely, let W^{u+} and W^{u-}, resp. W^{s+} and W^{s-}, be the two connected components (or branches) of $W^u \backslash O$, resp. $W^s \backslash O$. Our assumption for the flow f_0 means that W^{u+} coincides with W^{s+} and W^{u-} coincides with W^{s-}.

We denote by $\Gamma^+ = W^{u+} = W^{s+}$ and $\Gamma^- = W^{u-} = W^{s-}$ the homoclinic loops of the flow f_0 and then $\Gamma_0 = \Gamma^+ \cup \Gamma^-$ is the homoclinic figure-eight of the saddle O. Let $-\lambda$ and γ, as in (1), be the eigenvalues of the Jacobian matrix $Df_0|_O$ for f_0 in O. We assume the saddle value σ to be negative. This means that Γ_0 is a *locally asymptotically stable invariant set* of f_0. We can assume that Γ_0 is globally stable, i.e., Γ_0 is the global attractor (whose adsorbing domain is assumed to be quite large) of the system. Then two more equilibria, O_1 and O_2, exist inside the loops to be both asymptotically unstable (foci or nodes). The exact type of these points is not important for us. In the illustrations we will assume that both O_1 and O_2 are repulsive foci, see Fig. 2.

The bifurcations showing up in the 2-parameter unfolding f_μ of the figure-eight system f_0 were studied, in a more general context, which includes the multidimensional case when the unstable manifold of O is one-dimensional, by Turaev [10]. See also the references [11, 12, 13, 5]. For reader's convenience, we reproduce in Fig. 3 the typical bifurcation diagram for f_μ.

[1]This bifurcation was first discovered by Andronov and Vitt in their study of the Van der Pol equation with a small periodic force at a 1:1 resonance [4], see also [5] for more details.

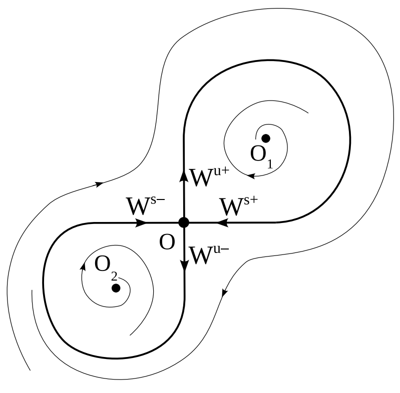

Figure 2: A homoclinic figure-eight to a saddle point with $\sigma < 0$.

The homoclinic figure-eight autonomous system became a very popular dynamical system for studying chaotic dynamics due to the presence of attractors in the system itself as well as in all close systems. For the family f_μ these attractors are simple: stable limit cycles which exist (and can coexist) for values of parameters from various open domains, see Fig. 3. However, non-autonomous perturbations of the figure-eight system exhibit different regimes of chaotic dynamics related to strange attractors.

A simple device that can be used physically to realize the figure-eight as seen in Fig. 2 can be as follows. Consider a conservative pendulum and take into account that the phase space is a cylinder. It is easy to see that compactifying the cylinder to $\mathbb{S}^2$ and doing a stereographic projection from the elliptic point, one obtains a figure like Fig. 2 without dissipation (see [22] for details). Then we can add dissipation to the pendulum, that can be assumed to be proportional to the velocity. If we want to add dissipation in an asymmetric way, it is enough to give the bulk different shapes in the left and right sides, to have different aerodynamic coefficients. But, of course, then the elliptic fixed point becomes a stable focus. To make it unstable we can proceed in the following way. Assume that the bulk contains a magnet and that the passages of the bulk through the minimum are detected by a photoelectric cell and a magnetic field is activated to kick the bulk. The kicks can be asymmetric, depending on the direction of the motion when passing through the minimum. This instabilizes the lower equilibrium point and tuning the intensity of the kicks one can either recover the separatrices or break them in the desired way.

The main goal of this paper is to study the global dynamics and the main bifurcations for small periodic perturbations of the flow f_0. We assume that these perturbations, analytical and actually small, include both autonomous and non-autonomous parts. Concerning the autonomous part, we embed our flow into a 2-parameter family f_μ of planar flows, where $\mu = (\mu_1, \mu_2)$ play the role of parameters which split independently the homoclinic loops Γ^+ and Γ^-, respectively. In other words, μ_1 and μ_2 are splitting parameters for the separatrices W^{s+}, W^{u+} and W^{s-}, W^{u-}, respectively. We analyze the system under a non-autonomous $\mathcal{O}(\varepsilon)$ periodic perturbation, where ε is assumed to be fixed but sufficiently small. For the non-autonomous system, we study the global dynamics and bifurcations for the time-2π Poincaré (stroboscopic) map $T_{\mu,\varepsilon}$.

There are, certainly, several papers devoted to the study of chaotic dynamics in systems under non-autonomous perturbations of various kinds: small, big, smooth, non-smooth or discontinuous (impulses), periodic, quasi-periodic, chaotic (from "white noise" to a "Bernoullian process"), etc. One can point out several works (not too many) that had a big influence in the qualitative theory of dynamical systems. The authors would like to propose the following list (which is not complete and has a subjective character): papers [14, 15, 16] deal with the global dynamics near a single homoclinic loop (see also the related papers [17, 18]); papers [19, 20, 21] about the passage through resonances and separatrices for Hamiltonian and nearly-Hamiltonian systems (see also the paper [22]), and the references [23, 24, 25] which focus on the dynamics of well-known systems like the forced damped Anti-Duffing oscillator.

A similar problem to the one considered in this paper, but with a figure-eight for a 3D flow instead, was studied in [26]. The case studied was a Shilnikov-Hopf scenario, with the branches of the unstable manifold of the periodic orbit created by Hopf bifurcation reinjecting near the stable manifold in a general non-necessarily symmetric way. A suitable return map to a Poincaré section formed by the union of two annuli was derived. But, under the assumption of strong dissipation, the model was approximated by a map of the union of two circles into itself. In the present study we keep the two annuli fundamental domain to display a very rich dynamics.

Nevertheless, as far as the authors know, a substantial qualitative analysis of non-autonomous perturbed systems having a dissipative ($\sigma < 0$) homoclinic figure-eight was not previously conducted. This paper, in particular, tries to fill such a gap in the literature while it proposes a systematic way to proceed, in this and similar problems, to a more quantitative analysis using (suitably adapted) semi-global return maps.

1.2 A description of the bifurcation diagram for the autonomous case

The planar autonomous system f_μ can be assumed to be, without loosing generality, of the form

$$\dot{x} \;=\; -\lambda x + P(x, y, \mu), \;\; \dot{y} \;=\; \gamma y + Q(x, y, \mu), \tag{2}$$

with λ and γ as in (1) and $\sigma < 0$. The functions P and Q vanish, as well as its first differentials DP, DQ, for $x = y = 0$. Moreover, we assume that for $\mu = 0$ the system possesses a figure-eight homoclinic to a saddle fixed point, see Fig. 2.

The parameters $\mu = (\mu_1, \mu_2)$ measure the distance between the separatrices of the figure-eight. The Fig. 3 displays the bifurcation diagram for f_μ according to the results in [10, 11, 12, 13, 5].

The μ_1 and μ_2-axes are related to the existence of homoclinic loops Γ^+ at $\mu_1 = 0$ and Γ^- at $\mu_2 = 0$. Then, the axes correspond to two bifurcation curves, $B^- : \{\mu_2 = 0\}$ and $B^+ : \{\mu_1 = 0\}$. On the other hand, two more bifurcation curves $B^\pm$ and $B^\mp$ exist. They correspond to those values of the parameters for which the flow f_μ has *big homoclinic loops*: the loop $\Gamma^\pm$ at $\mu \in B^\pm$ when the separatrices W^{u+} and W^{s-} coincide and the loop $\Gamma^\mp$ at $\mu \in B^\mp$ when W^{u-} and W^{s+} coincide. The curves $B^\pm$ and $B^\mp$ touch the curves B^- and B^+, for values of $\mu_1 < 0$ and of $\mu_2 < 0$ respectively, at $\mu = 0$.

These four bifurcation curves divide a neighborhood of the origin $\mu = 0$ into six open domains, where the system (2) is structurally stable. These domains are characterized, first of all, by their different set of (global) attractors, here asymptotically stable limit cycles. Such limit cycles will be denoted as C^+, C^- and C^*. They surround only the equilibrium O_1 (the upper or right one in Fig. 5), only the equilibrium O_2 (the lower or left one) and all equilibria O, O_1, O_2, respectively. These limit cycles can coexist for some domains of the parameters. So, C^+ and C^- coexist for $\mu \in$ IV, C^+ and C^* coexist for $\mu \in$ II and C^- exists together with C^* for $\mu \in$ VI.

The curves $B^\pm$ and $B^\mp$ are given by the equations, [10],

$$\begin{array}{ll} (a) \;\; B^\pm : \;\mu_1 = -\hat{A}^- \mu_2^{\gamma/\lambda}(1 + \dots), \;\; \mu_2 > 0, \\ (b) \;\; B^\mp : \;\mu_2 = -\hat{A}^+ \mu_1^{\gamma/\lambda}(1 + \dots), \;\; \mu_1 > 0, \end{array} \tag{3}$$

where $\hat{A}^-$ and $\hat{A}^+$ are some positive constants (called "separatrix values"). For completeness, we will show how to derive (3) for the case of the curve $B^\pm$ (the one for $B^\mp$ is derived analogously).

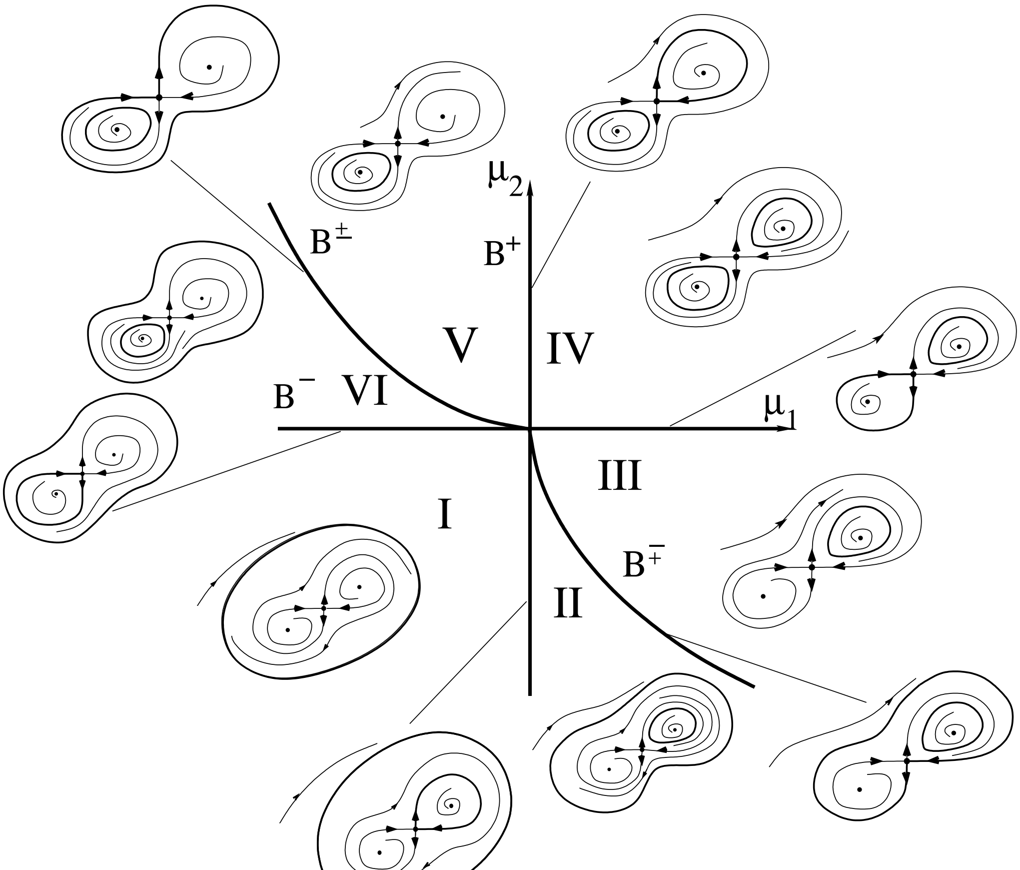

Figure 3: Sketch of the typical bifurcation diagram in the (μ_1, μ_2)-plane for a general 2-parameter family f_μ of flows near the original one having a homoclinic figure-eight at $\mu = 0$. The parameters $\mu = (\mu_1, \mu_2)$ are splitting ones. The two bifurcation curves $B^- : \{\mu_2 = 0\}$ and $B^+ : \{\mu_1 = 0\}$ correspond to the existence of *small homoclinic loops* Γ^+ at $\mu_1 = 0$ and Γ^- at $\mu_2 = 0$. Two more bifurcation curves $B^\pm$ and $B^\mp$ exist here which correspond to those values of μ for which the flow f_μ has *big homoclinic loops*: the loop $\Gamma^\pm$ at $\mu \in B^\pm$ when the separatrices W^{u+} and W^{s-} coincide and the loop $\Gamma^\mp$ at $\mu \in B^\mp$ when the separatrices W^{u-} and W^{s+} coincide.

The curve $B^\pm$ exists for $\mu_2 > 0$ and $\mu_1 < 0$ (i.e. when W^{u-} splits "inside" and W^{u+} "outside"), see Fig. 4. We assume, for simplicity, that the flow near O is linear, i.e. it has a form $\dot{x} = -\lambda x, \dot{y} = \gamma y$. We rescale coordinates, if necessary, and consider the points $(-1, 0) \in W^{s-}_{loc}$, $(0, -1) \in W^{u-}_{loc}$ and $(1, 0) \in W^{s+}_{loc}$, as well as the segments $Q_1 : \{x = -1, |y| \leq \delta_0\}$, $Q_2 : \{y = -1, |x| \leq \delta_0\}$ and $Q_3 : \{x = 1, |y| \leq \delta_0\}$. Then, W^{u-} intersects the segment Q_1 at the point $P_1(-1, -\mu_2)$ (by definition of μ_2) and, thus, W^{s-} intersects Q_2 at some point $P_2(A^-\mu_2, -1)$ (the nearest to $(0, -1)$). The coefficient A^- appears when transporting the distance μ_2, following the orbits of the flow, from P_1 to P_2. When the homoclinic loop $\Gamma^\pm$ exists, the points P_2 and $P_3 = W^{u+} \cap Q_3 = (1, \mu_1)$ belong to the same orbit. Using the first integral $x^\gamma y^\lambda$ at P_2 and P_3 and taking into account that $\mu_1 < 0, \mu_2 > 0$, we obtain equation (3)(a) for the curve $B^\pm$.

1.3 Contents and main results

We consider the figure-eight system under a fixed non-autonomous periodic $\mathcal{O}(\varepsilon)$-perturbation (or, equivalently, the Poincaré map $T_{\mu,\varepsilon}$) and we study the bifurcations taking place giving a description of the parameter space from both qualitative and quantitative points of view. The transitions between different dynamics are also analyzed and various attractors, including different

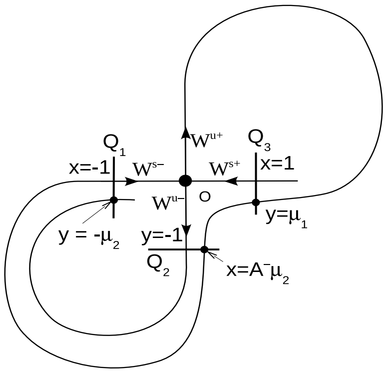

Figure 4: The phase space geometry for points in the curve $\Gamma^{\pm}$.

strange attractors, are identified. To this end we combine qualitative and analytic methods. Some illustrations and accurate quantitative descriptions are produced using numerical tools.

First, we focus on the *qualitative* description of the dynamics. To put the bifurcation problem for $T_{\mu,\varepsilon}$ into a suitable framework we might consider (implicitly) a family of systems of the form

$$\begin{aligned} \dot{x} &= -\lambda x + P(x,y,\mu) + \varepsilon p_1(x,y,t,\varepsilon), \\ \dot{y} &= \gamma y + Q(x,y,\mu) + \varepsilon q_1(x,y,t,\varepsilon), \end{aligned} \tag{4}$$

where the functions P, Q, DP, DQ vanish at $x = y = 0$ and the functions p_1 and q_1 are 2π-periodic in t. For $\varepsilon = 0$ we recover (2) which at $\mu = 0$ behaves as shown in Fig. 2. As mentioned, we assume that $\mu = (\mu_1, \mu_2)$ are control parameters which split independently the invariant manifolds. Generically, the bifurcation diagram for (2) on the μ-plane near the origin will be such as in Fig. 3. However, when we consider the whole family (4) the bifurcation diagram (for the corresponding Poincaré map $T_{\mu,\varepsilon}$ and for any small enough fixed ε) becomes much more complicated.

In Fig. 5 we show a sketch of a fragment of the bifurcation diagram for $T_{\mu,\varepsilon}$ in a neighborhood of the origin of the μ-plane (for sufficiently small and fixed ε). When $\varepsilon = 0$ the bifurcation diagram for $T_{\mu,0}$ coincides, evidently, with the flow diagram of Fig. 3. Only equilibria, limit cycles and separatrices should be changed to fixed points, closed attracting invariant curves and invariant (stable and unstable) manifolds, respectively. The latter can split in a non-trivial way when varying ε and, hence, Poincaré homoclinic structures generically appear. In Section 3 we construct (using qualitative methods) this bifurcation diagram and explain its main elements and the related homoclinic bifurcations.

At a first glance, comparing the bifurcation diagram for $T_{\mu,\varepsilon}$ in Fig. 5 with the one for f_μ in Fig. 3, the familiarized reader can easily recognize most of the expected elements in the parameter space. Each of the bifurcation curves B^a (either with $a = +, -, \pm$ or $\mp$) where the separatrices of f_μ coincide gives rise to a homoclinic zone HZ^a of size $\mathcal{O}(\varepsilon)$. These homoclinic zones are characterized by the fact that, for parameter values inside the zone, the fixed point O has homoclinics and, generically, the invariant manifolds $W^s(O)$ and $W^u(O)$ intersect transversally. More precisely, keeping ε fixed, if $\mu \in HZ^-$, then $W^{s-}(O) \cap W^{u-}(O) \neq \emptyset$; if $\mu \in HZ^+$, then $W^{s+}(O) \cap W^{u+}(O) \neq \emptyset$; if $\mu \in HZ^{\pm}$, then $W^{u+}(O) \cap W^{s-}(O) \neq \emptyset$; and if $\mu \in HZ^{\mp}$, then $W^{u-}(O) \cap W^{s+}(O) \neq \emptyset$.

In general, the bifurcation diagram for $T_{\mu,\varepsilon}$ contains, for every small and fixed ε, 35 open regions, see Fig. 5, corresponding to different dynamical regimes. Note that only six regions (**23**, **35**, **29**, **7**, **4** and **1**) relate to simple dynamics. We label these regions also by the Roman numerals I, II, III, IV, V and VI, the same as in Fig. 3, emphasizing that the map $T_{\mu,\varepsilon}$ possesses here simple dynamics which mimics the corresponding flow dynamics. In particular, the map $T_{\mu,\varepsilon}$ has closed

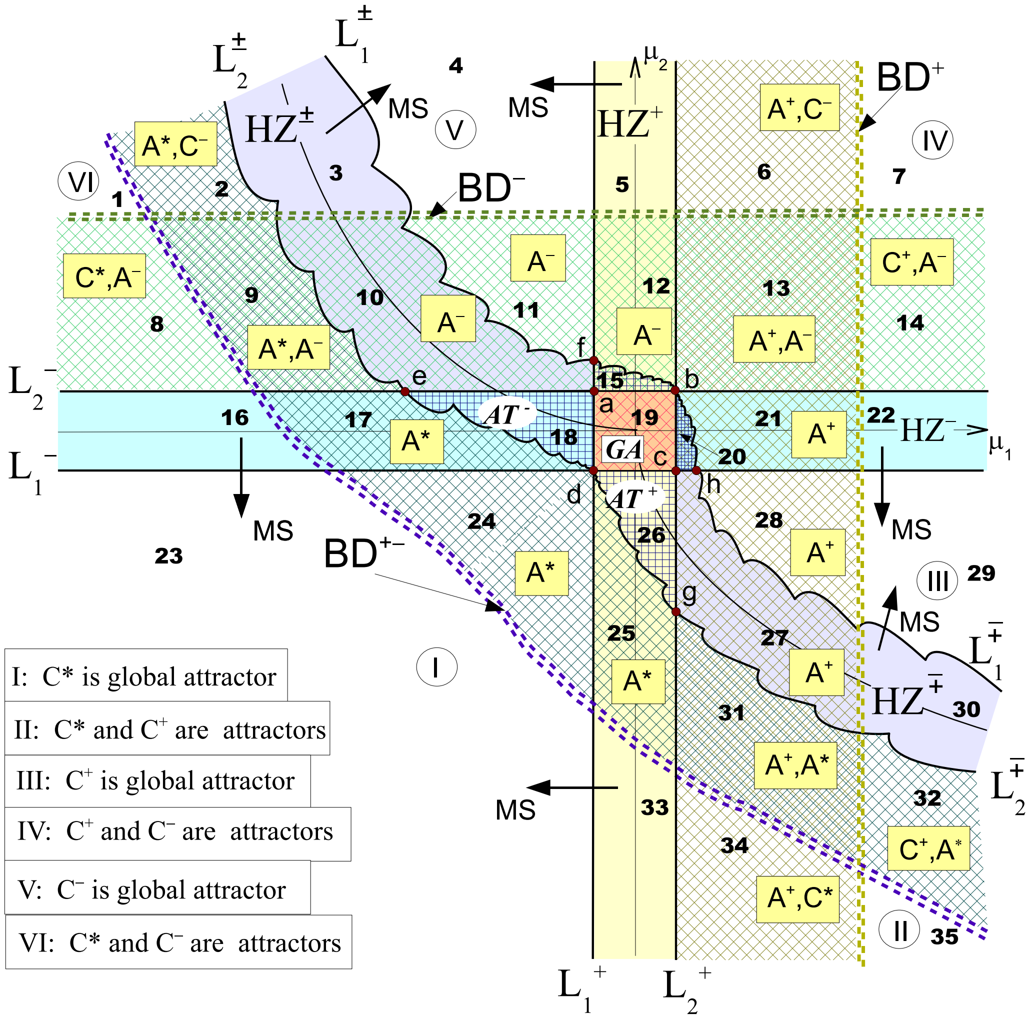

Figure 5: A sketch of the bifurcation diagram for the Poincaré map $T_{\mu,\varepsilon}$ on the μ-parameter plane at small and fixed ε. For a more detailed description of the related dynamics see Section 3.

invariant curves C^+, C^- or C^* as global attractors (see Fig. 5 and the labels at the bottom-left corner), either with quasi-periodic or periodic dynamics.

The other regions in Fig. 5 are related to possible chaotic dynamics. The closure of one of the branches of the unstable manifold (or of both branches) can contain a *quasi-attractor*, i.e., a nontrivial attracting invariant set which contains stable periodic orbits (sinks) and/or strange attractors SA (either made by a single piece or several pieces). Arbitrarily small perturbations of the parameters when a SA is found can give rise to sinks. The sinks create windows of stability and, thus, if the period is not very high, chaotic regimes can be seen (visually) to alternate with periodic ones. We have counted 6 main types of global SA which are marked as $A^+, A^-, A^*, AT^+, AT^-$ and GA. The attractors (or quasi-attractors) A^+, A^- and A^* are of "torus-chaos" type, since they are born under the break-down of the closed invariant curves C^+, C^- and C^*, respectively. The global attractors (quasi-attractors) AT^+, AT^- and GA have another nature: they can be labeled as "homoclinic attractors", since their appearance is connected with the creation of various types of homoclinic intersections of the invariant manifolds of the saddle O. So, GA exists for values of the parameters from the domain **19** in Fig. 5 where all the homoclinic zones intersect and, thus, every component W^{u+} and W^{u-} of W^u intersects with both components W^{s+} and W^{s-} of W^s. In this case, $GA \subseteq \overline{W^{u+}} = \overline{W^{u-}}$. Regions **18** and **26** are the existence regions for AT^- and AT^+, respectively. Here, exactly one pair of the connected components from $W^u\backslash O$ and $W^s\backslash O$ does not intersect: $W^{u+} \cap W^{s+} = \emptyset$ in the case of AT^- and $W^{u-} \cap W^{s-} = \emptyset$ in the case of AT^+, see Fig. 12 and Section 3 for details.

As one can see in Fig. 5, the boundaries $L^{\pm}_{1,2}$ and $L^{\mp}_{1,2}$ of the homoclinic zones $HZ^{\pm}$ and $HZ^{\mp}$ look to be more complicated comparing with the boundaries of the homoclinic zones HZ^+ and HZ^-. Some numerical computations using the model (5), to be introduced later in Section 2, show that $L^{\pm}_{1,2}$ and $L^{\mp}_{1,2}$ have a form of kinked curves with many steps. In Section 4 we prove that these curves are C^0 and have infinitely many steps (intervals of smoothness) which accumulate to the points `b` and `d` of the rectangle **19** of Fig. 5. The latter points `b` and `d` as well as the points `a,c,e,f,g` and `h` of Fig. 5 correspond to the existence of specific double primary homoclinic tangencies, see Fig. 13 below. The non-smoothness points on $L^{\pm}_{1,2}$ and $L^{\mp}_{1,2}$ also correspond to double primary homoclinic tangencies of other types. Every such a point is the intersection of two bifurcation curves of different quadratic homoclinic tangencies. We shall show that the latter curves finish at some points within $HZ^{\pm}$ (or $HZ^{\mp}$) and are related to cubic homoclinic tangencies of the invariant manifolds of O. Studying also the accompanying homoclinic bifurcations we prove the existence of infinite series of codimension 2 points corresponding to cubic and double quadratic homoclinic tangencies of O. See details in Section 4.

Up to this point, we have summarized the main qualitative results in this paper. Nevertheless, the paper also includes other results which fit within a more quantitative approach to the problem. Certainly, the qualitative results give a satisfactory theoretical explanation to the bifurcation problem. However, for real applications one needs to complement these results with information concerning questions like the ones we list below. Note that answers to these questions require techniques which are beyond the traditional topological description of the qualitative theory of dynamical systems. Some examples of quantitative questions related to our problem are the following.

1. The presence of cubic tangencies (and the associated cusp points) is related to the existence of (saddle, spring, cross-road, dovetails,...) areas of stability, see [27, 28, 17] (see also the Appendix A for the cases that appear in our problem). Which type of configurations are expected in the problem? Which is the size of the corresponding areas of stability? Are all of them relevant in the phase space or they just appear in a very tiny domain?
2. Crossing a last tangency line we find a zone where we expect to have strange attractors alternating with sinks. These zones have a "boundary line" BD^a ($a = +, -, +-$) in Fig. 5. Which is the size of these zones and which is the form of such boundaries?
3. Inside the regions bounded by the "bifurcation lines" BD^a we expect to find strange attractors together with sinks. Which is the abundance of SA within these zones?
4. There are different zones of parameters where different attractors coexist. Which is the probability of capture for each attractor? How the basins of attraction evolve as the parameters change?

Let us state, honestly, that our results are far from giving a complete answer to all the proposed questions. At most we provide partial answers to some of them. However, the idea of a more quantitative approach made us to develop a different approach to the bifurcation problem based on what can be named the *dissipative double separatrix map*, which generalizes the well-known separatrix map [29, 30, 14] but it is suitably adapted to the study of the figure-eight system $T_{\mu,\varepsilon}$ and to dissipation. The model is introduced in Section 2, where we give a simple numerical overview of the bifurcation problem, and it is used extensively in Section 5 to provide quantitative information on the problem. It gives also valuable information on some dynamical mechanisms that should play a role in similar problems. It must also be said that the study of model (5) was the seminal point of the present paper.

2 A dissipative figure-eight separatrix model

Most of the parts of the present paper deal with the topological description of the bifurcation diagram of $T_{\mu,\varepsilon}$ for a fixed ε small enough. In general, this type of qualitative approaches provides a complete map of the possible dynamics of a system, and hence it is extremely useful to understand the system theoretically. However, this description might be completely useless in real applications unless it is complemented with quantitative data concerning the set of the parameter space where some dynamics appears and the real influence of such a dynamics on the domain of the phase space where we study the system.

In this section we introduce a simple universal model to study the dynamics of a two-dimensional diffeomorphism with a double homoclinic loop. The model consists on a suitable return (semi-global) map and below we use it to describe the set of bifurcations of the figure-eight. The models obtained in this way, i.e., as return maps, have one remarkable peculiarity: they are not very sensitive to concrete details of the initial system, that is, the model is obtained having into account that, mainly, it is the character of the perturbations (both, the autonomous one and the final non-autonomous one) what determines the dynamics of the system. Therefore, the study of one model can help to observe dynamical properties of a wide class of systems. The maps obtained are, hence, universal models which depend on some relevant parameters of the system.

The model we consider is given as

$$M_{a,b,\psi,A,\omega} : \begin{pmatrix} z \\ \eta \\ s \end{pmatrix} \mapsto \begin{pmatrix} z + \omega_j + A\log(|y|) \\ \mathrm{sign}(y)|y|^{\psi} \\ \mathrm{sign}(y)s \end{pmatrix}, \tag{5}$$

where $y = a_j + \eta + b_j \sin(2\pi z)$ and the index j takes the value 1 if $s = 1$ and the value 2 if $s = -1$.

The map (5) is similar to the so-called separatrix map [29, 30] defined on a figure-eight homoclinic loop [31, 22, 32]. It is defined on a fundamental domain FD which is the union of two annular domains, one in the upper part of the figure-eight and another in the lower part. In these domains the part of the unstable manifold is parametrized by $z \in [0, 1)$. The variable η measures the position with respect to the corresponding unstable branch of W^u, while y measures the distance with respect to W^s. Both for η and y in the upper and lower domains the positive orientation points towards the saddle. We are taking the simplifying assumption that the position of the branches of W^u with respect to W^s is given by $a_j + b_j \sin(2\pi z)$, where $j = 1$ ($j = 2$) is used for the upper (lower) part. For instance, a point in the upper part of the fundamental domain, such that it gives $y > 0$, returns to the upper part.

The role of the exponent ψ is clear. It accounts for the passage near the dissipative saddle. If the eigenvalues (for the discrete map) are $\exp(\gamma), \exp(-\lambda)$ ($\lambda > \gamma > 0$), see (1), then it is immediate to obtain $\psi = \lambda/\gamma$ using a simple approximation as the time 1-map of a linear flow near the saddle.

For $\psi = 1$ and $a_j = 0$, the map (5) reduces to the well-known separatrix map [29, 30] defined on the figure-eight [31, 22] for the conservative case.

The variable z increases according to the sense of the dynamics on the manifolds: $T_{\mu,\varepsilon}$ maps a point with $z = 0$ to a point with $z = 1$. The parameters a_j measure the relative distance between the averaged invariant manifolds due to the perturbative effects. The values b_j can be seen as the amplitudes of the splitting of the invariant manifolds when $a_j = 0$. For simplicity we have used only one harmonic in the "undulation" of the splitting, but this is also justified if the dynamics is slow, see [33]. If $a_j = b_j = 0, j = 1, 2$, the stable and unstable branches of the upper and lower parts of the figure-eight coincide. If $b_j = 0, j = 1, 2$, we should have a map that mimics the behavior of the vector field when we perturb from the figure-eight. To relate b_1, b_2 to ε one can consider $b_1 = \varepsilon B_1, b_2 = \varepsilon B_2$ with B_1, B_2 normalized as $B_1^2 + B_2^2 = 1$ and ε small.

The constant A is related to the flight time close to the saddle. As we shall consider small values of $|\eta|$ and $|y|$ the term $\log(|y|)$ in the expression of the value of z in the image is negative. Hence, the coefficient A will be taken also as negative, to keep the increasing sense of z. The variable z can be seen as a time, which increases by 1 unit in the original map, but the map that we consider here is the return map to one of the fundamental domains. The returning time consists of a constant part, ω_j (that can be taken modulo 1) and a "flying time" near the saddle, which is of the form $A \log(|y|)$ (see Appendix A of [17]). In the simulations we shall use $\omega_j = 0, j = 1, 2$.

2.1 Admissible ranges of the parameters a_1 and a_2

We briefly recall from the Introduction that our goal is to study the parameter space of a family of planar maps $T_{\mu,\varepsilon}$. To this end we fix ε and look for the 2-parameter space in μ. For $\varepsilon > 0$, the invariant manifolds forming the figure-eight for $T_{\mu,\varepsilon}$ at $\mu_1 = \mu_2 = 0$, generically no longer coincide (for conservative maps ε is a "distance-to-integrable" parameter, see [22] for a suitable definition). Hence, roughly speaking, the role of ε is to create the homoclinic lobes. This is reflected by the parameters b_1 and b_2 in (5), which measure the amplitude of the homoclinic lobes (if $a_1 = a_2 = 0$). On the other hand, the role of the splitting parameters μ_1, μ_2 is played in the model (5) by a_1, a_2, respectively.

Since a_1, a_2 are unfolding parameters they are assumed to be small enough. One of the advantages in using a model like (5) is that we can obtain quantitative information of the maps $T_{\mu,\varepsilon}$. It is important to examine how large a_1, a_2 can be in order to recover the properties of (2) when $\varepsilon = 0$. Furthermore, we should take b_1, b_2 also small: the passage near O is assumed to be well approximated by a linear flow.

As $\psi > 1$, the passage near the saddle should give a contraction, the image value of $|\eta|$ being smaller than $|y|$. This requires $|y| < 1$ in all the iterates. Let us see also which conditions on the values of a_j follow if for $b_j = 0$ we should recover the dynamics of a flow.

We consider the case of a_1, the one of a_2 being similar. If $a_1 > 0, b_1 = 0$ (that is, W^s is on top of W^u on the upper part and no oscillations occur), we should look for $\eta > 0$ such that $\eta = (a_1 + \eta)^\psi$. The attracting invariant curve C^+ of the regions II, III and IV of Fig. 3 will be found as a graph over z with constant value.

For a_1 small it is clear that a solution with η small exists. Of course, another solution with $\eta \approx 1$ exists if a_1 is close to zero. One has to prevent that the solutions disappear in a double zero. This is a common solution of

$$\eta = (a_1 + \eta)^\psi \quad \text{and} \quad 1 = \psi(a_1 + \eta)^{\psi - 1},$$

from which it follows

$$\eta = \frac{1}{\psi}(a_1 + \eta), \quad \eta = \frac{a_1}{\psi - 1}.$$

Replacing in the initial equation

$$\frac{a_1}{\psi-1}=\left(a_1+\frac{a_1}{\psi-1}\right)^{\psi}=\left(\frac{\psi a_1}{\psi-1}\right)^{\psi}.$$

From last equalities it follows

$$a_1=\frac{\psi-1}{\psi^{\frac{\psi}{\psi-1}}},$$

which gives an upper bound for the admissible values of a_1. In fact, it is advisable not to be too close to that value. We want that the iterates pass close to O.

In a similar way we can consider the condition for existence of an invariant curve C^* surrounding the eight. This curve has to be seen as the graph of constant functions in both fundamental domains. Let $\eta_1<0,\eta_2<0$ be the corresponding values of η in each domain. We consider the case $a_1<0,a_2>0$ (region VI of Fig. 3), the others being similar. We recall that the boundary of the domain should be obtained when the upper branch of W^u is mapped to the lower branch of W^s. That is $a_2=(-a_1)^{\psi}$.

The condition for a surrounding curve is

$$\eta_2=-(-a_1-\eta_1)^{\psi},\quad \eta_1=-(-a_2-\eta_2)^{\psi},$$

or, introducing $w=-\eta_1>0$,

$$H(w):=(w-a_1)^{\psi}-a_2-w^{1/\psi}=0.$$

It is clear that $w=0$ at the boundary of the domain $a_2=(-a_1)^{\psi}$. Assume now that we fix a value of $a_1<0$. To look for the zeros of H it is enough to consider the graph of $h(w)=(w-a_1)^{\psi}-w^{1/\psi}$ and intersect: $h(w)=a_2$. As $dh/dw<0$ when w is close to zero and

$$d^2h/dw^2=\psi(\psi-1)(w-a_1)^{\psi-2}+\frac{\psi-1}{\psi^2}w^{\psi^{-1}-2}$$

is positive, it follows that $H(w)=0$ will have a solution provided a_2 is not below the minimum of h. As we want to have solutions for the domain $a_2\in(0,(-a_1)^{\psi})$, to find the maximum admissible value for $|a_1|$ we ask H to have a double zero for $a_2=0$, which is equivalent to $w=(w-a_1)^{\psi^2}$ having a double zero. This condition is similar to the one encountered before for the existence of the curve C^+ for $a_1>0$, but with ψ replaced by ψ^2. Hence, the condition for the lower bound of a_1 is

$$-a_1=\frac{\psi^2-1}{(\psi^2)^{\frac{\psi^2}{\psi^2-1}}}.$$

But, in fact, we want to be able to continue the existence of this outer curve in the domain $a_1,a_2<0$. As before, we keep the value of a_1 fixed and require the minimum of h to be less of equal than a_1. For the remaining part of this quadrant the roles of a_1 and a_2 can be exchanged. But if in the condition for the surrounding curve curve we put $a_2=a_1$ we obtain the same condition found for the invariant curves confined either to the upper part or to the lower part, except by the change of sign in a_1.

Summarizing, we have proved the following lemma.

Lemma 2.1. *The admissible domain for a_1, a_2 to recover the qualitative behavior of the flow case when $b_1 = b_2 = 0$ is given by $|a_1| < M, |a_2| < M$, where*

$$M = \frac{\psi - 1}{\psi^{\frac{\psi}{\psi-1}}}.$$

Remark. We note that $M \to 0$ as $\psi \to 1^+$ as expected because one approaches the conservative case.

2.2 A preliminary numerical exploration of model (5)

We start by computing the bifurcation diagram from model (5) in the (a_1, a_2)-plane. We will see that some homoclinic zones have an unexpected boundary shape. Here we show these boundaries and some related bifurcation curves as a motivation to the qualitative analysis of the problem. Later, in Section 5 we will study in detail the dynamics of the model (5) and we will provide precise quantitative information based on the qualitative description of Sections 3 and 4.

For concreteness, we consider through the text $b_1 = 0.003$, $b_2 = 0.0015$, $\psi = 1.6$, $A = 2$ and $\omega_1 = \omega_2 = 0$. From Lemma 2.1 it follows that $|a_1|, |a_2| \leq M \approx 0.17$ define an admissible domain. Note that we are using $A > 0$ instead of $A < 0$ as explained before. This is irrelevant because it is equivalent to a change in the orientation of z.

First, we compute the bifurcation curves which correspond to first and last homoclinic tangencies between the invariant manifolds. For simplicity we label the bifurcation curves for the model as their analogous in Fig. 5. The expressions for the local invariant manifolds in the fundamental domain of definition of (5) are $W^{u\pm} = \{\eta = 0, s = \pm 1\}$ and $W^{s\pm} = \{y = 0, s = \pm 1\}$. The condition for a primary homoclinic tangency between W^{u+} and W^{s+} (resp. between W^{u-} and W^{s-}) is $|a_1| = b_1$ (resp. $|a_2| = b_2$). Hence this condition defines two vertical (resp. horizontal) lines L_1^+ and L_2^+ (resp. L_1^- and L_2^-) bounding a homoclinic strip HZ^+ (resp. HZ^-) in the (a_1, a_2)-parameter space. See Fig. 6 left.

On the other hand, we look for primary homoclinic tangencies between W^{u+} and W^{s-}, and between W^{u-} and W^{s+}. Assume that we start from a point on W^{u+} (resp. W^{u-}) with coordinates $(z_0, 0, 1)$ (resp. $(z_0, 0, -1)$). The conditions for a quadratic tangency between W^{u+} and W^{s-} (resp. between W^{u-} and W^{s+}) are

$$y_1 = 0, \quad dy_1/dy_0 = 0,$$

where

$$y_1 = a_j + \eta_1 + b_j \sin(2\pi z_1), \quad \eta_1 = -(-y_0)^{\psi}, \quad y_0 = a_k + b_k \sin(2\pi z_0), \quad z_1 = z_0 + A\log(|y_0|)$$

and $j = 1$, $k = 2$ (resp. $j = 2$, $k = 1$). These conditions define several lines in the bifurcation diagram corresponding to primary quadratic tangency lines. The envelope of these curves can be easily computed numerically by using a continuation method. We obtain two curves $L_1^{\pm}$ and $L_2^{\pm}$ (resp. $L_1^{\mp}$ and $L_2^{\mp}$) which correspond to the first and last homoclinic tangencies between W^{u+} and W^{s-} (resp. between W^{u-} and W^{s+}) respectively. These two curves bound a "diagonal" homoclinic strip $HZ^{\pm}$ (resp. $HZ^{\mp}$), see Fig. 6 left. Some of the details of the curves $L_1^{\pm}$ and $L_2^{\pm}$ can be observed in Fig. 6 right. Surprisingly, the boundary of the homoclinic zone is not given by a smooth curve and, instead, a "stair" structure is observed. The reason why this behavior appears will be given in Section 4.

It turns out that $L_1^{\pm}$, $L_2^{\pm}$, $L_1^{\mp}$ and $L_2^{\mp}$ are obtained by joining different segments of bifurcation curves corresponding to different primary quadratic tangencies. To understand this structure we

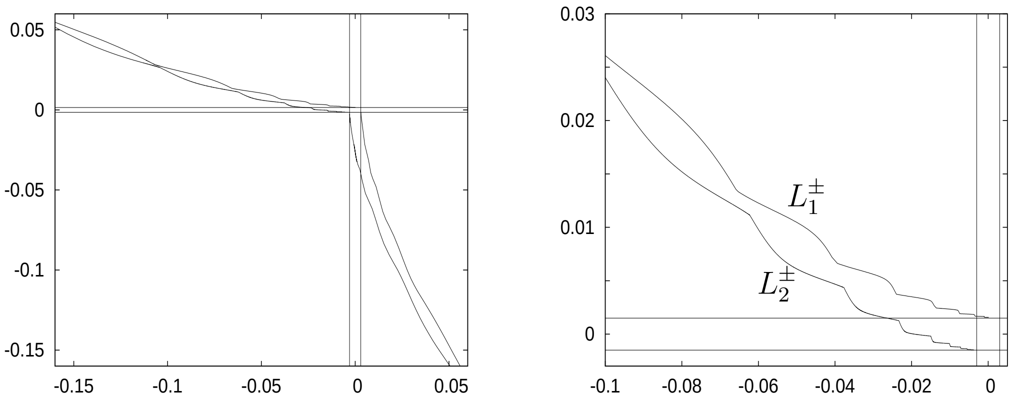

Figure 6: Bifurcation curves corresponding to first and last tangencies. They bound different homoclinic strips in the parameter space (a_1, a_2). Right plot is a detail of the boundary of the homoclinic zone $HZ^{\pm}$.

focus on the zone $HZ^{\pm}$ and we look for the curves of primary quadratic tangencies which form the boundary of $HZ^{\pm}$. They are shown in Fig. 7.

We observe in Fig. 7 a complicated structure of different pieces which accumulate to the limit rectangle which bounds the region $HZ^{+} \cap HZ^{-}$. The different pieces are interrelated and form a kind of "chain" structure which is responsible of the "stair" structure of the boundary of $HZ^{\pm}$. As we can see in the right magnifications, different cusp points play a role in the structure. They are related to cubic tangencies, see Section 4.2. Moreover, these cusp points accumulate to two of the vertices of the limit rectangle.

Next, we look for other quadratic tangency bifurcation curves inside the pieces shown in Fig. 7 second row left. The results are shown in Fig. 8. The additional curves inside the pieces show new cusp points which are also involved in the inner structure of the zone $HZ^{\pm}$. These cusp points accumulate to the other two vertices of the limit rectangle. However, as it can be observed, in the left "link" of the "chain" shown in Fig. 8 we have not obtained any inner bifurcation curve: they start on the link located around $a_1 = -0.02$.

As far as the authors know, this structure of the boundary of a homoclinic zone has not been previously observed in any example. For this reason, the next two sections are devoted to give a more complete qualitative description of the bifurcation diagram and to study in detail the "stair" structure of such a boundary curves, respectively. After this qualitative approach in Section 5 we will consider again the model (5) to provide a more quantitative description of the parameter space.

3 On the structure of the bifurcation diagram on the μ-plane at small periodic perturbations: a preliminary discussion.

Consider now the system (4), which is a periodically forced version of system (2). As it is well-known, the dynamics and bifurcations of such non-autonomous systems for small ε can be analyzed by means of the time-2π Poincaré map which we denote as $T_{\mu,\varepsilon}$.

In this section we give a very rough picture of the "qualitative orbit structures", typical for $T_{\mu,\varepsilon}$ at small ε and μ. For definiteness, we fix ε and consider μ_1 and μ_2 as governing parameters. Despite the bifurcations depend on ε we skip the explicit mention to ε through the study.

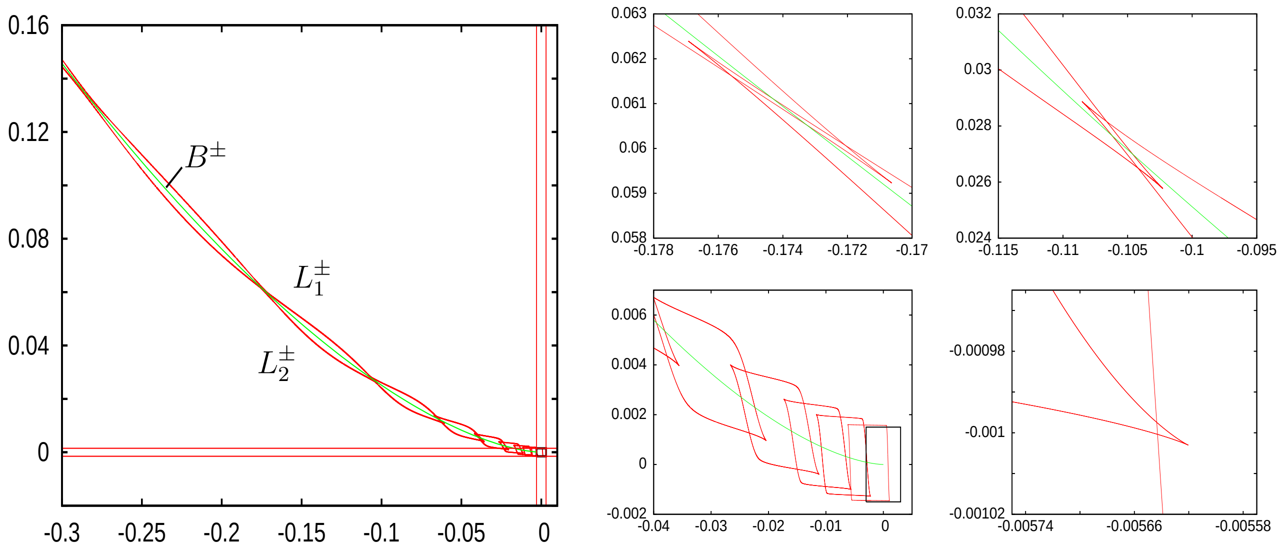

Figure 7: The red lines are bifurcation curves in the (a_1, a_2)-parameter space which correspond to primary quadratic tangencies that form the curves $L_1^{\pm}$ and $L_2^{\pm}$. The right figures are magnifications of the left figure. The green line corresponds to the bifurcation curve of the autonomous limit case. The black rectangle in the figure of the second row left corresponds to the intersection of the homoclinic zones HZ^+ and HZ^-. Note that on the left plot the range of $|a_1|$ exceeds the maximum admissible value M. The purpose has been to illustrate the shape of the boundaries.

Remark. One can think, in an equivalent way, that the system has a three dimensional parameter space $(\mu_1, \mu_2, \varepsilon)$ and we look at an slice $\varepsilon = \varepsilon_0$. In any case, for small ε the bifurcation diagram will be qualitatively similar to the one shown in Fig. 5. Note, however, that the sizes of the homoclinic zones grow, in general, when $|\varepsilon|$ grows.

All the homoclinic zones $HZ^-, HZ^+, HZ^{\pm}$ and $HZ^{\mp}$, mentioned in Section 1.3 intersect in a rectangle surrounding the origin of the μ-plane: the *chaotic zone* labeled GA in the Fig. 5. For $\mu \in GA$ all the branches of the invariant manifolds of O have intersections and, thus, the well-known structure of a “figure-eight chaos” similar to that appearing in periodic perturbations of conservative systems (such as the Duffing equation [23]) shows up. However, the system under consideration exhibits other limit (regular and chaotic) regimes that we try now to describe. Some of these regimes were previously observed numerically for the model (5), see Fig. 37. Here we give a qualitative description.

Let us consider Fig. 5 in detail. As shown in the figure, there are 11 principal bifurcation curves: 8 of them are curves of “first” and “last” homoclinic tangencies of manifolds of O and other 3 are certain fractal “curves” corresponding to a transition from a simple big attractor (usually a closed invariant curve) to a strange one. We enumerate these curves and “curves”.

1-2 L_1^+ (and L_2^+) are the curves of the first (and last) homoclinic tangency of W^{u+} and W^{s+}, see Fig. 9 c) and j) (and Fig. 9 d) and i)).

3-4 L_1^- (and L_2^-) are the curves of the first (and last) homoclinic tangency of W^{u-} and W^{s-}, see Fig. 9 b) and g). (and Fig. 9 a) and h)).

5-6 $L_1^{\pm}$ (and $L_2^{\pm}$) are the curves of the first (and last) homoclinic tangency of W^{u+} and W^{s-}, see Fig. 9 k) (and Fig. 9 l)).

7-8 $L_1^{\mp}$ (and $L_2^{\mp}$) are the curves of the first (and last) homoclinic tangency of W^{u-} and W^{s+}, see Fig. 9 f) (and Fig. 9 e)).

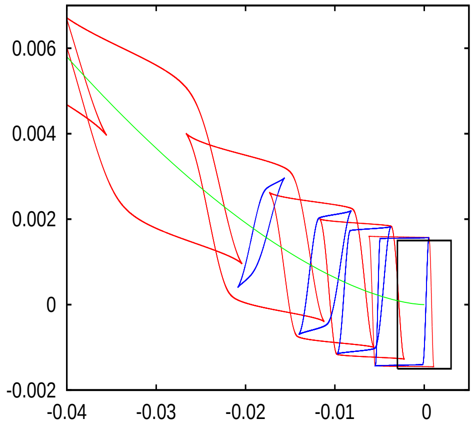

Figure 8: Detail of the bifurcation curves inside the homoclinic zone $HZ^{\pm}$. The figure corresponds to the Fig. 7 second row left. Note that inside the left "link" of the "chain" structure there is not a bifurcation curve related to a primary quadratic tangency fully contained in it. In contrast, the remaining "links" from the right contain such a curve.

9-11 We add into consideration also three more bifurcation "curves" BD^+, BD^- and BD^{+-}. They are some (possibly) fractal boundaries corresponding to a transition from simple attractors to strange ones. Such a transition goes through the break-down of the closed invariant curves C^+, C^- and/or C^*. After crossing these boundaries, strange attractors A^+, A^- and A^{+-} and/or periodic sinks appear for some values of the parameters. [2]

In general, these 11 curves divide the μ-plane into 35 open regions. For μ in the regions I, II, III, IV, V and VI (numbered also as regions **23, 35, 29, 7, 4, 1**, respectively) the map $T_{\mu,\varepsilon}$ has a simple dynamics which mimics the dynamics of the autonomous flow (2) for the corresponding regions in Fig. 3. On the other hand, the dynamics of $T_{\mu,\varepsilon}$ can be chaotic for some of the values of μ in the other regions. Moreover, for values of the parameters from the dashed regions, sinks and different kinds of SA can exist (and coexist).

The homoclinic zones and their boundaries play a key role to understand the dynamics of $T_{\mu,\varepsilon}$ even for values of μ outside these zones. Generally, we can select two types of homoclinic zone boundaries: 1) *MS-boundaries* and 2) *SA-boundaries.*

The MS-boundaries correspond to the existence of a type of homoclinic tangency which is called "first" tangency, or tangency "from below", or tangency of the first class, see Fig. 10 (b) (and compare it with Fig. 9 (b),(c),(e),(g),(j),(k) in which various cases with such a tangency type are shown for $T_{\mu,\varepsilon}$). The system with such a tangency can belong to the boundary of Morse-Smale systems and then the corresponding homoclinic bifurcations lead to a type of homoclinic Ω-explosion [34, 35, 36, 37, 38]. The trivial dynamics of the systems before the bifurcation moment (of homoclinic tangency creation) becomes immediately complicated after it, e.g., infinitely many Smale horseshoes are born as soon as the tangency splits into two (transverse) homoclinics. Geometrically, it may be clarified by Fig. 10. In Fig. 5, we mark by MS-arrows the corresponding transitions (in direction from "complicated dynamics" to "trivial one", that is from (c) to (a) in

[2]In general, such transitions are accompanied by very interesting dynamical phenomena. Beyond total or partial period doubling cascades of sinks, leading or not to a SA, the closed invariant curves can "fold" and, after reaching a cubic tangency with the stable foliation, they can become SA, see [17]. Thus, the lines BD are now only conditional lines (of transition from a simple attractor to a SA). Their structure seems to be rather complex. For some preliminary information see [16, 5]. See Figs. 29, 30, 37, 38 for illustrations using (5).

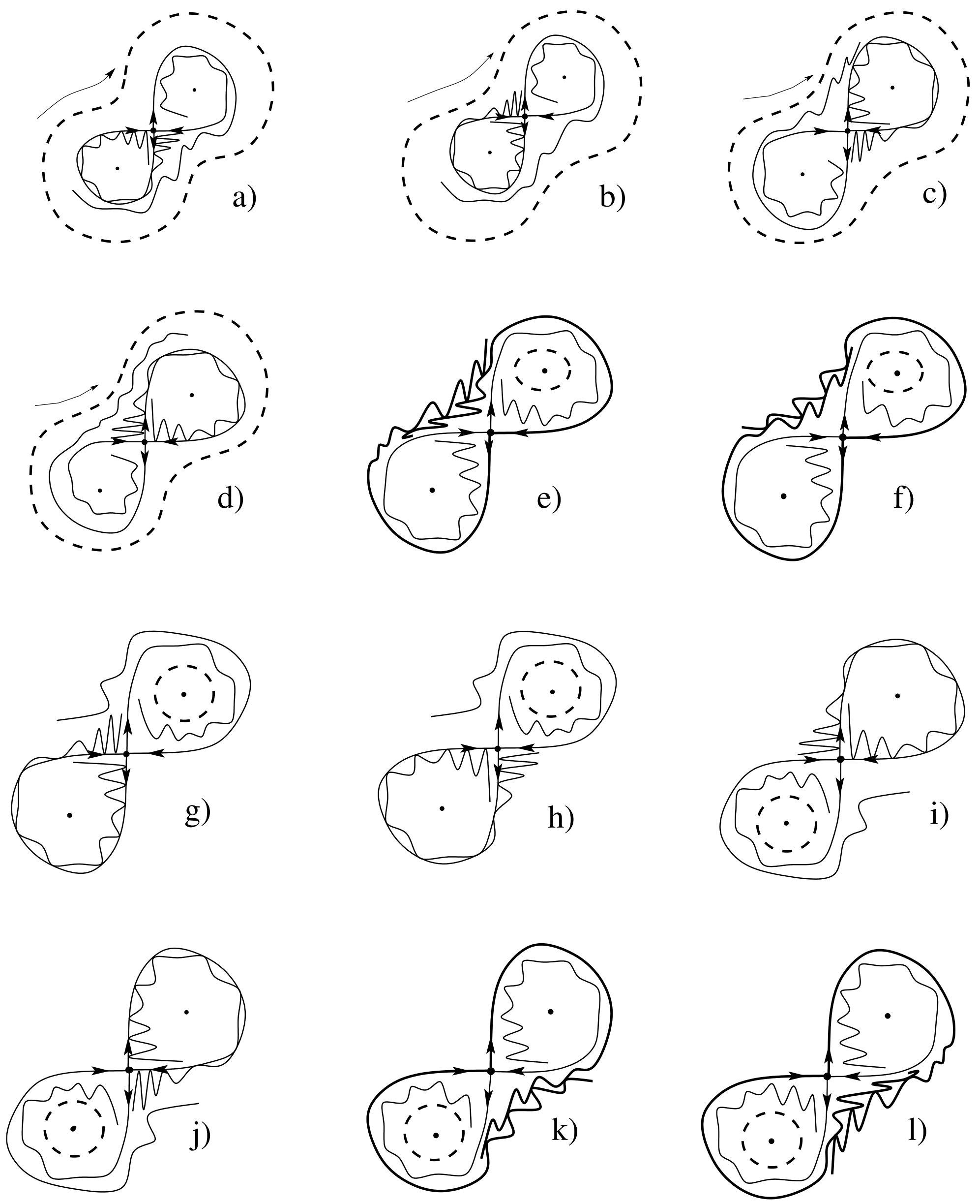

Figure 9: Homoclinic tangencies associated with the bifurcation curves in counterclockwise passage around the origin in the bifurcation diagram in Fig. 5: a) $\mu \in L_2^-$, $\mu_1 < 0$; b) $\mu \in L_1^-$, $\mu_1 < 0$; c) $\mu \in L_1^+$, $\mu_2 < 0$; d) $\mu \in L_2^+$, $\mu_2 < 0$; e) $\mu \in L_2^{\mp}$; f) $\mu \in L_1^{\mp}$; g) $\mu \in L_1^-$, $\mu_1 > 0$; h) $\mu \in L_2^-$, $\mu_1 > 0$; i) $\mu \in L_2^+$, $\mu_2 > 0$; j) $\mu \in L_1^+$, $\mu_2 > 0$; k) $\mu \in L_1^{\pm}$; l) $\mu \in L_2^{\pm}$.

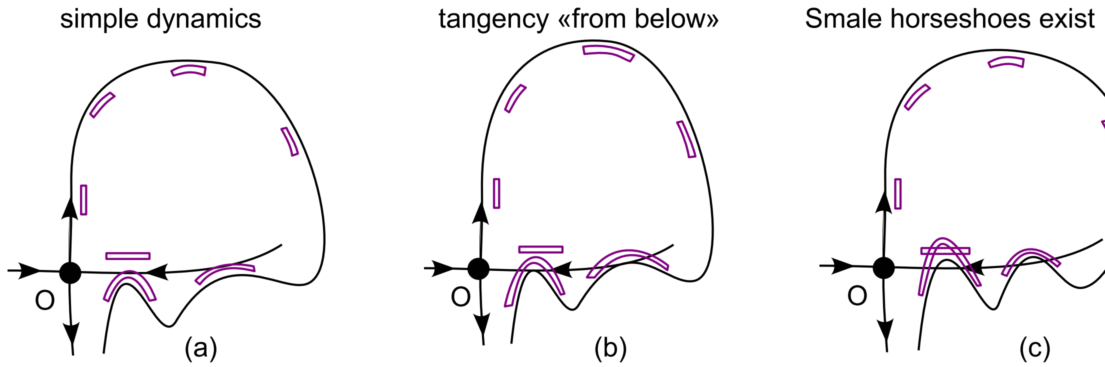

Figure 10: Creation of horseshoes (complicated dynamics) at MS homoclinic intersection.

Fig. 10). Note that in our problem if, for example, Fig. 10 illustrates the behavior on the upper loop, the expected attractor depends on what happens in the lower loop, as can be checked in Fig. 5 when crossing the line L_1^+ at different places from top to bottom. Also, between the (b) and (c) cases in Fig. 10, different periodic orbits are created at saddle-node bifurcations. Hence, one expects the existence of tiny domains of μ-parameters for which $T_{\mu,\varepsilon}$ has sinks (and the associated cascades) inside the upper loop.

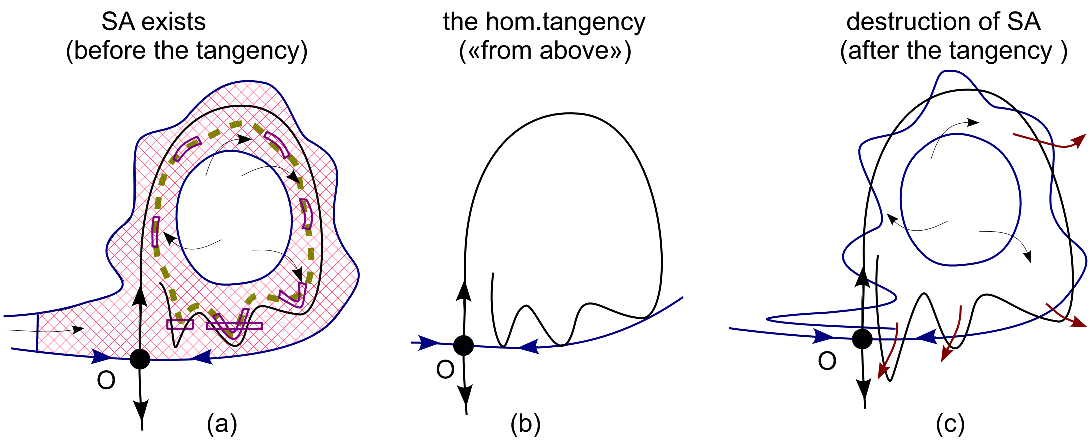

Figure 11: Towards attracting dynamics through a SA homoclinic intersection.

The SA-boundaries correspond to the homoclinic tangency which is called "last" tangency, or tangency "from above", or tangency of the third class, see Fig. 11(b) (and compare it with Fig. 9(a),(d),(f),(h),(i) and (l)). In this case all close systems can have a complicated dynamics [34]. However, the non-wandering set cannot contain global strange attractors inside the loop when transversal homoclinics to O exist because, in such a case, open sets of orbits leave the neighborhood of the homoclinic structure, see Fig. 11(c). On the other hand, the exit from the homoclinic zone can be accompanied here by the immediate appearance of some "big" strange attractor. Thus, in a situation like Fig. 11(a), an adsorbing domain with a nontrivial dynamics inside appears (for example, there exist Smale horseshoes). As before, if Fig. 11(c) displays the manifolds in the upper loop, the attractor to be expected depends on the dynamics in the lower loop. Also, in a case like (c) it can happen that some sinks (or several-pieces SA) are confined to the lobes which remain in the upper loop.

The previous "superficial" analysis of the global dynamics allows to predict the appearance and existence of big strange attractors of various types. We recall from Section 1.3 that, when they exist, we denote the attracting invariant curve inside the right (resp. left) loop of the figure-eight by C^+ (resp. C^-) and the attracting invariant curve surrounding the figure-eight by C^*. Namely, without going into details, one can roughly classify the following types of strange attractors (quasi-attractors, in fact):

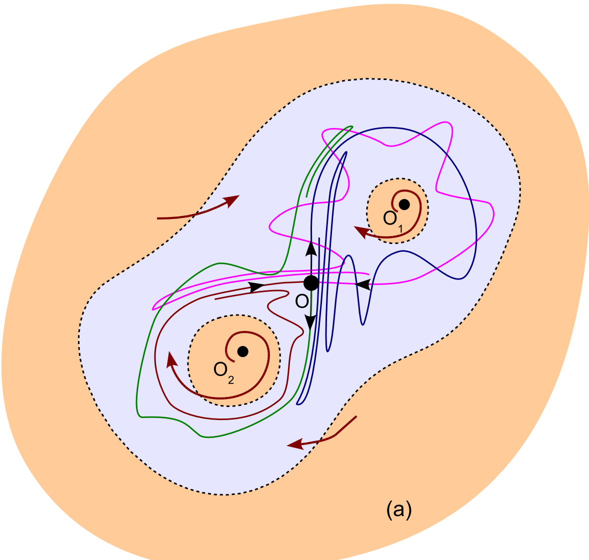

Figure 12: Homoclinic intersections in the cases (a) $\mu \in \mathbf{26}$, the "tail" strange attractor AT^+ exists; (b) $\mu \in \mathbf{19}$, the global strange attractor GA exists;

1) A^+ – it is a type of strange attractors which appear at the exit from the homoclinic zone HZ$^+$ crossing the line L_2^+ and which also appear as a result of the break-down of the invariant curve C^+. That is, these attractors exist in the regions of parameters **6**, **13**, **20**, **21**, **27**, **28**, **31** and **34**, to the right of the curve L_2^+.

2) A^- – it is a type of strange attractors which appear at the transition crossing the line L_2^- and which also appear at the break-down of the invariant curve C^-. That is, these attractors exist in the regions of parameters **8**, **9**, **10**, **11**, **12**, **13**, **14** and **15**, above the curve L_2^-.

3) A^* – it is a type of strange attractors which appear at the transition through $L_2^{\pm} \cup L_2^{\mp}$ and also at the break-down of the invariant curve C^*. Note that these attractors exist in the dashed regions **2**, **9**, **17**, **24**, **25**, **31** and **32**.

4) "Tail" strange attractors AT^- and AT^+. Their domain of existence are two triangular zones **18** and **26**. A characteristic property of such attractors is that both branches of the unstable manifold W^{u+} and W^{u-} intersect only one of the branches of the stable manifold, namely, W^{s+} for AT^+ and W^{s-} for AT^- (and do not intersect the other branch of the stable manifold). Consequently, we have a typical "tail structure" of these attractors. For example, an orbit of the attractor AT^+ can make an arbitrary number of turns near the loop Γ^+ before it makes a passage along the global piece of W^{u-}, see Fig. 12 (a).

5) Global (homoclinic) attractors GA on the figure-eight. Such attractors exist for values of the parameters inside the rectangle `abcd` (the region **19**) and are characterized by the following property: all the branches of the unstable manifold $W^{u+}(O)$ and $W^{u-}(O)$ intersect all the branches of the stable manifold $W^{s+}(O)$ and $W^{s-}(O)$, see Fig. 12 (b).

Remark. One can emphasize the difference in a symbolic description of orbits from attractors A^+, A^-, AT^+, AT^- and GA. Let Ω_2 be the set of all bi-infinite sequences $(\dots, \alpha_0, \dots, \alpha_n, \dots)$, where α_i can take the values 1 and 2. Consider some orbit from an attractor (except for the orbit O for GA). Then, by the geometry of the problem, every such an orbit can be trivially coded by one of the sequences from Ω_2: the symbol "1" (resp. "2) corresponds to every single whole passage of the orbit around the point O_1 (resp. O_2). It is clear that GA contains O and orbits with arbitrary codes; the attractor A^+ (resp. A^-) contains neither O nor those orbits whose codes have at least one symbol "2" (resp. "1"). The tail attractor AT^+ (resp. AT^-) contains O (on the boundary) and those orbits with a coding sequence without two neighboring symbols "2" (resp. "1"). In this case, the symbol "2" (resp. "1") corresponds to a tail of the attractor and some orbits can have infinitely many such tails.

3.1 Recovering the homoclinic zones and primary double homoclinic tangencies.

The bifurcation curves B^-, B^+, $B^{\pm}$ and $B^{\mp}$ for the flow (2) intersect (all of them) at the point $\mu = 0$. This implies that, typically, the pointed out homoclinic zones $HZ^+, HZ^-, HZ^{\pm}$ and $HZ^{\mp}$ are recovered and this can look, for example, as in Fig. 5. In this case, the boundary curves of the homoclinic zones intersect and the intersection points correspond in the phase space of $T_{\mu,\varepsilon}$, in general, to double quadratic homoclinic tangencies. We can compute 8 (types of) double homoclinic points labeled as `a`, `b`, ..., `h`.

Six of these points, concretely the points `b`,`d`,`e`,`f`,`g` and `h`, do not lie inside homoclinic zones and they correspond to *primary double homoclinic tangencies*, that is, there are no any other homoclinic points to the saddle O (e.g. transversal ones) except for points of the indicated homoclinic tangencies. We illustrate in Fig. 13 these primary double homoclinic tangencies (of "figure-eight" type).

The two remaining points `a` and `c` correspond to *not primary double homoclinic tangencies*, since they are located inside the homoclinic zones $HZ^{\pm}$ and $HZ^{\mp}$, respectively. This implies the existence of other (e.g. transverse) homoclinic points belonging either to $W^{u+} \cap W^{s-}$ or to $W^{u-} \cap W^{s+}$, see Fig. 14.

Note also that the points `a`,`b`,`c` and `d` belong to the boundary of the chaotic zone **19**. We remark that the points `a` and `c` also correspond to primary (single) tangencies, when W^{u+} touches W^{s+} and W^{u-} touches W^{s-} respectively, and the point O has only those two homoclinic orbits, see Fig. 14. Obviously, infinitely many homoclinic orbits of all types appear immediately after splitting the two of these primary tangencies (at the transition from regions **18, 15** and **20, 26** to region **19**).

4 The boundary structure of the homoclinic zones $HZ^{\pm}$ and $HZ^{\mp}$.

As reflected in the bifurcation diagram in Fig.5, the boundaries $L^{\pm}_{1,2}$ and $L^{\mp}_{1,2}$ of $HZ^{\pm}$ and $HZ^{\mp}$ look to be more complicated in comparison with the boundaries of HZ^+ and HZ^-. The numerical computations performed in Section 2 for the model (5) show that $L^{\pm}_{1,2}$ and $L^{\mp}_{1,2}$ have the form of kinked curves with many steps. In this section we establish (see Figs. 18 and 28 below) that these curves are C^0 and have infinitely many steps (intervals of smoothness) which accumulate to the double tangency points `b` and `d` (see Fig. 13 first row) of the rectangle **19**. More concretely, in this section we consider the following questions:

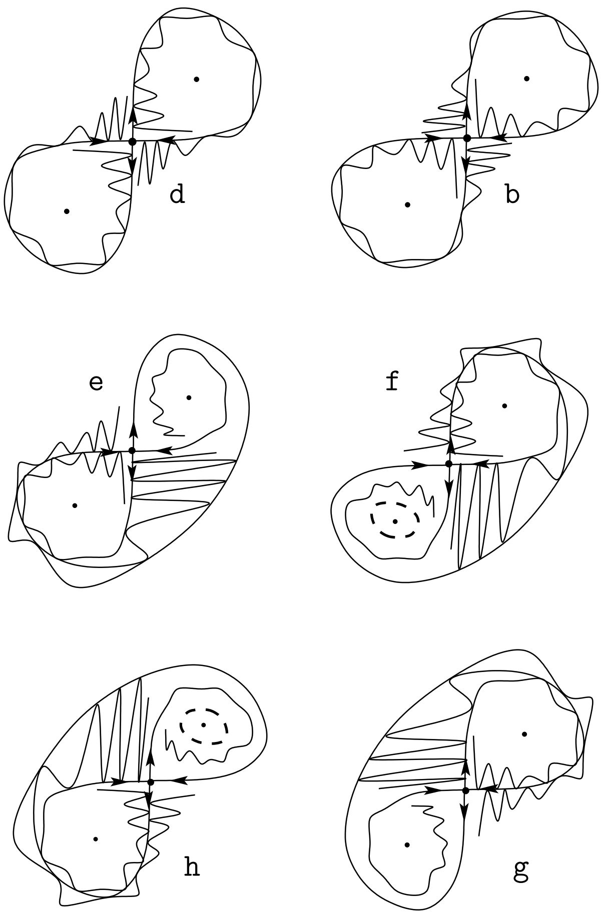

Figure 13: Primary double homoclinic tangencies corresponding to the points d,b,e,f,h,g of Fig. 5.

- why the boundaries of $HZ^{\pm}$ and $HZ^{\mp}$ are non-smooth?
- which bifurcations occur when crossing these boundaries?
- which dynamical meaning have the non-smoothness points?
- why the boundaries of $HZ^{\pm}$ and $HZ^{\mp}$ have infinitely many steps?

It turns out that such unexpected (but universal for systems having a figure-eight) structure of the boundaries of the homoclinic zones is explained by the existence (and abundance) of specific cubic and (primary) double quadratic homoclinic tangencies of the corresponding invariant manifolds of the point O: the manifolds W^{u+} and W^{s-} in the case of $HZ^{\pm}$ and the manifolds W^{u-} and W^{s+} in the case of $HZ^{\mp}$. Note that there are no main differences in the study of the boundaries for $HZ^{\pm}$ and $HZ^{\mp}$. Therefore, below we focus our attention in the zone $HZ^{\pm}$.

4.1 Non-smoothness of the boundaries.

In Fig. 9 (k) and (l), we represent the position of the manifolds W^{u+} and W^{s-} when they have quadratic homoclinic tangencies either at $\mu \in L_1^{\pm}$ (MS tangency – Fig. 9 (k)), or at $\mu \in L_2^{\pm}$ (SA tangency – Fig. 9 (l)). Analogous pictures of the manifolds W^{u-} and W^{s+} are shown in Fig. 9(e) for $\mu \in L_2^{\mp}$ and in Fig. 9(f) for $\mu \in L_1^{\mp}$. One can see that the manifolds near some of the points

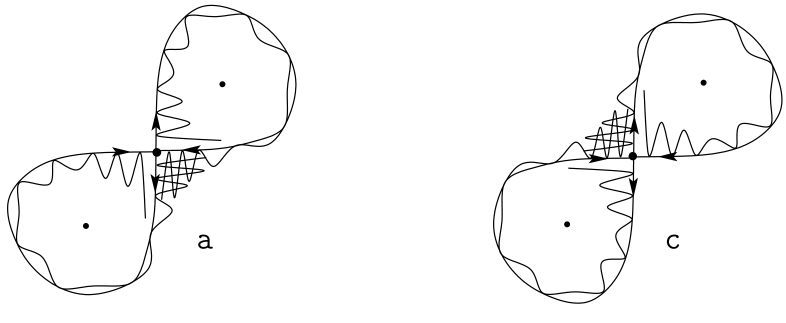

Figure 14: Not primary double homoclinic tangencies at the boundary of the chaotic zone **19** of Fig.5.

of tangency have a “sinusoidal” form.[3]

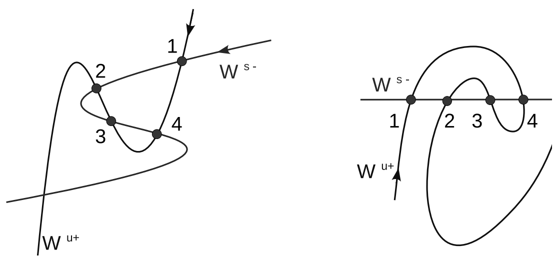

Figure 15: Sketch of the form W^{u+} and W^{s-} at $\mu \in HZ^{\pm}$. Four homoclinic trajectories (points $1, 2, 3, 4$) are created. We sketch the location of the homoclinic points $1, 2, 3, 4$ by displaying details on the manifolds near the bisectrix $y = -x,\ x > 0$ (left) and in a neighborhood of W^{s-}_{loc} close to O (right).

This “sinusoidal” form is typical for those homoclinic points appearing near the bisectrix $y = -x,\ x > 0$ of the fourth quadrant of the phase plane. Hence Fig. 15 left sketches the general position of the manifolds between the double tangencies of Fig. 9(k) and (l), compare also with Fig. 24 below. Note that Fig. 15 sketches a situation in which there are four different homoclinic trajectories in a fundamental domain (which contains the “horizontal” and “vertical” sinusoids) capturing the full dynamics near the separatrices W^{u+} and W^{s-}. However, there are other configurations expected at different μ values. Generically, depending on μ, there are up to eight different homoclinic points in a fundamental domain (see the homoclinic tangle in Fig. 14(a) and also Fig. 24 left where one counts six homoclinics in a fundamental domain but two more will appear when splitting the cubic tangency c_1). At different iterates of the same homoclinic trajectories the form of the manifolds W^{u-} and W^{s+} near them may look sharply different. For example, in the simple situation of Fig.15 left, for homoclinic points on W^{s+}_{loc} (with negative x-coordinate) the corresponding piece of W^{u+} will have a form of “distorted parabola” and, in this case, W^{u+} “makes a signature” around W^{s+}_{loc}, see Fig. 15 right.

In Fig. 16(a) we show the corresponding fragments (which extend more than two fundamental domains and represent the pattern shown at the fourth quadrant in Fig. 14(a)) of the manifolds W^{u+} and W^{s-} for $\mu \in L_1^{\pm}$. The analogous situation for $\mu \in L_2^{\pm}$ is shown in Fig. 16(b).

In a situation like the one shown in Fig. 16(a) top, we can vary μ along the curve $L_1^{\pm}$ in such a way that the tangency of type “a” does not split. However, this can be done only till the moment when a double homoclinic tangency appears. It means that the curve $L_1^{\pm}$ has always points S

[3]Of course, the form may be more complicated than a sinus-like function. This is not so relevant: the main effects related to double quadratic and cubic homoclinic tangencies will be always present.

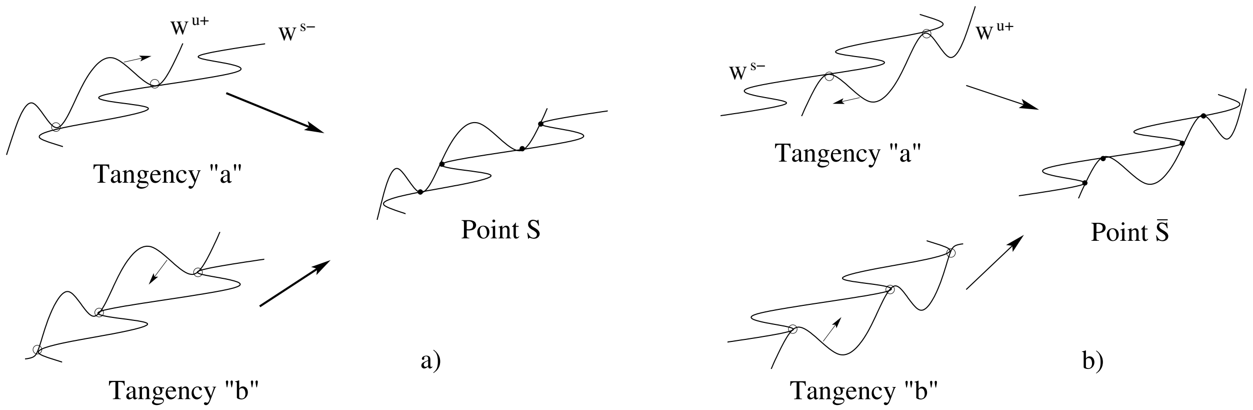

Figure 16: (a) $\mu \in L_1^{\pm}$; (b) $\mu \in L_2^{\pm}$.

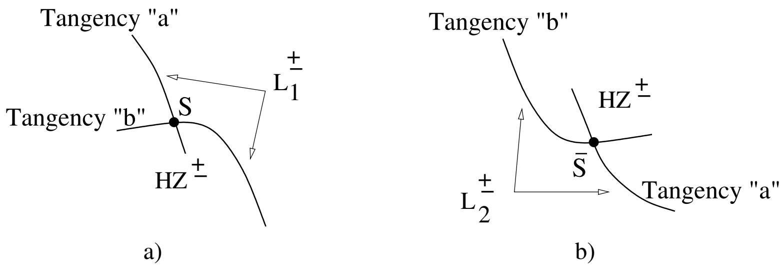

Figure 17: Bifurcation curves for tangencies "a" and "b" near the point S (left) and $\bar{S}$ (right) on the (μ_1, μ_2) parameter plane.

corresponding to the existence of two different quadratic homoclinic tangencies. After meeting the point S, we can continue the boundary curve $L_1^{\pm}$ but the homoclinic tangency "a" disappears and the new quadratic tangency "b" is kept. Thus, the point S has to be a singular point on $L_1^{\pm}$ created by the intersection of two bifurcation curves of quadratic homoclinic tangencies (of types "a" and "b", see Fig. 17(a)). In general, these curves intersect transversely. This implies that the point S is a point where $L_1^{\pm}$ loses smoothness. The same happens to the point $\bar{S}$ on $L_2^{\pm}$, see Figs. 16(b) and 17(b).

4.2 Cubic and double quadratic single-round homoclinic tangencies in $HZ^{\pm}$ and $HZ^{\mp}$.

It is interesting to trace "from beginning to end" those bifurcation curves which correspond, in Fig. 17, to the existence of tangency "a" and tangency "b". The corresponding tracing (for a typical two parameter unfolding) is demonstrated by pictures in Figs. 19, 20 and 21 and the related bifurcation curves (in the μ-plane) are shown in Fig. 18. In Figs. 19, 20, 21 and also 26, the vertical dotted lines denote some boundaries of fundamental domains. We carry out our tracing in several steps.

Step 1. Tracing a closed way $S \to c_1 \to \bar{S} \to c_4 \to S$ from Fig. 18.

Let us consider Fig. 19. Here we start at the point S, Fig. 19(a), and move the parameters μ_1 and μ_2 to keep the tangency marked by a circle and index 1 (this is tangency "b" from Fig. 16 (left)). Entering inside zone $HZ^{\pm}$ we first meet a new quadratic homoclinic tangency, point d_1, marked in Fig. 19(b) by a bold point. Moving next we can keep the first quadratic tangency

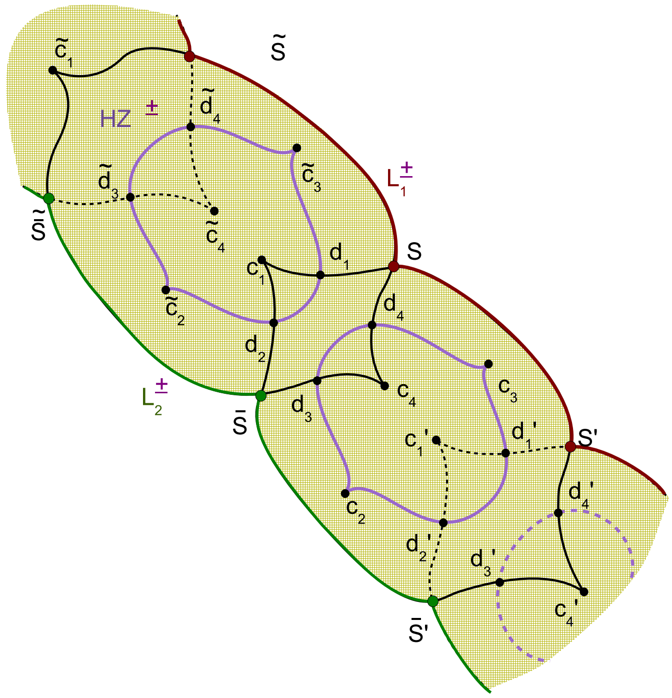

Figure 18: Structure of the bifurcation diagram in a piece of the zone $HZ^{\pm}$. We can select two series of closed curves. One of them consists of curves containing cusp points c_1 and c_4 while the curves from the other series have cusp points c_2 and c_3. We explain below (in Section 4.2) the principal details of this bifurcation diagram.

only till a cubic tangency c_1 appears as represented in Fig. 19(c). This is a final point for the bifurcation curve corresponding to the quadratic tangency 1. However, the cubic tangency gives rise to a new bifurcation curve corresponding to the existence of another quadratic homoclinic tangency labeled as 2. Following this curve we first find the point d_2, where another quadratic tangency appears, see Fig. 19(e). Next we meet the point $\bar{S}$ belonging to the curve $L_2^{\pm}$. At this moment we have two homoclinic tangencies, labeled as 2 and 3 in Fig. 19(e). Next, we move the parameters μ_1, μ_2 keeping the tangency point 3, see Fig. 19 (right). First we meet point d_3, where another quadratic tangency appears, see Fig. 19(f), and next we meet the point c_4, see Fig. 19(g), where the bifurcation curve related to the tangency 3 finishes at a cubic tangency (cusp point). Again, a new quadratic homoclinic tangency, labeled as 4, appears. Keeping the tangency 4 we meet, first, the point d_4 (where another quadratic homoclinic tangency is born) and, finally, we return to the point S closing the way.

Step 2. Tracing a way $S \to S' \to c_4' \to \bar{S}' \to \bar{S}$ from Fig. 18.

We return again to the point S in Fig. 19(a) but we move now the parameters μ_1 and μ_2 to keep the tangency 1 following the boundary curve $L_1^{\pm}$. The corresponding double and cubic tangencies taking place are sketched in Fig. 20.

Starting at S (Fig. 20 (a)) we reach first the point S' (Fig. 20 (b)), next a new double tangency d_4' (Fig. 20(c)) and we end at c_4' (Fig. 20(d)) which corresponds to a new cubic tangency. Next we can follow the other branch of quadratic homoclinic tangencies, starting at c_4'. Then, we meet, successively, the point of double tangency d_3' (Fig. 20(e)), the new point $\bar{S}'$ (Fig. 20(f)) and, following now the boundary curve $L_2^{\pm}$, we come to $\bar{S}$ (Fig. 20(g)), which is the same as in Fig. 19(e). We have traced the closed way $c_1 \to S \to S' \to c_4' \to \bar{S}' \to \bar{S} \to c_1$ from Fig. 18. Obviously, this procedure can be repeated again and we obtain new "links" containing new steps

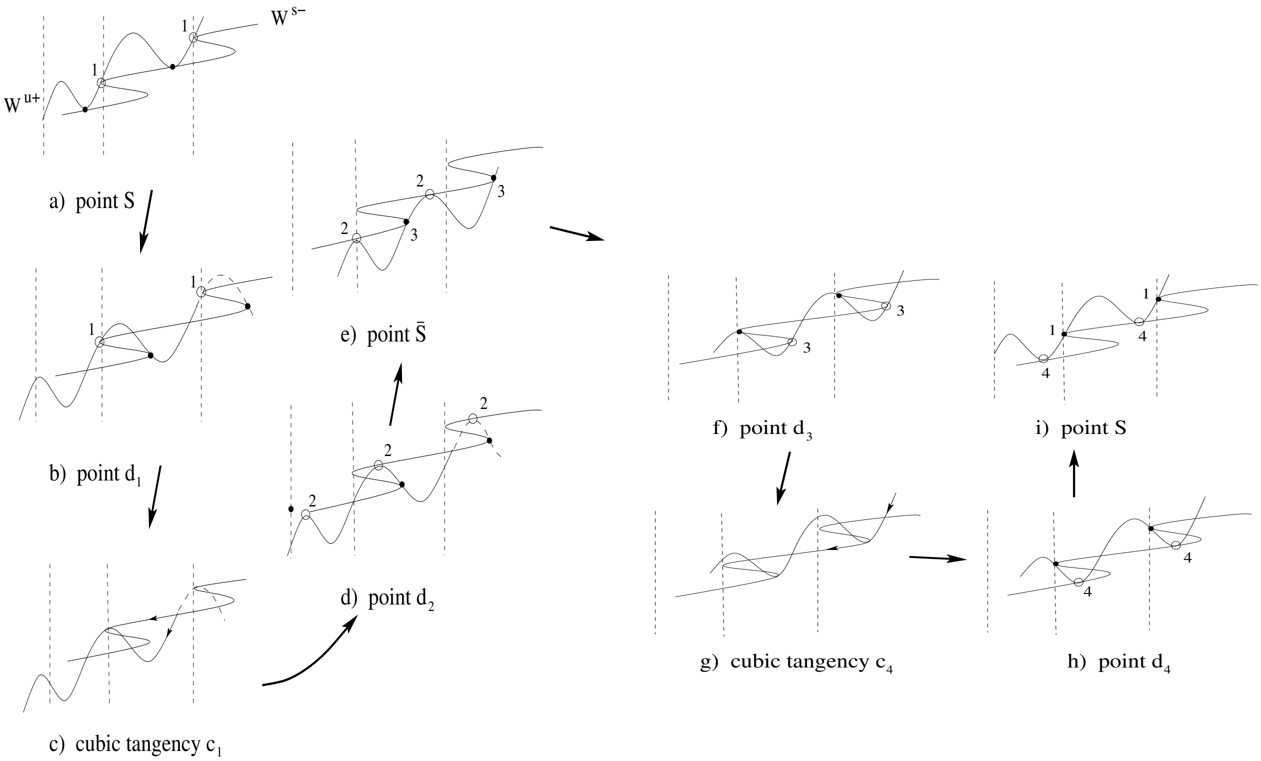

Figure 19: Sketch of double quadratic and cubic tangencies that are found following the path $S \to c_1 \to \bar{S} \to c_4 \to S$. In this figure, and in several forthcoming ones, the vertical dotted lines represent the boundaries of a fundamental domain.

in $L_1^{\pm}$ and $L_2^{\pm}$ with other end points like c_1 and c_4.

Step 3. Tracing the way $d_4 \to c_3 \to d_1' \to d_2' \to c_2 \to d_3 \to d_4$ from Fig. 18.

In Fig. 18 we observe two paths inside the zone $HZ^{\pm}$ which join S to $\bar{S}$ following the curves of quadratic homoclinic tangencies: $S \to c_1 \to \bar{S}$ and $S \to c_4 \to \bar{S}$. Each one of these paths has two points of double quadratic tangency: d_1, d_2 and d_3, d_4 respectively. We have traced the bifurcation curves corresponding to quadratic tangencies that emerge from the cusp points c_1 and c_4. However, it remains to follow the other branches related to d_1, d_2, d_3 and d_4, which belong to (generically transverse) intersections of two bifurcation curves corresponding to different single-round homoclinic tangencies.

We start now at d_4, as in Fig. 19(h). However, we will follow another curve of homoclinic tangency, the one obtained by keeping the tangency labeled by a circle in Fig. 21(a). Changing the parameters μ accordingly, we first meet the point c_3 (Fig. 21(b)) which corresponds to a new type of cubic tangency. Then, keeping another homoclinic tangency point, we reach successively the points d_1' (Fig. 21(c)), the point d_2' (compare with Fig. 19 (b) and (d)) of double homoclinic tangencies, and the point c_2 (Fig. 21(e)). The last point corresponds again to a new type of cubic tangency. Then, following another branch keeping another quadratic homoclinic tangency, we meet the point d_3 and finally, d_4, see Fig. 21 (f) and (a). Thus, the way is closed.

Note that this path is regular except at two points: c_2 and c_3. Similarly, one could consider the path $c_1 \to \bar{S} \to \bar{S}' \to c_4' \to S' \to S \to c_1$.

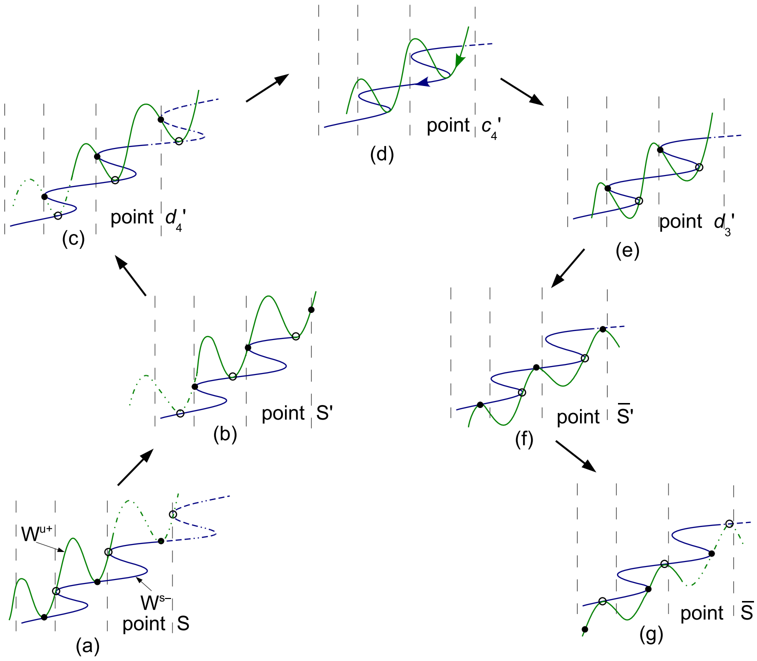

Figure 20: Sketch of double quadratic and cubic tangencies that are found following the path $S \to S' \to c_4' \to \bar{S}' \to \bar{S}$.

4.2.1 Remarks on the cubic single-round homoclinic tangencies for $\mu \in HZ^{\pm}$.

A cubic (homoclinic) tangency can be created if the manifolds W^s and W^u near a tangency point have a form of "vertical" and "horizontal" parabolas. Moving in a suitable way these parabolas we get a position such that they touch each other cubically. For example, the parabolas $y = b - x^2$ and $x = b - y^2$ have a cubic tangency at $b = 3/4$ (then the system $\{y = b - x^2,\ x = b - y^2\}$ of equations has a triple root), see Fig. 22. It is clear that this construction can be also realized for "vertical" and "horizontal" sinusoidal lines. In that case we can have many more intersections.

The main bifurcations of cubic homoclinic tangencies were studied in [39, 40, 41, 27, 28, 17]. For completeness, in Appendix A we give a short review of some of the related results.

We have shown that, moving along a bifurcation curve corresponding to a simple quadratic homoclinic tangency, we meet either some point of double homoclinic tangency (points d_i, d_i', $\tilde{d}_i$ in the figures through the text) or a point of cubic tangency (points c_i, c_i', $\tilde{c}_i$ in the figures). As stated before, for perturbations like $\varepsilon \sin t$, there exist generically four cubic tangencies which give rise to the cusp points c_1, c_2, c_3 and c_4 in the parameter plane, see Fig. 18.

There are essentially two types of cubic tangencies which depend on the sign of a coefficient d in a suitable return map. The details are given in Appendix A. Let (x, y) be straighten up coordinates around the saddle, that is, coordinates such that W^u_{loc} is given by $x = 0$ and W^s is given by $y = 0$. Assume that the cubic tangency takes place at the point $(x^+, 0) \in W^s \cap W^u$ and at the pre-image $(0, y^-)$. The coefficient d appears in the so-called global map, which maps a point (x, y) in a domain D^- around the point $(0, y^-)$ to a point $(\bar{x}, \bar{y})$ in a domain D^+ of the point $(x^+, 0)$. The first order truncation of this global map can be written as (compare with (7) in Appendix A)

$$\begin{aligned} \bar{x} - x^+ &= ax + b(y - y^-), \\ \bar{y} &= cx + d(y - y^-)^3. \end{aligned} \tag{6}$$

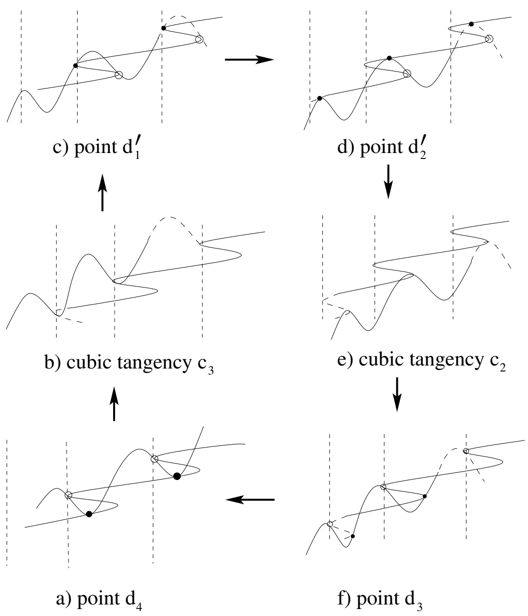

Figure 21: Sketch of double quadratic and cubic tangencies that are found following the path $d_4 \to c_3 \to d'_1 \to d'_2 \to c_2 \to d_3 \to d_4$.

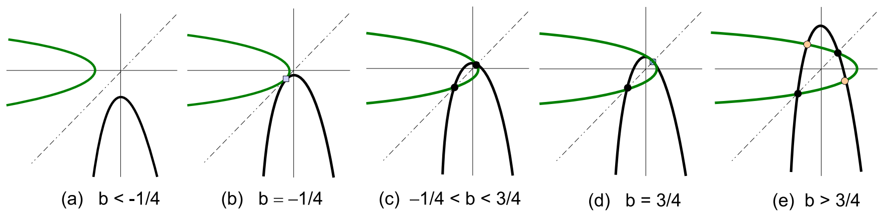

Figure 22: The creation of cubic tangency between parabolas $y = b - x^2$ and $x = b - y^2$.

The unstable manifold in D^- is given by $x = 0$. The relative position of its image in D^+ with respect to the stable one $y = 0$ determines four different cases according to the signs of b and d. We sketch these four basic cases in Fig. 23.

For d positive the unfolding of a single-round periodic orbit close to the cubic tangency shows, in the limit case, a *saddle-area* type region of stability in the phase space (see Fig. 40 left in Appendix A). For d negative the region of stability is of *spring-area* type (see Fig. 40 right in Appendix A). The names saddle-area and spring-area are suggested by the pattern of the bifurcation locus in the parameter plane. We will refer to cubic tangency (or to cusp point) of "+" or "−" type according to the sign of d.

Lemma 4.1. *The primary homoclinic cubic tangency points (or the primary cusp points)* c_1, c_2, c_3 *and* c_4 *are, all of them, of "−" type (i.e. spring-area). Concretely,* c_1 *and* c_4 *are similar to the cubic tangency (d) of Fig. 23 (i.e.* $b < 0$*), while the cubic tangencies* c_2 *and* c_3 *are similar to the cubic tangency (c) shown in Fig. 23 (i.e.* $b > 0$*).*

Proof. It is enough to sketch the position of the invariant manifolds corresponding to each of the cusp points and check the orientation. We sketch the situation for the cusp points $c_1, \dots, c_4 \in HZ^{\pm}$ in Fig. 24. Analogously one can check the situation for the cusps in $HZ^{\mp}$. □

Recall that in a 2-parameter family (unfolding) of a cubic tangency there are, in general, two branches beginning in the cusp point which correspond to the existence of different quadratic (homoclinic) tangencies.

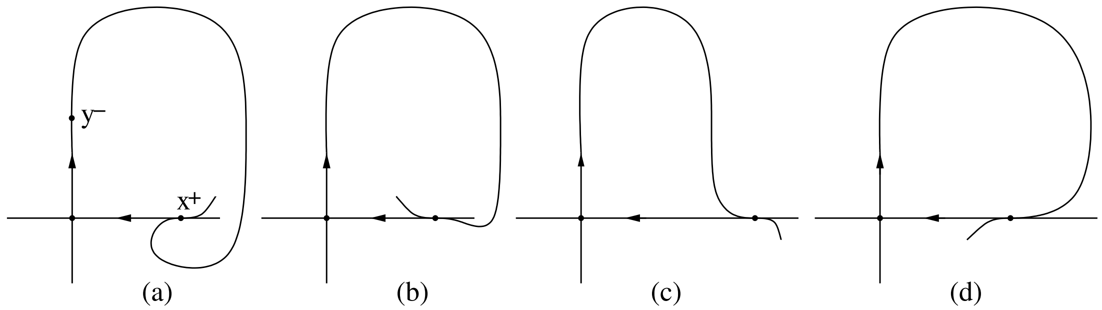

Figure 23: Primary cubic homoclinic tangencies: (a) and (b) are cubic tangencies of type "+" while (c) and (d) correspond to cubic tangencies of type "−", see text for definition. In the cases (a) and (c) the parameter b of the global map is positive, while in the cases (b) and (d) it is negative.

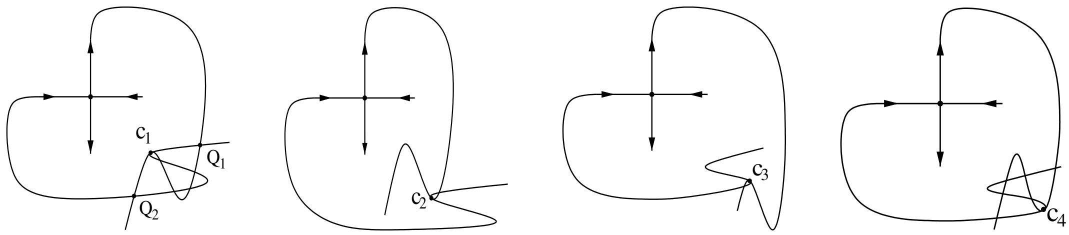

Figure 24: Sketch of the relative position of the invariant manifolds at the primary homoclinic cubic tangencies c_1, c_2, c_3 and c_4 for the zone $HZ^{\pm}$. On the left plot the point Q_1 is mapped to Q_2, hence the arcs of the manifolds from Q_1 to Q_2 are in a fundamental domain.

The appearance of cubic homoclinic tangencies (and also of tangencies of arbitrary orders) at bifurcations of quadratic homoclinic tangencies was established in [42, 43]. However, the corresponding homoclinic orbits are, in general, multi-round. For example, the new cubic homoclinic tangencies near a given quadratic homoclinic tangency in [42, 43] were only three-round. This is not the case for our situation: the cubic homoclinic tangencies which we have found are single-round. This means that their related stability domains in the phase space are expected to be larger (see Fig. 31 where these domains are shown for model (5)). We shall see that these single-round cubic tangencies play a relevant role in the dynamics within $HZ^{\pm}$ and $HZ^{\mp}$ and in some nearby domains (like, for example, in region **24**).

4.3 The complicate structure of the bifurcation diagram inside $HZ^{\pm}$.

Our next goal is to analyze the structure of the zones $HZ^{\pm}$ and $HZ^{\mp}$ as μ approaches to the vertices `a,b,c,d` of the GA rectangle in Fig. 5. In what follows, we focus on $HZ^{\pm}$. By symmetry, similar considerations also hold for the homoclinic zone $HZ^{\mp}$.

Lemma 4.2. *The point* `b` *is the final point of the boundary curves* $L_1^{\pm}$ *and* $L_1^{\mp}$ *and the point* `d` *is the final point of the boundary curves* $L_2^{\pm}$ *and* $L_2^{\mp}$*.*

Proof. In Fig. 25 we show the relative position of the manifolds W^{u+} and W^{s-} for values of μ on the bifurcation curves $L_1^{\pm}$ (left) and $L_2^{\pm}$ (right). We observe that in the left plot there is also an intersection between the manifolds W^{u+} and W^{s+}. This means, that we can continue the curve $L_1^{\pm}$ (moving down) until we find the double primary quadratic tangency when the manifolds W^{u+} and W^{s+} have the "last" homoclinic tangency and the manifolds W^{u-} and W^{s-} have the "first" homoclinic tangency. This corresponds to the existence of the double primary homoclinic tangency `b` from Fig 13. The same consideration follows for $L_2^{\pm}$ which terminates at the moment of creation of the double homoclinic tangency `d` from Fig 13. The symmetry implies that $L_1^{\mp}$ (resp. $L_2^{\mp}$) also finishes at the point `b` (resp. point `d`). □

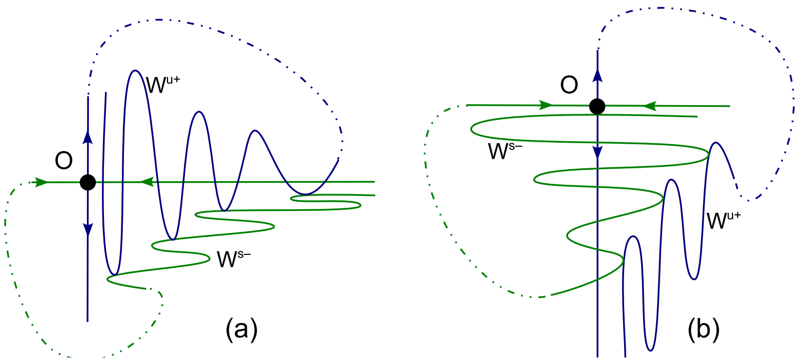

Figure 25: Behaviour of W^{u+} and W^{s-} near the double primary homoclinic tangency point `b` for $\mu \in L_1^{\pm}$ (left) and near the point `d` for $\mu \in L_2^{\pm}$ (right).

Let us consider again Fig. 18. As observed before, a point x (where x refers to any point S, d_i, c_i, $i = 1, 2, ...$) is in correspondence with a point x'. The points x and x' correspond to (either double or cubic) tangencies related to homoclinic orbits of the same type but for different values of μ. The structure of the bifurcation diagram is repeated as we move "down", towards the rectangle `abcd`, within the zone $HZ^{\pm}$.

However, the following has to be taken into account: in the transition "from *picture* to *picture* ′ " new double tangency and cubic tangency points can appear. Indeed, as we move down along $HZ^{\pm}$ and we get close to the rectangle `abcd`, the "steepness" of the sinusoidal curves W^{u+} and W^{s-} grows, meaning that more double and cubic tangency points (cusps) must appear in the bifurcation diagram. See Fig. 28 for an sketch of the structure of $HZ^{\pm}$ and $HZ^{\mp}$ close to the rectangle `abcd`.

Let us analyze why this growth of the steepness takes place as we approach the rectangle `abcd`. In Fig. 26 we sketch the growth of the "steepness" which leads to a complication of the bifurcation structure inside $HZ^{\pm}$ (or $HZ^{\mp}$) as moving "down" for $HZ^{\pm}$ (or moving "up" for zone $HZ^{\mp}$) and approaching the rectangle `abcd`. The Figs. 26 (a), (b) and (c) correspond to values of $\mu \in L_1^{\pm}$ which are (a) far away from `abcd`; (b) not far from `abcd` (and μ corresponds to some point S) and (c) near `abcd` (μ corresponds again to some S').

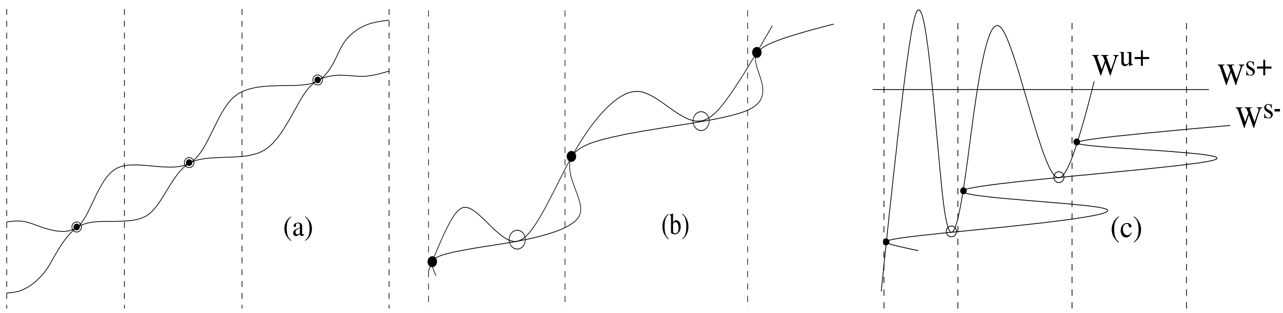

Figure 26: Growth of the steepness of the stair structure.

If we consider a case like the one shown in Fig. 26(a) there are no bifurcation curves related to primary quadratic tangencies inside $HZ^{\pm}$. In particular, we cannot meet cubic tangencies between the curves $L_1^{\pm}$ and $L_2^{\pm}$ for such values of μ. This is the expected situation far away from the rectangle `abcd`, as shown in Fig. 8 for the model (5).

On the other hand, assume that the manifolds have a middle size of steepness as in Fig. 26(b). In such a situation, keeping the quadratic tangency point marked by a circle in the figure, we find the cubic tangencies c_1 and c_4 inside $HZ^{\pm}$, see Fig. 18. Moving along the bifurcation curve from S to c_4 shown in Fig. 18 we find only few double quadratic tangency points like the point d_4 (also other mechanisms may create new types of quadratic double tangency, see Corollary 4.0.2 below). This is also the situation shown in Fig. 8 for the model (5) where, for the pieces of the bifurcation diagram shown, only one double quadratic tangency point is observed when moving from S to c_4.

Finally, consider a case like Fig. 26(c). In such a situation, following the bifurcation curve from S to c_4, we expect to meet many double quadratic tangency points. This is due to the accumulation process towards the rectangle `abcd`.

There are infinitely many such reconstructions when moving down towards the rectangle `abcd`. To clarify the full picture the following lemma states the way in which the cubic tangencies accumulate.

Lemma 4.3. *For parameters μ inside $HZ^{\pm}$ the following considerations hold.*

1. *The primary cubic tangencies of type c_1 can exist only if $W^{u+} \cap W^{s+} = \emptyset$ and $W^{u-} \cap W^{s-} = \emptyset$. This means that c_1 can only exist in the regions* **3** *and* **10** *of the bifurcation diagram Fig. 5.*

2. *The primary cubic tangencies of type c_2 can exist if $W^{s+} \cap W^{u+} = \emptyset$. Thus, they can exist within the regions* **3**, **10** *and* **18** *of Fig. 5.*

3. *The primary cubic tangencies of type c_3 can exist if $W^{s-} \cap W^{u-} = \emptyset$. Thus, they can exist within the regions* **3**, **10** *and* **15** *of Fig. 5.*

4. *In the region* **19** *of Fig. 5 only primary cubic tangencies of type c_4 can exist.*

Proof. We follow the notation of Fig. 27, see also Fig. 23 and Fig. 24 for the different types of cubic tangencies. Since we consider $\mu \in HZ^{\pm}$ the cubic tangencies can only exist in the region of the phase space which is below the local manifold W^{s+} and to the right of the local manifold W^{u-}. Then, if $W^{u+} \cap W^{s+} \neq \emptyset$, the point m_1 is located above W^{s+}_{loc}. This implies that the cubic tangencies c_1 and c_2, which involve the point m_1, cannot exist. Similarly, if $W^{u-} \cap W^{s-} \neq \emptyset$ then the point m_3 is located to the left of W^{u-}_{loc} and the cubic tangencies c_1 and c_3 cannot exist. Finally we note that for parameters $\mu \in HZ^{\pm}$, a set which includes the rectangle `abcd` (region **19**), the points m_3 and m_4 are always in the region where we can have a cubic tangency of type c_4. □

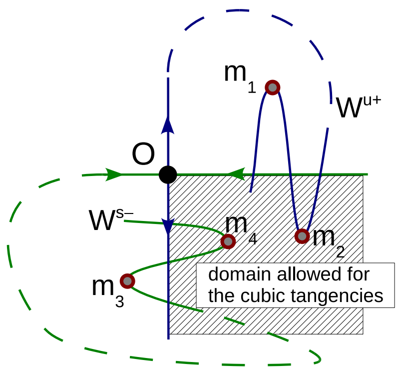

Figure 27: Domain where we can have primary cubic tangencies c_1, c_2, c_3 and c_4.

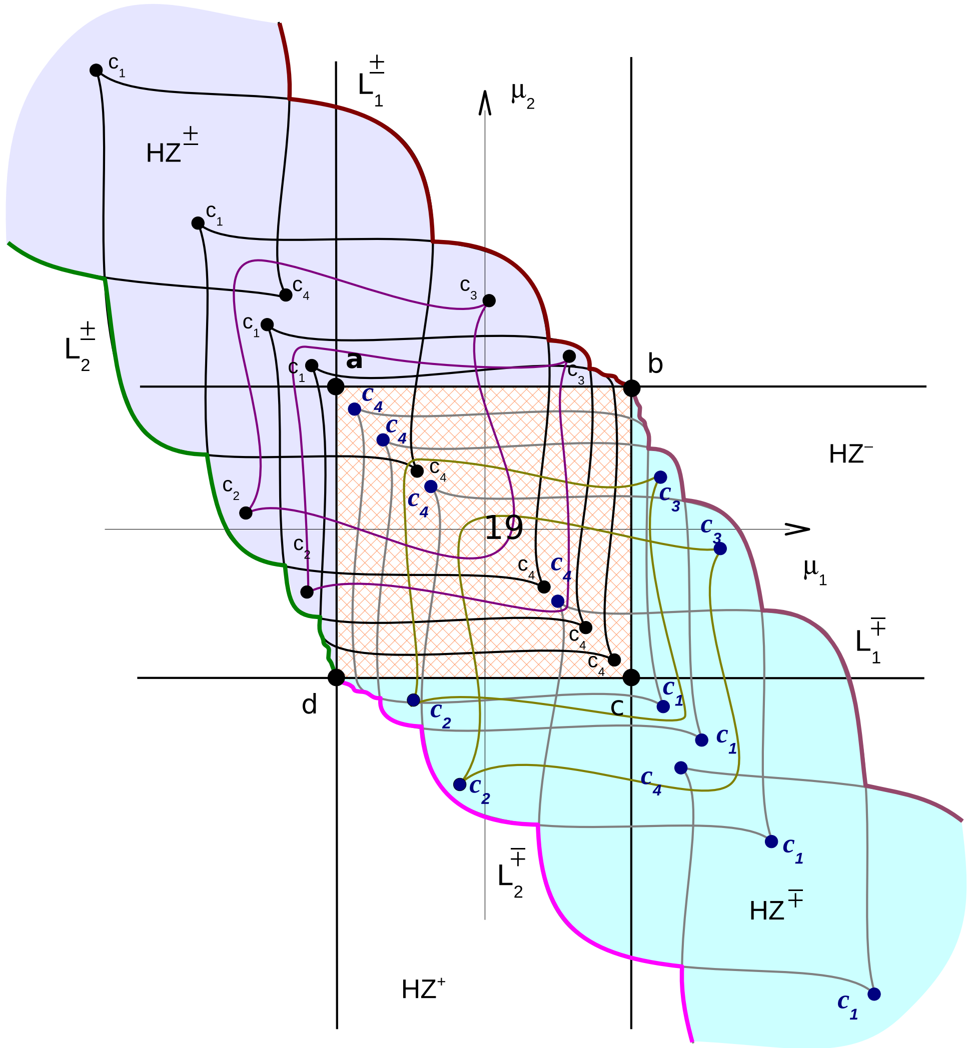

Figure 28: Structure inside the homoclinic zone $HZ^{\pm} \cup HZ^{\mp}$ (continuation of Fig. 18 for parameters close to the rectangle `abcd`).

Corollary 4.0.1. *The cusp points c_1, c_2, c_3 and c_4 accumulate to the points* `a,d,b` *and* `c` *respectively, which are the vertices of the rectangle bounding the zone GA.*

In particular, the accumulation of the c_1 and c_4 type points to different vertices means that, at some moment, the bifurcation points c_4 and c_1' must interchange position inside $HZ^{\pm}$. That is, the μ_1 coordinate of c_4 becomes larger than the one of c_1' (see Fig. 28). See details in Fig. 7 (second row right) concerning the model (5). This creates new double primary quadratic homoclinic tangencies.

Corollary 4.0.2. *There exist infinitely many primary double quadratic tangencies corresponding to the intersection of the homoclinic branches related to the primary cubic tangency points of type c_1 and c_4.*

Similar considerations hold for $HZ^{\mp}$. As a result, we obtain the global bifurcation diagram related to the homoclinic tangencies (quadratic and cubic) inside the zone $HZ^{\pm} \cup HZ^{\mp}$, see Fig. 28.

5 A quantitative approach to the bifurcation problem

Let us proceed now to a more quantitative analysis of the parameter and phase spaces of the map $T_{\mu,\varepsilon}$. To this end, we consider again the model (5) introduced in Section 2.

For simplicity of the presentation we consider again the same parameters that were considered in Section 2, that is, $b_1 = 0.003$, $b_2 = 0.0015$, $\psi = 1.6$, $A = 2$ and $\omega_1 = \omega_2 = 0$. Other sets of parameters have been also considered in simulations, the corresponding figures displaying a similar behavior to the ones shown below.

As shown in Fig. 5, when leaving a homoclinic zone through an SA-boundary there is a region of the parameter space where one expects that $T_{\mu,\varepsilon}$ exhibits different types of chaotic attractors together with periodic sinks. To have a good picture of these regions we compute the maximal Lyapunov exponent (MLE or Λ) of an orbit starting in the unstable invariant manifold (in both domains of the FD). For each point in the (a_1, a_2)-plane we consider the initial condition (i.c.) (z_0, η_0, s_0) with $z_0 = 0.5$, $\eta_0 = 0$ and s_0 either 1 or -1. To compute Λ we have used the MEGNO approach (see [44] and also [45] for an application to conservative maps). For each initial data, after a transient of 10^5 iterates, a maximum of 10^6 iterates has been used to compute Λ, but if a periodic orbit up to a period $k \leq 10^3$ is detected, the computation is stopped, the periodic orbit is refined and Λ is obtained from DM^k, where the map M is given by (5). A threshold Λ_0 is used to decide whether Λ is positive, zero or negative: $\Lambda > \Lambda_0$, $|\Lambda| \leq \Lambda_0$, $\Lambda < -\Lambda_0$, respectively. The value used for Λ_0 is 10^{-6}. The concrete values of a_1, a_2 in the computations go, in both cases, from -0.15996 to 0.15996 with step 0.00008. This is relevant because other choices can change minor details in the left plot in Fig. 29 for $a_1 > b_1$, but close to b_1, and in the right plot for $a_2 > b_2$, but close to b_2, as we shall explain. Another detail to point out is the choice of the i.c. As we can expect multiplicity of attractors, for some values of (a_1, a_2) the result depends on the i.c. To check this effect a computation has been done using 10^6 pixels in the domain of Fig. 29 with 12 different i.c. (both for $s_0 = 1$ and $s_0 = -1$). The total fraction of cases in which not all the i.c. give the same attractor is ≈ 0.002. We also did similar computations with smaller ε (e.g., by dividing (b_1, b_2) by 2 and 3), obtaining similar results but with a minor presence of SA and sinks, as one could expect.

5.1 Results of scanning the (a_1, a_2) parameter plane

The results are shown in Fig. 29. The left plot shows the computation for $s = 1$ while the right one corresponds to $s = -1$. In the figure, the parameters (a_1, a_2) for which $\Lambda > 0$ and, hence, the used initial point tends to a SA, are shown in red. We plot in green the set of points for which $\Lambda = 0$ and, hence, the initial point tends to an invariant curve. White regions correspond to sinks, $\Lambda < 0$. As mentioned, some changes are produced if the initial point changes, because of the possible multiplicity of attractors, but they have a minor impact on the global figure. We note that, as expected, inside the green and red regions there are infinitely many white domains which correspond to sinks. Next we shall comment on such a structure in more detail.

Let us compare the Fig. 29 left with Fig. 5 (the following comments apply also to the right one in an analogous way by exchanging the roles of a_1 and a_2). At $a_1 = -0.15$, going from top to bottom, we see a transition from a green domain to a red one. It corresponds to the bifurcation line $L_2^{\pm}$, while $L_1^{\pm}$ (in top of $L_2^{\pm}$) is not observed in the figure. As discussed in Section 3 the homoclinic zone $HZ^{\pm}$ bounded by $L_1^{\pm}$ and $L_2^{\pm}$ corresponds to a situation between tangencies of types k) and l) in Fig. 9. A SA surrounding the full figure-eight is not possible because points to the left of W^{s-} are trapped by the attractor around O_2. Typically, on top of $L_2^{\pm}$ it will be

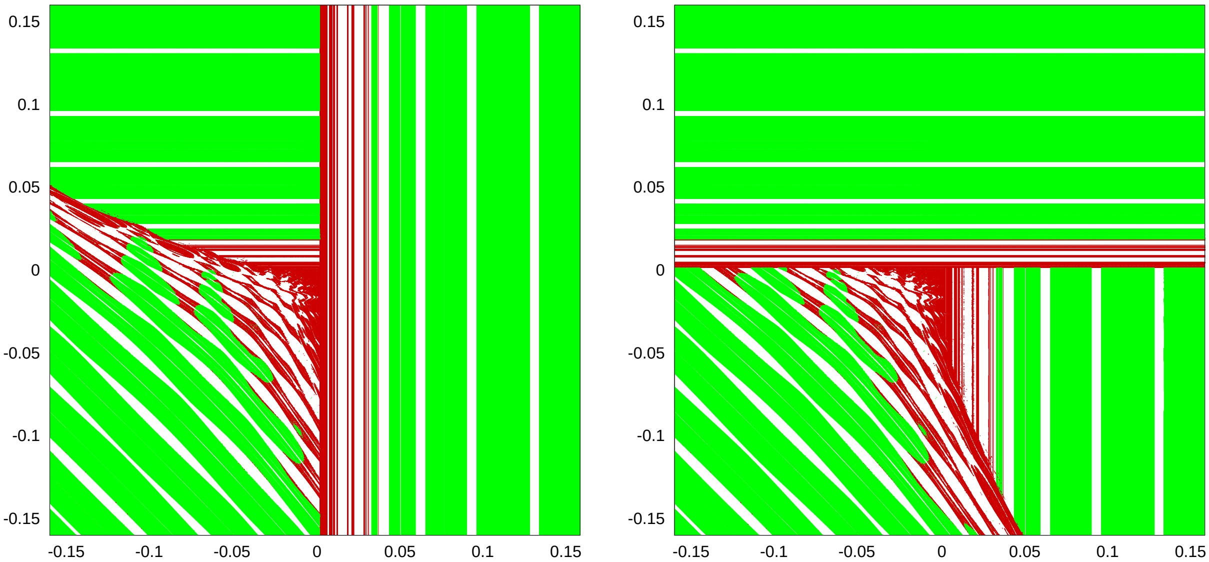

Figure 29: Maximal Lyapunov exponents (Λ) for the orbit with initial condition $(0.5, 0, s_0)$ with $s_0 = 1$ (left) and $s_0 = -1$ (right). Red points correspond to $\Lambda > 0$ (chaotic attractor), green points to $\Lambda = 0$ (invariant curve) and white points to $\Lambda < 0$ (periodic sink). Some white domains are narrow and can be seen by magnifying.

an invariant curve, $\Lambda = 0$, or a sink, $\Lambda < 0$. However, it can happen that for $(a_1, a_2) \in HZ^{\pm}$ an attractor, surrounding the figure-eight, is located "inside" W^{u+} but "outside" W^{s-}, in the homoclinic lobes. It can be either a high period sink or a "many-pieces" SA (see again Fig. 9 k) and l)). And, in fact, attractors of this type have been located when either one uses many i.c. to compute the orbits or for fixed a_1 one proceeds to scan a_2 with small stepsize (e.g. 10^{-6}). The same phenomenon has been observed in all other homoclinic zones displayed in Fig. 5 but which can not be "seen" in Fig. 29.

The rectangle `abcd` is a very small rectangle located inside the mostly red colored region close to $a_1 = a_2 = 0$. The vertical (resp. horizontal) red regions in Fig. 29 left (resp. in Fig. 29 right) are located in the zone between the bifurcation curves L_2^+ and the boundary "curve" BD^+ (resp. between L_2^- and BD^-). The possible attractors, either sinks, SA or invariant curves, for parameters (a_1, a_2) from the right part (resp. above) of L_2^+ (resp. L_2^-) are located inside the upper (resp. the lower) loop of the figure-eight when we take $s_0 = 1$ (resp. $s_0 = -1$). Hence they are independent of the value of a_2 (resp. a_1). This is the reason why we observe vertical (resp. horizontal) lines in the Fig. 29 left (resp. in the Fig. 29 right).

The bifurcation "curve" BD^+ (resp. BD^-) is essentially a horizontal (resp. vertical) "curve". A point worth to stress is that BD^+ and BD^- determine a domain where the attractive invariant curves of the map (in the green parameter region) are destroyed because they "fold" when they have a tangency with the stable foliation of O (see [17] for details). The first one of these tangencies is a cubic one. Then they become either a SA or a sink. As the curves attract the unstable manifold, one can find a rough estimate of the size of this domain by asking that already the first image of W^u in a fundamental domain is no longer a graph. Points with $z \in [0, 1), \eta = 0$ are mapped to $(z + A\log(|y|), \mathrm{sign}(y)|y|^{\psi})$, where now $y = a_j + b_j \sin(2\pi z)$ with j either equal to 1 or 2. The condition to stop being a graph is $d(z + A\log(|y|))/dz = 0$. It is easily checked that this gives the values $a_j = Cb_j$, where $C = \sqrt{1 + (2\pi A)^2}$. For smaller values of $|a_j|$ already the first image of the unstable manifold in a fundamental domain is no longer a graph.

Consequently, the domain between HZ^+ and BD^+ (resp. HZ^- and BD^-) is expected to be

$\mathcal{O}(b_1)$ (resp. $\mathcal{O}(b_2)$). For the present parameters ($A=2$, $b_1=0.003$ and $b_2 = 0.0015$) the above estimate gives $C\approx 12.6061$ and, hence, BD^+ is expected to be at $a_1\approx 0.0378$ while BD^- is roughly given by $a_2 \approx 0.0189$. Both values agree well with the Λ computations shown in Fig. 29.

Finally, we note the nice structure for BD^{+-} observed in Fig. 29, looking like a curve between red and green with large oscillations. Crossing this "curve" the attractive invariant curves surrounding the figure-eight are expected to be "folded", becoming (possibly) SA. This has been checked by scanning narrow intervals crossing the "curve" with small steps in a_1, a_2. Such a structure depends on the concrete parameters b_1 and b_2 considered and on the representation of the W^u with respect to W^s in the FD. As in the BD^+ and BD^- cases, folding starts with a cubic tangency of the invariant curve with the stable foliation of O.

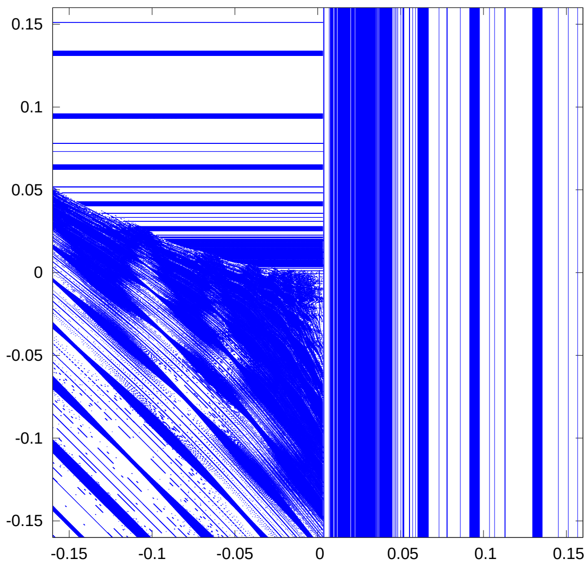

Figure 30: Set of (a_1, a_2)-parameters of computed $\Lambda < 0$, as in Fig. 29 left, for the trajectory with initial condition $(0.5, 0, 1)$. Many details can be seen by magnifying the plot, computed with 16×10^6 pixels.

As previously mentioned, the white pixels in Fig. 29 correspond to periodic sinks ($\Lambda < 0$). The global structure of this set of parameters in the (a_1, a_2)-plane is shown (blue pixels) in Fig. 30. This fills the white regions of Fig. 29 left.

5.2 Some details on the parameter domains related to sinks

The Fig. 31 magnifies the structure shown in Fig. 30 close to the rectangle `abcd`. We remark that the homoclinic zone HZ^+ is given by the condition $|a_1| \leq 0.003$ and HZ^- by $|a_2| \leq 0.0015$. Hence, comparing with Fig. 5, in Fig. 31 we show the rectangle (region **19**) and part of the regions **17** and **18** within HZ^-, part of the regions **25** and **26** in HZ^+ and part of the region **24**. The blue points correspond to periodic sinks of all (detected numerically) periods, while the red points are those which have period 2. Periods are counted on the FD. Hence, red points correspond to periodic trajectories with i.c. in the $s=1$ domain, the first iterate is in the $s=-1$ domain, then go back to the $s=1$ domain and close.

Let us try to explain the structure observed in Fig. 31. Concretely, we focus on the structure of the 2-periodic sinks (in red in the figure, while blue corresponds to higher period sinks). In Section 4 we stated that the bifurcation diagram in the homoclinic zone $HZ^\pm$ (and $HZ^\mp$) is

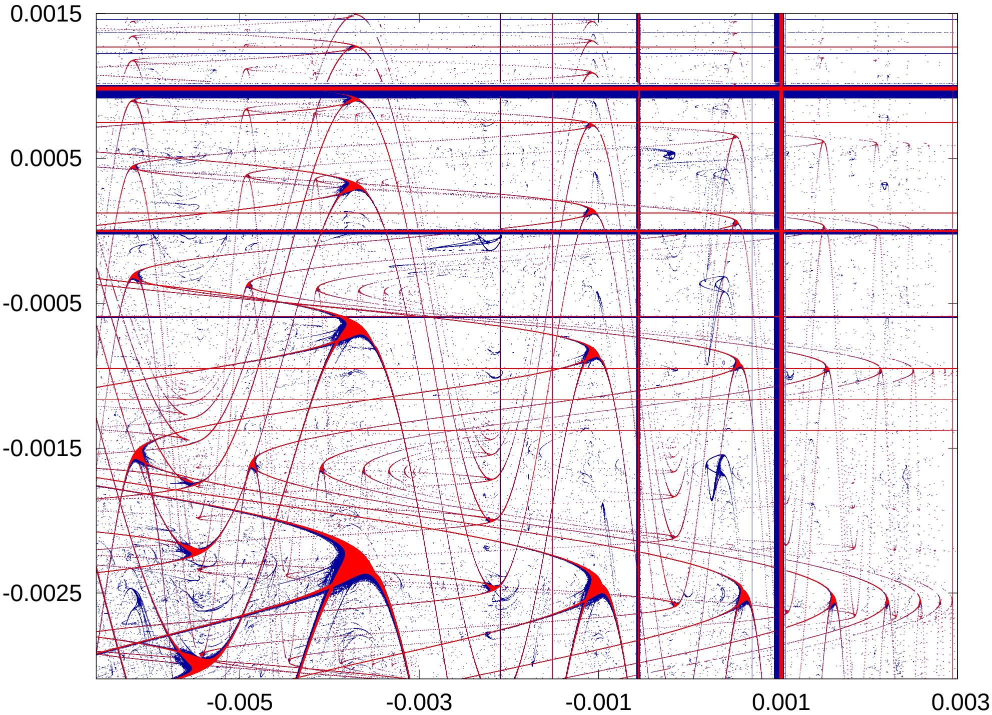

Figure 31: In blue we represent the set of (a_1, a_2)-parameters with computed $\Lambda < 0$ for the trajectory with initial condition $(0.5, 0, 1)$. For these parameters the attractor is a periodic sink. In red we show those parameters for which there is a 2-periodic sink as attractor. Periods are counted on the FD.

organized by the cubic tangencies c_i, $i = 1, \ldots, 4$ and that these cubic tangencies c_i accumulate themselves to the corresponding vertex of the limit rectangle `abcd`.

On the other hand, we recall from Section 4.2.1 that the cubic tangencies are of "$-$" type (c_i are spring-area cusp points). As it is well-known, see [17, 27, 28], one of the possible (and most frequently) configurations around a tangency of "$-$" type is such that the corresponding area of stability in the parameter plane corresponds to a cross-road area, see Appendix A. Concretely, in Fig. 32 we sketch the position of the fold bifurcation curves L_1^+ and L_2^+, and the flip bifurcations curves L_1^- and L_2^-. In particular, we observe that in a cross-road scenario the flip curves accumulate to two different fold curves at different regions of the parameter space. This is the type of the main stability areas shown in Fig. 31.

As it is known, see [39, 17] and also the Appendix A, related to each one of the cusp points c_i one expects to observe a cascade of cusp bifurcations (cubic tangencies) which accumulates to it. Accordingly, in Fig. 31 we observe four families of what looks like cross-road stability regions (large "triangular" regions basically in red) which accumulate to cubic points of the type c_i, $i = 1, \ldots, 4$ in $HZ^{\pm}$ and $HZ^{\mp}$. Each type of cross-road (with different orientation) accumulates to a different cubic tangency c_i. We recall that from a cross-road configuration emanate four strips of stability which can be easily observed in the Fig. 31. Two of them correspond to the strips between the fold and the two flip bifurcation curves (i.e. between the curves L_1^+ and L_1^-,L_2^- in Fig. 32), while the other strips are bounded by the flip curves and a fold curve (i.e. between the curves L_1^-,L_2^- and L_2^+ in Fig. 32). By "the orientation of the cross-road" we refer to the direction towards which it "points" the cusp point on L_1^+ in Fig. 32. For instance, the cross-road in that figure has the orientation $(0, -1)$.

The structure around a cross-road can be clearly observed in the Fig. 31. For example the largest cross-road area observed in Fig. 31 is located at $(a_1, a_2) \approx (-0.0038, -0.0023)$ and we

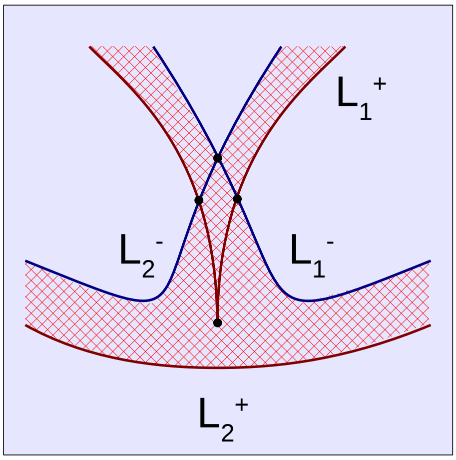

Figure 32: Parameter representation of a cross-road area. The fold bifurcation curves are labeled with "+" while the flip bifurcation curves are labeled with "−". The dashed region corresponds to the cross-road stability area.

clearly distinguish the four strips. This cross-road has approximately the orientation of the vector $(1, 1)$. It is related to two cubic points of type c_3: one in $HZ^{\pm}$ and the other in $HZ^{\mp}$ (see Fig. 28). Hence we observe that this cross-road is part of a (vertical) sequence of (roughly) cross-road configurations which accumulate close to the top part of $HZ^{\pm}$ and, at the same time, it is part of a (horizontal) sequence of (roughly) cross-road configurations which accumulate to the right part of $HZ^{\mp}$.

At this point it is worth to stress that the results shown in figures 29, 30 and 31 have been obtained starting at some fixed values of z, η, s. Due to the multiplicity of attractors and the changes on its basins when we change (a_1, a_2) it can happen, for instance, that a sink of a given period subsists for a domain slightly larger than what is shown. Indeed, this happens in Fig. 31. In Fig. 33 we have been using a different method, by "following the attractor". That is, starting the computations for given (a_1, a_2) at the last iterate computed in the attractor found for nearby values of (a_1, a_2).

Let us examine one of the sequences of (roughly) cross-road configurations mentioned. For example, let us consider the horizontal sequence related to the cross-road located at $(a_1, a_2) \approx (-0.0038, -0.0023)$ in Fig. 31. Assume that this configuration is related with the return map close to the cubic tangency c_3 in $HZ^{\mp}$ for some (large) period k (see Appendix A for the details of the derivation of the return map). The next cross-road configuration, located at $(a_1, a_2) \approx (-0.0011, -0.0023)$, is obtained as the stability region of the return map with period $k + 1$. For a cubic tangency of "−" type, like the cubic tangency c_3, we prove in Appendix A that, in the limit $k \to \infty$, the only possible configuration for the stability region related to the return map is a spring-area configuration (see Fig. 40 right). We expect, then, to observe a spring-area configuration in the limit of the sequence related to the cross-road at $(a_1, a_2) \approx (-0.0038, -0.0023)$ as a_1 approaches the cubic tangency c_3 in $HZ^{\mp}$, i.e. for values $a_1 \approx 0.003$. This is exactly what is observed in Fig. 33. [4]

As an example we focus on some domains of sinks near $a_2 = 0.00059$ in GA moving to HZ^{-} (see Fig. 5). These domains are so small that even the first one, which is the larger one, is not visible in Fig. 31. Concretely, the Fig. 33 top left shows the last configuration of the cascade with $a_1 < b_1$, that is, the last one inside the homoclinic zone HZ^{+}. We clearly see how a spring-area has separated from the fold curve, and that a flip curve appears bounding a strip (in black) at

[4] In [27, 28] a transition scenario from cross-road to spring-area configuration was described, however it seems that the one observed here might differ from that one. A complete description of the possible evolution scenarios is needed to clarify this point. We postpone this analysis for future works.

some distance from the spring-area. Let k be the period of the return map close to the cubic tangency c_3 in $HZ^{\mp}$, see Appendix A. Then $k = k_1 + k_2$ where k_1 is the number of iterates from the domain $s = 1$ to the domain $s = -1$ and k_1 from $s = -1$ to $s = 1$. Then, Fig. 33 top left corresponds to $(k_1, k_2) = (14, 22)$. We note that almost any initial condition on W^u with $s = -1$ converges to the sink attractor related to this stability region.

The next stability domain is obtained for $(k_1, k_2) = (14, 23)$ and it is shown in the Fig. 33 top right. In this case, there are few initial conditions of W^u with $s = -1$ that converge to the corresponding sink attractor. That is, the basin of attraction of the periodic sink intersects W^u in the $s = -1$ domain in a very small interval (or a collection of tiny intervals). Scanning the values of $z \in [0, 1]$ with a small step gives an estimate of the measure of this interval which is ≈ 0.002083. For this reason, to show the spring-area configuration, when for some (a_1, a_2) an initial condition converges to a sink (or maybe a SA) related to the spring-area, we have used the last iterate computed for these parameters (a_1, a_2) as initial condition for some nearby set of parameters (a kind of continuation technique). This explains why some parts of the configuration that are expected to correspond to 2-periodic sinks (in black) are observed in red or pale blue, which correspond to sinks of larger periods, or in white (for white small spots inside) which correspond to strange attractors. We invite the reader to magnify the Fig. 33 top right close to the crossing of the stability strips emanating from the spring-area configuration to observe the details. We note that this is a consequence of the phenomenon of coexistence of attractors for some of the parameters.

Keeping $k_1 = 14$ fixed, for $k_2 = 24$ and $k_2 = 25$ we obtain the next two elements of the cascade related to the cubic tangency c_3 in $HZ^{\pm}$. We see the spring-area configurations and how they separate from the strip of stability which previously was part of the cross-road configuration. Note the size of the configuration, which agrees with the scalings obtained for the size of the spring-areas for different k values in Appendix A.

Similar considerations concerning the accumulation of the stability areas apply to the other types of cross-road configurations which have a different orientation. Hence the cross-roads with orientations $(1, -1)$, $(-1, 1)$ and $(1, -1)$ accumulate to cubic tangency points of type c_4, c_1 and c_2 in $HZ^{\pm}$, respectively. The last type of oriented cross-road (i.e. $(1, -1)$) might be difficult to observe in Fig. 31. The largest one of these domains is located at $(a_1, a_2) \approx (-0.0054, -0.0028)$ slightly above a much larger cross-road with orientation $(-1, 1)$. The reader can also observe another transition from cross-road to spring-area related to the vertical sequence of the previous large cross-road with orientation $(-1, 1)$, for values of $a_2 \approx -0.0015$ the spring-area separates from the previous cross-road configuration in the same way that is observed in Fig. 33.

We remark that the previous considerations follow from a local study around the cubic tangency and around the fixed points of the return maps of period k. On the other hand, the Fig. 31 displays a fascinating global structure which needs a different approach to be analyzed. In this sense, it is interesting to note that each of these cross-road configurations is connected with the others by four large strips of stability (also in red, hence for these parameters there are 2-periodic sinks) which emanate from the main part of the stability region. This is related with the structure of the bifurcation diagram inside $HZ^{\pm}$ (and $HZ^{\mp}$) which also joins the different cubic tangency points, see Figs. 18 and 28. In Fig. 34 we sketch the global structure observed in Fig. 31 where we represent the fold and flip bifurcation lines and how they intertwine.

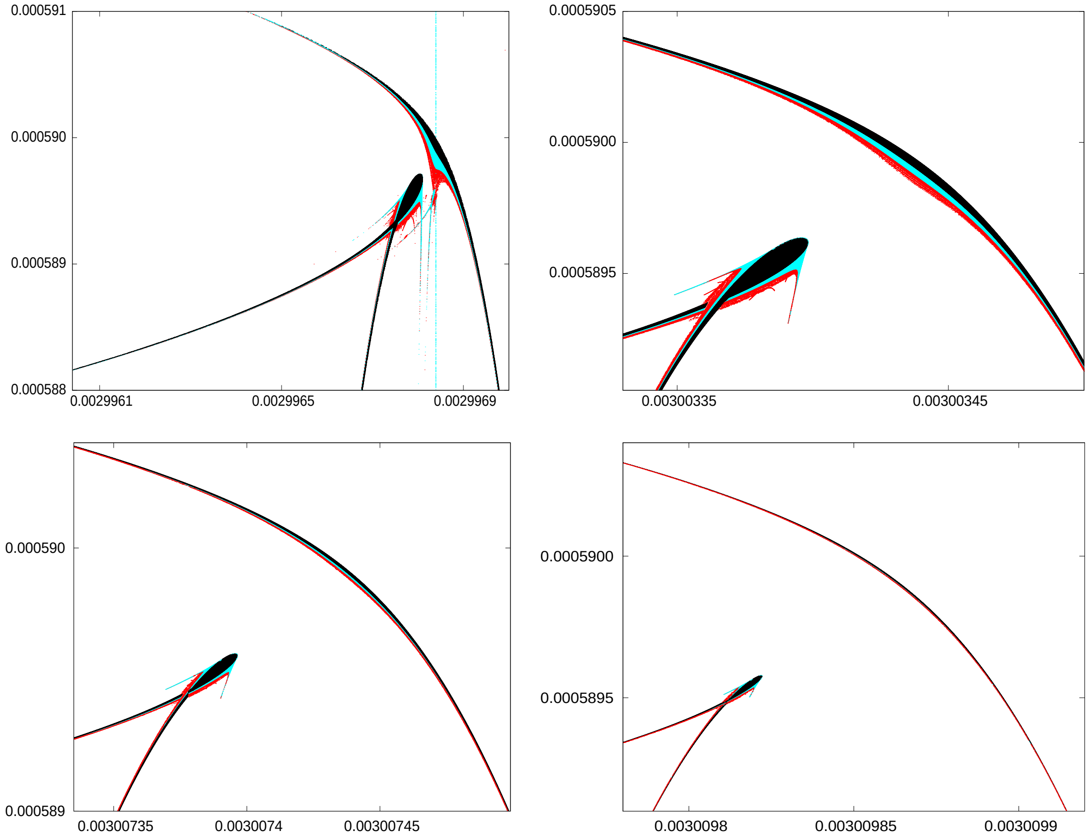

Figure 33: Some details of a cascade of stable configurations accumulating to a cubic tangency c_3 in $HZ^{\mp}$. It corresponds to a near horizontal cascade for a_2 close to 0.00059. We observe that in the limit of the cascade, i.e. for periods k large enough, we have a spring-area configuration. In black we plot the parameters (a_1, a_2) for which M has a 2-periodic sink, in pale blue those for which it has a 4-periodic sink and in red those parameters for which a periodic sink of period less than 2000 has been found.

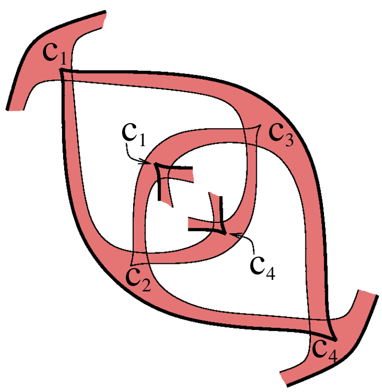

Figure 34: Sketch of the structure of the stability zones in the parameter plain. Detail of the joining strips and main stability islands shown in Fig. 31 related to the homoclinic zone $HZ^{\pm}$. The fattened lines correspond to fold bifurcation curves, the thin ones to flip bifurcation curves.

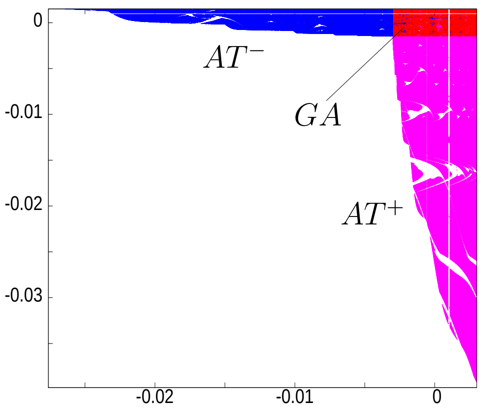

Figure 35: We show in blue and magenta the zones of the (a_1, a_2)-plane where we expect to have tail strange attractors AT^- and AT^+ respectively. The red color corresponds to the domain where global attractors GA are expected, that is, the `abcd` rectangle. In particular, we can identify the points `e` and `g` in Fig. 5. The white domains contained in these colored regions correspond to sinks.

5.3 Tail and global attractors

As a next step in our description of the parameter space we look for the region where tail strange attractors (together with periodic sinks) are expected. See Fig. 12 for an sketch of the manifolds giving rise to a (possible) tail attractor AT^+. We recall that the model (5) is defined in the union of the $s = 1$ and $s = -1$ domains and that in both domains the positive orientation of y points to the point O_s (or to the saddle if the domains are suitably chosen) of the Fig. 12. A tail attractor AT^+ (resp. AT^-) can be easily identified using the model (5) because the trajectories starting on W^u verify that

1. most of the iterates correspond to $s = 1$ (resp. $s = -1$) and have $y > 0$,
2. few iterates, however, have $s = 1$ (resp. $s = -1$) and $y < 0$,
3. there are no iterates with $s = -1$ (resp. $s = 1$) with $y > 0$.

Using this characterization one can easily identify the regions **18** and **26** in Fig. 5. These regions, for the selected values of b_1, b_2, ψ and A of the model, are shown in Fig. 35. Note that one can give explicit quantitative information on the size and concrete shape of these (and most of the other) zones in the parameter space as a function of the parameters of the model (5).

5.4 Details on Lyapunov exponents along a line in the parameter plane

To conclude the comments about the model and the parameter space, we give some details on Λ computed along the horizontal line $a_2 = 0$ in the (a_1, a_2)-plane with step in a_1 equal to 10^{-6}. This line is inside the homoclinic zone HZ^-. We use $z = 0.123456789$, $\eta = 10^{-5}$ and either $s = 1$ or $s = -1$ as i.c. The results are shown in Fig. 36. We remark that the fraction of values of a_1 such that $s = 1$ and $s = -1$ lead to different attractors is less than 1.9%.

Let us explain the Fig. 36 and give some details on the attractors observed. For values of $a_1 < -0.1432$ in Fig. 36 (2nd row left) we mainly observe an invariant curve as global attractor, with tiny sink intervals and, exceptionally, some SA. An example of such an invariant curve is shown in Fig. 37 (1st row left) for $a_1 = -0.145$.

As expected in a general intermittency route to chaos scenario, see [46, 16, 17] for an overview of some related results, the structure of the set of parameters for which the attractor is either a

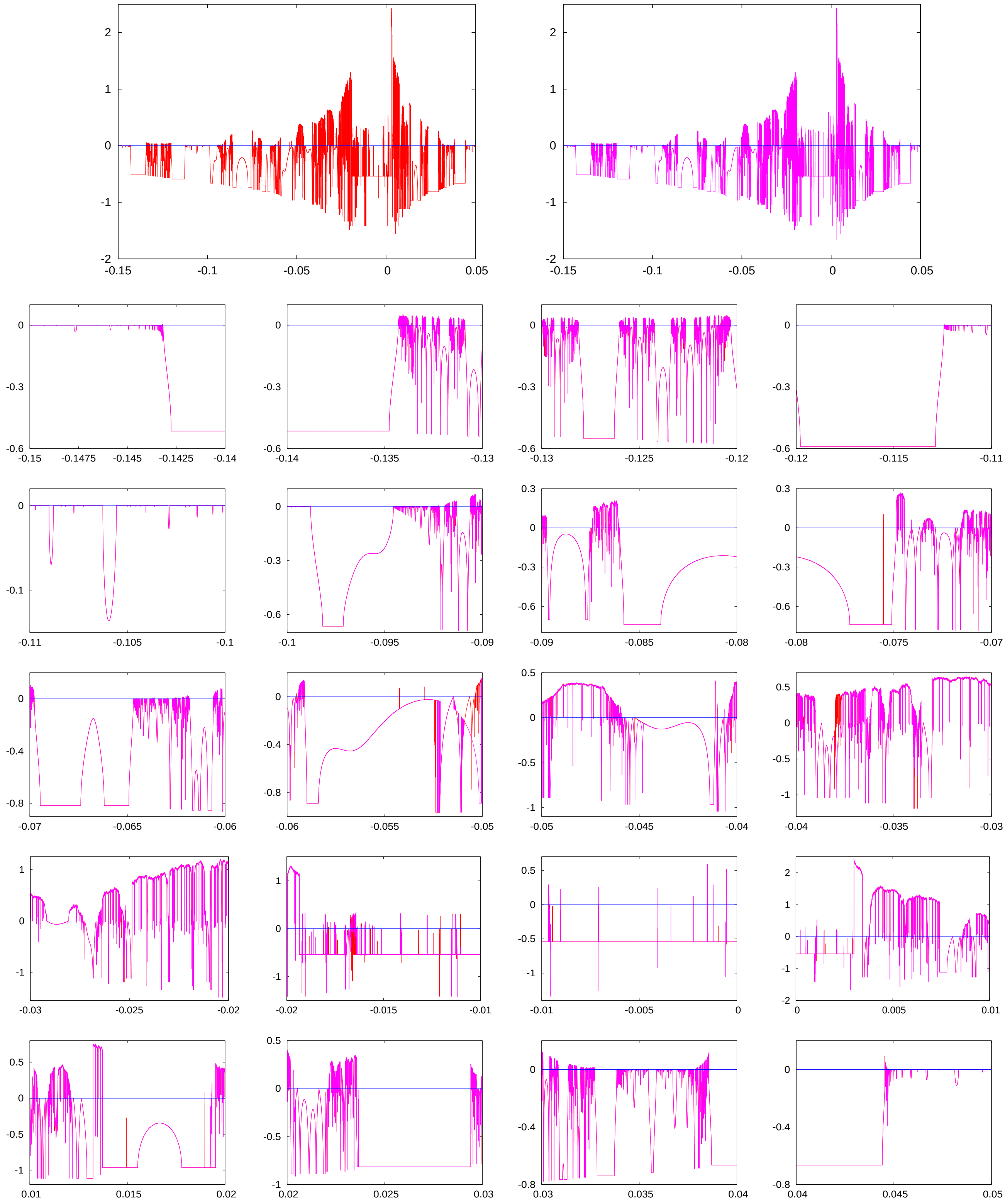

Figure 36: We display in the vertical axis Λ computed along $a_2 = 0$ as a function of a_1. The initial point of the orbit is $(0.5, 0, s)$. First row left: $s = 1$. Right: $s = -1$. All the other plots are magnifications of the previous ones where we display the cases $s = 1$ (red) and $s = -1$ (magenta) together. The values obtained using $s = 1$ and $s = -1$ coincide in many cases.

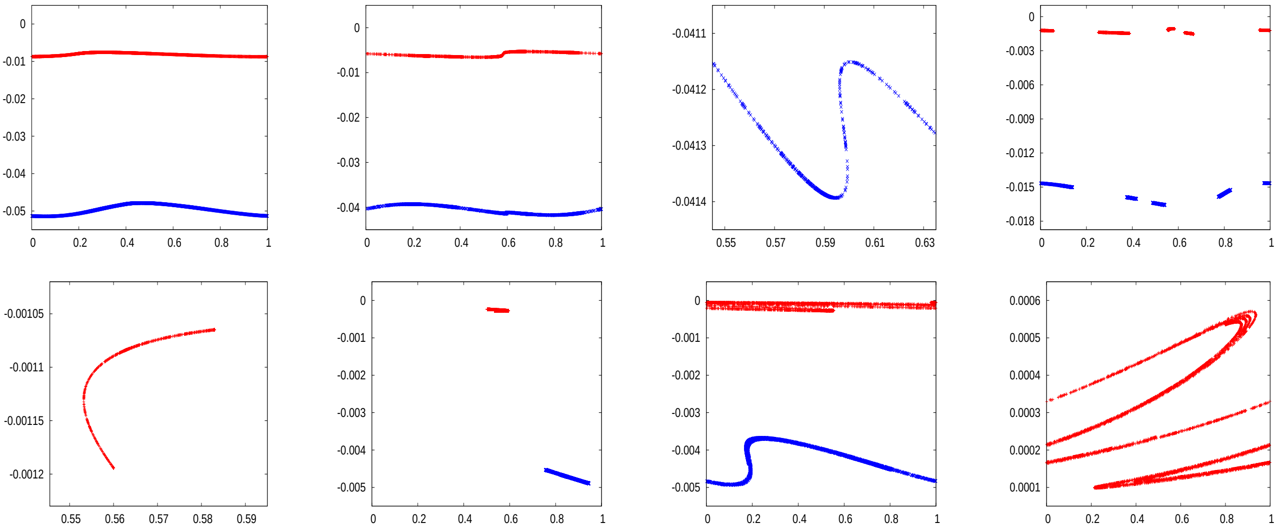

Figure 37: Detail of the attractors observed for the model (5) with $a_2 = 0$ for different values of a_1. We consider the i.c. $(z, \eta, s) = (0.123456789, 10^{-4}, 1)$ and we perform a transient of 2×10^5 iterates. Next we plot 10^5 iterates of the trajectory. The red (resp. blue) points correspond to iterates of the trajectory in the $s = 1$ (resp. $s = -1$) domain. From left to right, 1st row: invariant curve ($a_1 = -0.145$), SA of type A^* with a global nature ($a_1 = -0.129$), detail of the fold in the previous SA ($a_1 = -0.129$) and a SA of type A^* with a local periodic nature ($a_1 = -0.073$). 2nd row: Detail of the Hénon-like structure of the previous SA ($a_1 = -0.073$), SA of type A^* with a local nature ($a_1 = -0.034$), globalization of the previous SA ($a_1 = -0.033$) and a SA of type A^- ($a_1 = 0.006$).

SA or an invariant curve has a fractal structure. Accordingly, between the SA and/or invariant curves we detect many (infinitely many should exist) small platforms corresponding to periodic sinks of different period. For $-0.1431 \lesssim a_1 \lesssim -0.1344$, Λ shows a relatively large platform, see Fig. 36 (2nd row left and center left plots). This corresponds to a periodic sink attractor and, on this interval, the attractor has exactly one point in each one of the components of the FD for (5).

Now we comment on the observed SA. Around $a_1 \approx -0.1343$ we observe SA, that is $\Lambda > 0$. It is checked that the SA looks like a folded invariant curve. This mechanism giving rise to a SA was described in [16, 17]. We show the SA for $a_1 = -0.129$ in Fig. 37 center-left and a detail of the fold in center-right plots. We note that these SA have a global nature: they project on the z variable covering the full $[0, 1)$ interval, both for $s = 1$ and $s = -1$. We recall that the existence of SA of global nature was proved in [47] to be a prevalent property in the context of the one-parameter unfolding of a saddle-node cycle. In the present case the situation is similar for curves around the full figure-eight.

After a large platform, for $a_1 \approx -0.1125$, we observe again an invariant curve as a global attractor, see Fig. 36 (1st row right).

For $-0.1125 \lesssim a_1 \lesssim -0.092$ several transitions from invariant curve to periodic sinks and vice-versa are detected, see for example Fig. 36 (2nd row right and center-right plots).

In many of the illustrations in Fig. 36 one can detect transitions between SA and periodic sinks. Most of the SA detected have a local nature, that is, the projection on z consists of one or several intervals not covering $[0, 1)$. For example in Fig. 37 (right) we show the attractor for $a_1 = 0.073$. As stated in [50], these local nature attractors are persistent (the prevalence was also proved in [47]) in families unfolding a saddle-node point. These are local periodic Hénon-like attractors [48, 49] which appear for parameters at the end of a period-doubling cascade. These period-doubling cascades can be of direct or inverse type, can be total or only partial, and can be observed in many of the figures. See, e.g., [51] for details on the cascades of SA. For example,

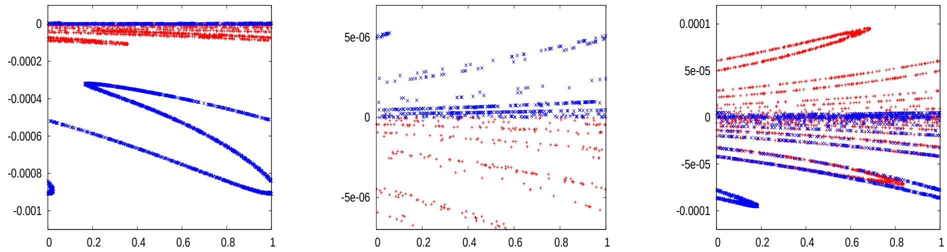

Figure 38: Detail of the attractors observed for the model (5) with $a_2 = -10^{-3}$. We consider the initial condition $(z, \eta, s) = (0.123456789, 10^{-4}, 1)$ and we perform a transient of 2×10^5 iterates. Next we plot 10^5 iterates of the orbit. In red we display the iterates in the $s = 1$ domain while the ones in blue are in the $s = -1$ domain. Left: Tail attractor of type AT^- ($a_1 = -0.0095$). Center: Magnification of the previous figure. Right: Global SA of type GA ($a_1 = 0$).

they can be clearly observed in the Fig. 36 (3rd row right, 4rd row center-left and right, 5th row right plot and 6th row left), where we also observe partial cascades which at some point undo the process.

Typically, by a small change of the parameter a_1 these local attractors globalize and become of global nature. This transition takes place for $a_1 = -0.034$ where a SA of local nature is shown in Fig. 37 (2nd. row center-left). For $a_1 = -0.033$ we observe in Fig. 37 (2nd. row center-right) how the attractor has a global nature.

All the SA commented before are related to the A^* SA. For $a_1 > 0$ we also observe SA of type A^- as shown in Fig. 37 (2nd. row right) for $a_1 = 0.006$.

As a final remark concerning SA, we note that for $a_2 = 0$ we have not detected tail attractors AT^- nor global strange attractors GA. This might be related to the properties of the model (5) for $a_2 = 0$. To show these “homoclinic” SA, consider for a moment $a_2 = -0.001$. For $a_1 = -0.0095$ we illustrate in Fig. 38 (left) a tail attractor of type AT^-. As can be observed in Fig. 38(center) some of the iterates of the orbit which are in the $s = -1$ domain have $y > 0$. Finally, for $a_1 = 0$ we show a global SA of type GA.

As it has been commented, between the SA and/or the invariant curve attractors we should have (infinitely many intervals of) periodic sinks. In Fig. 39 left we display some periods observed as a function of a_1, also along the line $a_2 = 0$. These are periods for the model, i.e., we count the number of points in the FD. The period for the figure-eight map is much higher. Near 68% of the values of a_1 taken in $[-0.15, 0.05]$ have sink attractors. Among them near 72% have either period 1 (and appear in $s = 1$, mainly for $a_1 > 0$) or period 2 (with one point in $s = 1$ and another in $s = -1$, mainly for $-0.1431 < a_1 < -0.02$, or with both points in $s = -1$ for $a_1 > -0.02$), independently of the initial value of s. In Fig. 39 left one can also check the behavior of the period as a function of the distance to a saddle-node bifurcation. If a s-n appears for a critical value $a_1 = a_{1,c}$, then the period of nearby sinks behaves as ctant$\times|a_1 - a_{1,c}|^{-1/2}$, as usual. See Appendix B for details. Of course, this behavior takes place around every one of the saddle-node bifurcations. In particular at the creation of sinks of the different periods by this mechanism.

In the Fig. 39 right we check in detail this behavior. We select the domain $a_1 \in [a_{1,c} - e^{-8}, a_{1,c} - e^{-20}]$, where $a_{1,c}$ is the value for the first appearance of period 2 with $a_1 > -0.15$ (see Fig. 36 second row left). In the selected range all the periodic orbits alternate points in $s = 1$ and $s = -1$. To fix ideas consider as relevant map M^2 instead of M and, hence, the periods are halved. A fixed point appears for $a_1 = a_{1,c}$ as a saddle-node bifurcation. To the left of $a_{1,c}$ (in the present interval; in other ranges exchange left by right) there are points of increasing period, tending to ∞ as $a_1 \to a_{1,c}^-$. They have rotation numbers of the form $1/k, k > k_1$. Also periodic points of

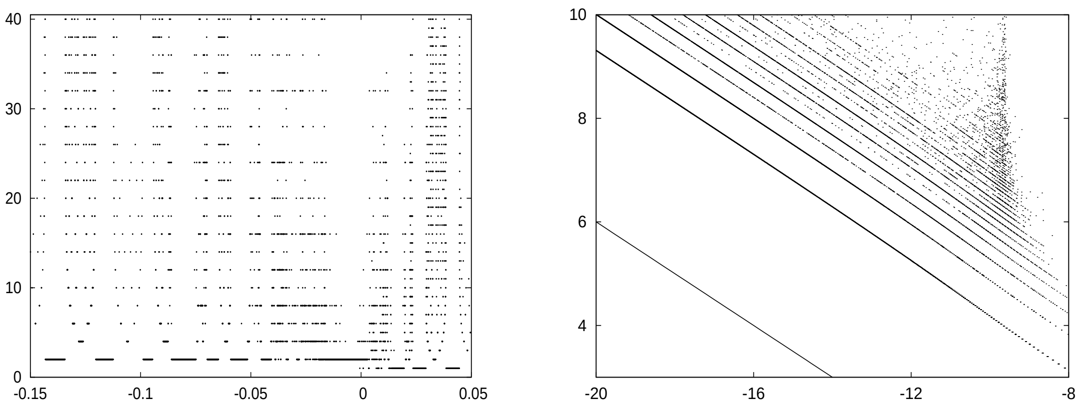

Figure 39: On the left we display the period (vertical axis) of the sinks detected (up to period 40) as a function of the parameter a_1 (horizontal axis). The right side shows log(Per) as a function of $\log(a_{1,c} - a_1)$, where Per denotes the period of the sink and $a_{1,c} \approx -0.143170413565918$ is the value for the first appearance of period 2 orbits with $a_1 > -0.15$. The line from $(-20, 6)$ to $(-14, 3)$ with slope $-1/2$ is just for reference. See also Fig. 36 second row left and the text for details.

rotation numbers of the form $j/k, k > k_j$ for $j = 2, 3, 4, \ldots$ should appear. The theoretical value k/j tends to behave as $\text{ctant}|a_1 - a_{1,c}|^{1/2}$. The agreement with Fig. 39 (right) is excellent. For the primary (with $j = 1$) periodic orbits detected, scanning the range $[a_{1,c} - e^{-8}, a_{1,c} - e^{-20}]$ the periods (under M) go from 24 to 11026. All of them have been detected without exceptions. The scanning has been made with a small constant step in the variable $\log(a_{1,c} - a_1)$. Furthermore, the range of values of a_1 for which a primary sink of period k (under M^2) exists, tends to be a given fraction of the distance between the creation of the sinks of period k and $k + 1$. See Appendix B for more quantitative details.

We also remark that, before reaching the value $a_{1,c}$ some SA have already been detected. They appear when the graph of the invariant curve attractor starts to develop folds and becomes a SA. This occurs for $a_1 \approx -0.143236$. From that point until $a_{1,c}$ the maximum value of Λ between the end of sinks of period $2k$ and the beginning of the ones of period $2k+2$ increases up to a maximum for $a_1 \approx -0.143190$ $(2k = 100)$ to decrease later tending to 0 when $k \to \infty$ and, hence, $a_1 \to a_{1,c}^-$.

The right hand side of Fig. 39 right deserves a comment. It is seen that for values of $\log(a_{1,c} - a_1)$ between ≈ -9.5 and -8 there are few sinks detected. The reason is that the width of the intervals of existence of these sinks is small compared with the step used to scan the variable a_1 in that zone.

We conclude this section by noting that all the predicted types of attractors have been observed in the model (5) and all the regions in the parameter space have been numerically obtained. The evolution of the parameter and phase space in terms of the parameters of the model (5) has been described providing a more detailed approach to the figure-eight bifurcation problem considered.

6 Conclusions and outlook

We have studied the bifurcation diagram related to the unfolding of a planar dissipative figure-eight under a non-conservative periodic forcing.

First, using a topological approach, the stair structure of one of the borders related to a homoclinic zone has been analyzed. We have shown that this is due to the distribution pattern of the cusp points in the parameter space. All the related bifurcations curves have been described.

Moreover, concerning the phase space of the system, all the possible different attractors have been described and we have discussed about the possible transitions between them.

Second, we have introduced a suitably adapted return map model to study the bifurcation problem. We have detected all the attractors predicted by the theory giving further quantitative details on the parameter zones and bifurcations that take place in the system. We think that such a more quantitative approach, which combines topological, analytical and numerical techniques, is essential for real applications.

This work leaves open several related questions to be studied in future works. Let us briefly mention some of them.

1. Concerning the bifurcation diagram in Fig. 5 it must be interesting to determine the boundary BD^{+-} of the region **24**, to study its evolution with respect the parameters and to determine the size of such a region.
2. Also, the mechanisms of creation/destruction of folds, specially in the regions **2,9,17,24,25, 31** and **32**, should be analyzed.
3. Another question concerns the rate of accumulation of the stairs that form the lines $L_{1,2}^{\pm;\mp}$ when approaching to the limit square `abcd`. This might be relevant because of the universality of the figure-eight problem studied.
4. The same universality criterion applies to the amazing structure displayed in Fig. 31, which certainly deserves further investigations to be clarified.
5. A related question to the previous item concerns the detachment mechanisms of the spring areas of stability from a cross-road configuration. It might necessary to look for more global return map close to cubic tangencies (or local but to higher order, for example considering different types of generalized cubic maps).
6. Another point is related to the orientation-reversing case, see Fig. 41 right in Appendix A. Note that, in such a situation, the stability domains are related to cubic tangencies of type "+" and "−" and, consequently, one expects the stability configurations to be different from those displayed in Fig. 31.

We believe that the techniques presented in this work, which can be adapted to other situations and problems (including multidimensional ones), can be also useful for further investigations in these (and maybe other) directions.

Acknowledgments

This work has been supported by grants MTM2006-05849/Consolider (Spain), MTM2010-16425 (Spain) and 2009 SGR 67 (Catalonia). SG was supported by the Russian Federation Government grant, contract No.11.G34.31.0039 and grants of RFBR No.10-01-00429, 11-01-00001 and 11-01-97017 r-povoljie. The authors are indebted to D. Turaev and J.C. Tatjer for their comments and suggestions. The computing facilities of the Dynamical Systems Group of the Universitat de Barcelona have been largely used.

A On cubic homoclinic tangencies: a review of results.

Bifurcations of cubic homoclinic tangencies were studied in [39] for the general case (see also [40, 41, 52]). Here we give some review of results from [39]. However, for simplicity, we consider only the two-dimensional case (although, in [39] a multidimensional case was studied).

Let F_0 be a two-dimensional C^r-smooth, $r \geq 6$,[5] diffeomorphism satisfying the following conditions.

- C1) F_0 has a saddle fixed point O with multipliers λ and γ such that $0 < \lambda < 1 < \gamma$;
- C2) the saddle value $\sigma \equiv \lambda\gamma$ is less than 1; [6]
- C3) the stable W_0^s and unstable W_0^u invariant manifolds of O have a cubic tangency at the points of some homoclinic orbit Γ_0.

Let F_μ, $\mu = (\mu_1, \mu_2)$ be a two parameter family which unfolds generically the initial cubic homoclinic tangency, i.e. the parameters μ_1 and μ_2 can be chosen as the splitting parameters of $W_0^s(\mu)$ and $W_0^u(\mu)$ (see (7) below for the concrete role of μ) with respect to some point of the homoclinic orbit Γ_0.

Consider a small fixed neighborhood U of the contour $O \cup \Gamma_0$. Such a neighborhood U is the union of a small neighborhood (disk) U_0 containing the point O with a number of small disks surrounding those points of the orbit which do not belong to U_0.

The main problem here is to study bifurcations of single-round periodic orbits from U within the framework of the family F_μ. Every point of such an orbit can be considered as the fixed point of the corresponding first return map.

A.1 Derivation of the return map

As usual, the first return maps are constructed as a composition of two maps: the local map $T_0(\mu)$, where $T_0 \equiv F_\mu \big| U_0$, defined on U_0, and the global map $T_1(\mu) : U_0 \to U_0$ defined by the orbits close to a global piece of Γ_0. Then the first return maps can be represented as $T_k = T_1 T_0^k$ for every sufficiently large integer k ($k = k_0, k_0 + 1, ...$).

For simplicity, we assume that there are C^r-coordinates in U_0 in which the local map T_0 is linear, that is, given by $\bar{x} = \lambda x,\ \bar{y} = \gamma y$.[7] Accordingly, the map T_0^k can be written as $x_k = \lambda^k x_0,\ y_k = \gamma^k y_0$ or as $x_k = \lambda x_0,\ y_0 = \gamma^{-k} y_k$. The latter form is called *the cross-form* of the map T_0^k.

For $\mu = 0$, let $M^+(x^+, 0) \in W_{loc}^s$ and $M^-(0, y^-) \in W_{loc}^u$ be a pair of homoclinic points of the orbit Γ_0 and Π^+ and Π^- be small neighborhoods of the points M^+ and M^- respectively. Let q be

[5] such smoothness is required for the correct study of certain codimension 2 bifurcations of periodic orbits.

[6] in fact, we only exclude the case $\sigma = 1$, the case $\sigma > 1$ can be reduced to the case $\sigma < 1$ for the inverse map.

[7] As it is well-known, a sufficiently smooth linearization is not always possible. However, we can introduce C^r-coordinates on U_0 in which the local map $T_0(\mu)$ has the so-called *main normal form*, [39, 53, 54],

$$\bar{x} = \lambda x + h_1(x, y, \mu) x^2 y, \quad \bar{y} = \gamma y + h_2(x, y, \mu) x y^2.$$

Then the map T_0^k for all k can be written in the cross-form as follows

$$x_k = \lambda^k x_0 + \mathcal{O}(\lambda^k \gamma^{-k}), \quad y_0 = \gamma^{-k} y_k + \mathcal{O}(\gamma^{-2k}),$$

where $(x_k, y_k) = T_0^k(x_0, y_0)$. These formulas show that there are no principal differences between the linear and nonlinear cases.

such integer that $M^+ = F_0^q(M^-)$. Then the global map $T_1(\mu) = F_\mu^q : \Pi^- \to \Pi^+$ can be written as

$$\begin{array}{l} \bar{x} - x^+ = ax + b(y - y^-) + \mathcal{O}\left(x^2 + (y - y^-)^2\right), \\ \bar{y} = \mu_1 + \mu_2(y - y^-) + cx + d(y - y^-)^3 + \mathcal{O}\left(x^2 + |x||y - y^-| + (y - y^-)^4\right), \end{array} \tag{7}$$

where $(x, y) \in \Pi^-$, $(\bar{x}, \bar{y}) \in \Pi^+$, $d \neq 0$ since the homoclinic tangency is cubic and $bc \neq 0$, since the map T_1 is diffeomorphism.

When a cubic tangency splits, new quadratic tangencies can appear. This fact takes place for our family F_μ for which the following result, stated in [39] holds.

Proposition A.1. *On the (μ_1, μ_2)-parameter plane there exists a bifurcation curve B_0 given by*

$$\mu_1 = \pm 2d \left[-\frac{\mu_2}{3d}(1 + O(\mu)) \right]^{3/2}, \tag{8}$$

such that at $\mu \in B_0$ the map F_μ has a close to Γ_0 (single-round) homoclinic orbit consisting of points of quadratic tangency of W_μ^u and W_μ^s.

Now we consider single-round periodic orbits and study their bifurcations. For every such an orbit one can consider its first return map having the following representation

$$T_k = T_1 T_0^k \;:\; \Pi^+ \to \Pi^- \to \Pi^+,$$

where k can take any integer value beginning at some $\bar{k}$, i.e. $k \in \{\bar{k}, \bar{k}+1, \dots\}$. Denote the coordinates (x, y) in Π^+ and Π^- as (x_0, y_0) and (x_1, y_1), respectively. From $(x_1, y_1) = T_0^k(x_0, y_0)$ it follows that $x_1 = \lambda^k x_0$ and $y_0 = \gamma^{-k} y_1$. Thus, by (7), we can write the map T_k in cross-coordinates (x_0, y_1) as follows

$$\begin{array}{l} \bar{x}_0 - x^+ = a\lambda^k x_0 + b(y_1 - y^-) + \dots, \\ \gamma^{-k}\bar{y}_1 = \mu_1 + \mu_2(y_1 - y^-) + d(y_1 - y^-)^3 + c\lambda^k x_0 + \dots \end{array} \tag{9}$$

Introduce shifted coordinates $\xi = x_0 - x^+ + \nu_1$, $\eta = y_1 - y^- + \nu_2$, where $\nu_i = O(\lambda^k)$ for $i = 1, 2$, in such a way that the first equation does not contain constant terms and the second one quadratic terms in η. Then system (9) is recast as follows

$$\begin{array}{l} \bar{\xi} = a\lambda^k \xi + b\eta + O\left(\lambda^{2k}\xi^2 + \eta^2\right), \\ \bar{\eta} = m_1 + m_2\eta + d\gamma^k\eta^3 + c\lambda^k\gamma^k\xi + \gamma^k O\left(\lambda^{2k}\xi^2 + \lambda^k|\xi\eta| + |\eta|^4\right), \end{array} \tag{10}$$

where $m_1 = \gamma^k\left(\mu_1 - \gamma^{-k}y^-(1 + \dots)\right)$, $m_2 = \gamma^k\left(\mu_2 + \mathcal{O}(\lambda^k)\right)$. Now we rescale coordinates as follows

$$\psi \;=\; \frac{b}{\sqrt{|d|}}|\gamma|^{-k/2}X, \;\; \eta \;=\; \frac{1}{\sqrt{|d|}}|\gamma|^{-k/2}Y. \tag{11}$$

Then the system (10) is recast as

$$\begin{array}{l} \bar{X} = Y + O(|\gamma|^{-k/2}), \\ \bar{Y} = M_1 + M_2 Y + \alpha Y^3 + bc\lambda^k\gamma^k X + O(|\gamma|^{-k/2}), \end{array} \tag{12}$$

where $\alpha = \operatorname{sign} d$,

$$M_1 = \sqrt{|d|}\gamma^{3k/2}\left(\mu_1 - \gamma^{-k}y^-(1 + \dots)\right), \;\; M_2 = \gamma^k\left(\mu_2 + O(\lambda^k)\right). \tag{13}$$

Evidently, the rescaled parameters M_1 and M_2 for large k can take arbitrary finite values when varying μ_1 and μ_2 near zero. Also, since the rescaling factors in (11) are asymptotically small as $k \to \infty$, the domain of definition for new coordinates X and Y is (asymptotically) large. Then, since $|\lambda\gamma| < 1$, the rescaled map (12) is asymptotically close to the following cubic map

$$\bar{X} = Y, \;\; \bar{Y} = M_1 + M_2 Y + \alpha Y^3 \tag{14}$$

which is, in fact, a one-dimensional cubic map with $\alpha = \text{sign } d$. Thus, we can now recover the bifurcations of the fixed points. However, we need to take into account that our map is a diffeomorphism. Therefore, we have to keep the small term $bc\lambda^k\gamma^k X$ in (12). That is, we must consider the normal rescaled form as the following two-dimensional diffeomorphism

$$\bar{X} = Y, \;\; \bar{Y} = M_1 + M_2 Y + \beta_k X + \alpha Y^3, \tag{15}$$

where $\beta_k = bc\lambda^k\gamma^k$ is the (main part of the) Jacobian of the first return map T_k.

A.2 Bifurcation diagram of the return map (15)

The bifurcation diagram for the map (15) is shown in Fig. 40 (a) for the case $\alpha = +1$ and in Fig. 40 (b) for the case $\alpha = -1$. The bifurcation curves are: L^+ – for the fixed points with the multiplier $+1$; L^- – for the fixed points with the multiplier -1; $C^+_{1,2}$ – for the period 2 points with the multiplier $+1$; $C^-_{1,2}$ – for the period 2 points with the multiplier -1 (second period doubling). Their equations are given by

$$\begin{aligned}
&L^+: \;\; M_1 = \pm\frac{2}{3}\left(\frac{1+\beta_k - M_2}{3\alpha}\right)^{3/2} \\
&L^-: \;\; M_1 = \pm\frac{2}{3}\left(\frac{-1-\beta_k - M_2}{3\alpha}\right)^{1/2}(2+2\beta_k - M_2) \\
&C^+_{1,2}: \;\; M_1 = \pm\frac{2}{3\sqrt{3}}\left(-M_2 - 2(\beta_k+1)\right)^{3/2} \;\; \text{in the case } \;\alpha = +1 \\
&C^+_{1,2}: \;\; M_1 = \pm\frac{2}{3\sqrt{3}}\left(M_2 + 2(\beta_k+1)\right)^{3/2} \;, M_2 > -\frac{2}{3}(\beta_k+1), \;\text{in the case } \;\alpha = -1 \\
&C^-_{1,2}: \;\; M_1^2 = \frac{1}{216\alpha}\left[6(\beta_k+1) + M_2 \pm S\right]^2\left[-5M_2 - 6(\beta_k+1) \pm S\right], \;\text{ where} \\
&\qquad\qquad S = \sqrt{(3M_2 + 2\beta_k + 2)^2 - 8(\beta_k^2+1)}.
\end{aligned} \tag{16}$$

We should remember that β_k is small and it tends to zero geometrically when $k \to \infty$.

The regions I Fig. 40(a) and (b) correspond to those values of the parameters M_1 and M_2 for which the map (15) has only one fixed point and has no periodic orbits. In both cases this point is a saddle. However, in the case $\alpha = +1$, it is the saddle-plus (both multipliers are positive), and in the case $\alpha = -1$, the point is the saddle-minus (both multipliers are negative). The dashed regions in Fig. 40(a) and (b) correspond to those values of the parameters M_1 and M_2 at which the map (15) with $\alpha = +1$ and $\alpha = -1$, respectively, has an asymptotically stable fixed point. These regions are bounded by the curves L^+ and L^-.

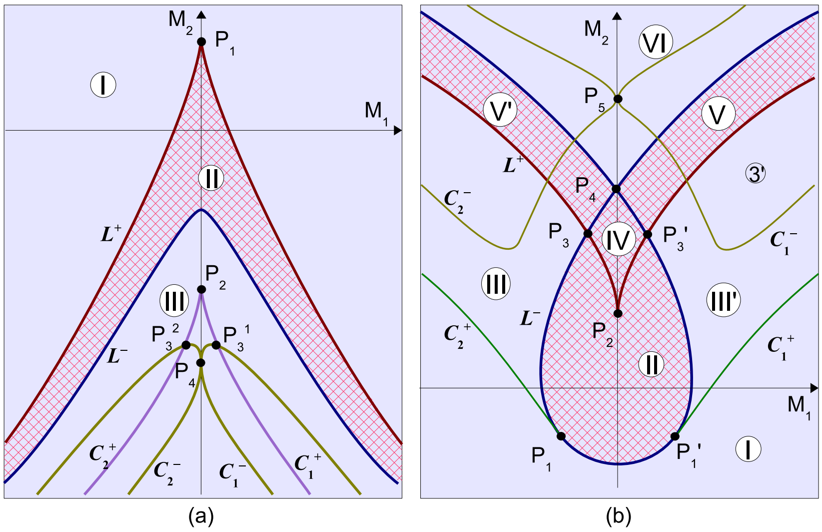

Figure 40: Bifurcation curves of the map $T_k(\mu)$: a) the case of tangency of "+" type: $d > 0, \gamma^k > 0$, b) the case of tangency of "−" type: $d < 0, \gamma^k > 0$.

The stable fixed points appear in different ways depending on the case. In the case $\alpha = +1$ such points are born under the saddle-node bifurcation through the curve L^+ and, in the symmetric case $M_1 = 0$, a pitch-fork bifurcation $I \to II$ takes place when crossing the cusp point P_1.

In the case $\alpha = -1$, at the transition $I \to II$ (when crossing the segment $[P_1, P_1']$ of the curve L^-), a period doubling bifurcation occurs: here the fixed point becomes stable in II and two saddle points of period two are born in its neighborhood. Along the path I $\to$ III(III') $\to$ II on the parameter plane, we meet, first, a saddle-node bifurcation of period 2 when crossing the line C_1^+ or C_2^+. This bifurcation is non-degenerate, and, as result, a stable period 2 point appears when $(M_1, M_2) \in$ III (III'). In turn, this period 2 point undergoes a period doubling bifurcation on the curve L^-: the stable period 2 cycle merges with the saddle fixed point and, as result, the latter becomes stable at $(M_1, M_2) \in$ II. However, when the parameters move to the domain IV, one more stable fixed point appears due to a saddle-node bifurcation when crossing the curve L^+. Thus, at $(M_1, M_2) \in$ IV two stable fixed points exist and here the cusp point P_2 corresponds to the pitch-fork bifurcation: 1 stable fixed point gives rise to 2 stable and 1 saddle fixed points. For values of the parameters from the domain V(V'), the map has again only one stable fixed point, since the other stable point undergoes a period doubling bifurcation at the transition IV$\to$ V(V').

A.3 Cascades of periodic sinks at a cubic homoclinic tangency

Having into account the relations (13) and the formulas (8) and (16) for the bifurcation curves, the following result was obtained in [39].

Theorem A.1. *Concerning the existence of a cascade of periodic sinks at a cubic homoclinic tangency, the following two assertions hold:*

(i) In any neighborhood of the origin of the (μ_1, μ_2)-parameter plane, there exist infinitely many domains S_k accumulating, as $k \to \infty$, at a bifurcation curve B_0 and such that the map F_μ has at $(\mu_1, \mu_2) \in S_k$ an asymptotically stable single-round periodic orbit of period k.

(ii) The curve B_0 has the equation (8). The boundary of the domain S_k consists of the curves

L_k^- and L_k^+ whose equations are as follows[8]

$$
\begin{aligned}
L_k^+ :\quad \mu_1 &= \gamma^{-k} y^-(1+\dots) \pm 2d \left(\frac{\gamma^{-k}(1+\dots) - \mu_2}{3d} \right)^{3/2}, \\
L_k^- :\quad \mu_1 &= \gamma^{-k} y^-(1+\dots) \pm \frac{2}{3} \left(\mu_2 - 2\gamma^{-k}(1+\dots)\right) \sqrt{\frac{-\mu_2 - \gamma^{-k}(1+\dots)}{3d}},
\end{aligned}
\tag{17}
$$

where the dots stand for terms tending asymptotically to zero as $k \to \infty$.

The bifurcation diagram associated to this theorem is shown in Fig. 41 left and center plots. The stability regions S_k are marked by the hatching. They correspond to the stability zones of Fig. 40: either zone II for the case $d > 0, \gamma^k > 0$ (a), or zone II∪IV∪V∪V' (b), in the rescaled parameters M_1 and M_2. Since these zones have size of order 1 in Fig. 40, then their sizes in the (μ_1, μ_2)-parameter plane are of order γ^{-k} along the μ_2-direction and order $\gamma^{-3k/2}$ along the μ_1-direction. Thus, we can see that, although the stability zones near cubic tangencies are asymptotically small, they are larger than those in the case of a quadratic homoclinic tangency, where such zones have order γ^{-2k} along the μ_1-direction.

Remark. Similarly one derives a return map when $\gamma < 0$ (e.g. orientation reversing case), see [39]. It might happen that both sides of the cascade show a different type of stability area. This is illustrated, for completeness, in Fig. 41 right.

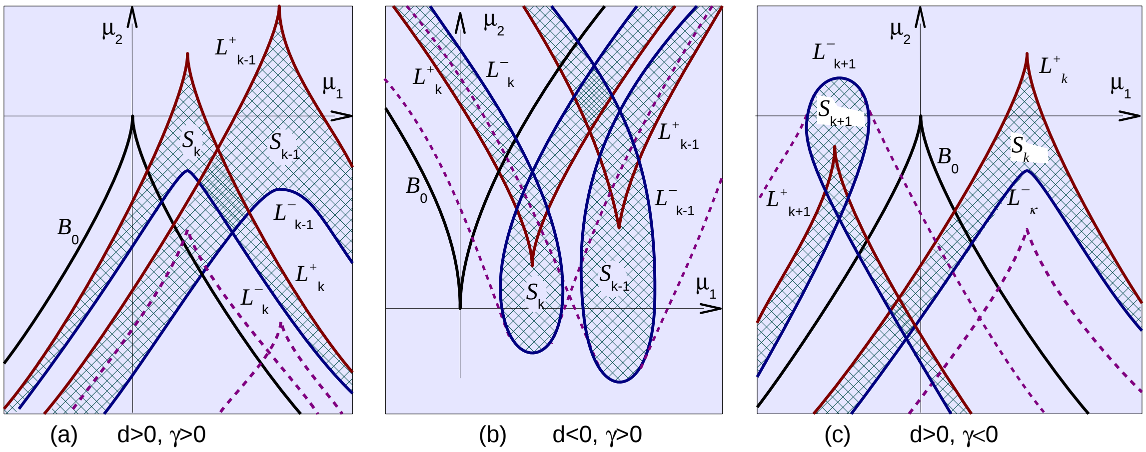

Figure 41: Main bifurcations curves near a point $\mu_1 = \mu_2 = 0$ that corresponds to a cubic homoclinic tangencies. We display here also the curves C_{k1}^+ and C_{k2}^+ (the dotted lines) from (16).

A.4 The cross-road scenario

The map (15) is obtained as a limit return map for $k \to \infty$. The ignored terms are sufficiently small for k large enough meaning that, at the end of a cascade of cusp points accumulating to a concrete cubic tangency, the stability area expected should be either a saddle-area of stability or an spring-area one. However, in concrete applications these limit cases might be observed for large values of k and other scenarios, giving rise to other types of stability area, can be observed

[8] see the corresponding equations for the curves L^- and L^+ (16) in the rescaled parameters M_1 and M_2

for moderated values of k, see [17]. For completeness, here we comment on the cross-road scenario because this is one of the observed in the Fig. 31 for the model (5).

Consider a two parameter family of maps $f_{a,b} : \mathbb{R}^2 \to \mathbb{R}^2$, $a, b \in \mathbb{R}$. For a fixed $k \in \mathbb{N}$, the family F^k_μ is an example of such a biparametric family. Denote by S the set of fixed points of $f_{a,b}$, that is, $S = \{(a, b, x, y) \in \mathbb{R}^4$ such that $f_{a,b}(x, y) = (x, y)\}$, and denote by $\Lambda : S \to \mathbb{R}$ the map

$$\Lambda(a, b, x, y) = \frac{\mathrm{tr} Df_{a,b}}{\det Df_{a,b}(x, y) + 1}.$$

Let (a_0, b_0, x_0, y_0) be a regular point of S and assume that $f_{a,b}$ has a cusp point at (x_0, y_0) for $(a, b) = (a_0, b_0)$ of "$-$" type. We say that $f_{a,b}$ displays a cross-road area near (a_0, b_0, x_0, y_0) if there is a domain $W \subset S$ such that

1. the map $\Lambda|_W$ has one, and only one, non-degenerated critical point of saddle type (a_1, b_1, x_1, y_2) with $-1 < \Lambda(a_1, b_1, x_1, y_2) < 1$, and

2. (a_0, b_0, x_0, y_0) is the only one cusp bifurcation point in W.

If $f_{a,b}$ displays a cross-road area, then the projection onto the (a, b)-plane of S gives a bifurcation pattern like the one shown in Fig. 32, which corresponds to the pattern observed in Fig. 31 related to the cascade of the cubic tangency points $c_1, \ldots, c_4$ of "$-$" type.

At the end of the cascade of cusp points which accumulate to a cubic tangency point of "$-$" type, we should observe areas of stability of spring area type. The reader is referred to [27, 28] for a description of one of the possible scenarios to evolve from a cross-road area to a spring area.

It turns out that the cross-road scenario appears quite frequently in codimension 2 unfoldings near a cubic tangency. The universal model (5) considered in this work is an example of such a fact. However, the cross-road scenario might be (a priori) expected in codimension 3 unfoldings near a quartic tangency instead. See related comments in [17]. Further investigations are required to provide an explanation of the so common presence in (5) and other scenarios.

B Creation of sinks close to a saddle-node bifurcation in $\mathbb{S}^1$

As pointed out in Section 5, when the attractor is an invariant curve and the rotation number tends to zero periodic sinks of period k and rotation number $1/k$ show up generically. They appear at a saddle-node (s-n) bifurcation of the k-th power of the map and are destroyed at another such s-n. Using the k-th power of the map the process is repeated again and again in a self-similar way. Also sinks of rational rotation number of the form $j/k, k \to \infty$ are found generically.

Here we want to discuss some simple scaling properties. To this end we consider an analytic diffeomorphism, $F_a(x)$, in $\mathbb{S}^1 = \mathbb{R}/\mathbb{Z}$ of the form

$$x \mapsto x + a + bf(x) \text{ with } f(x) > 0\ \forall x \in \mathbb{S}^1 \setminus \{0\},\ f(0) = 0,\ df/dx(0) = 0,\ d^2f/dx^2(0) > 0,\ b \gg a > 0. \tag{18}$$

Note that it is not restrictive to assume $d^2f/dx^2(0) = 2$, which amounts to rescale b. For a fixed value of b we are looking for the behavior when $a \to 0$. Let $a^{(k)}_{sni}, a^{(k)}_{snf}$ be the initial and final s-n of creation and destruction of sinks of period k. We want to emphasize that any analytic diffeomorphism in $\mathbb{S}^1$ is of the form $x \mapsto x + a + f(x)$. However, we keep the expression depending on b to make clear that some results depend on b for a fixed f. We have the following result.

Proposition B.1. *Assuming the analytic diffeomorphism $x \mapsto F_a(x) = x + a + bf(x)$ satisfies the properties in (18) then*

i) the values of $a_{sni}^{(k)}$ and $a_{snf}^{(k)}$ behave generically as $c_1/k^2 + \mathcal{O}(1/k^3)$ for k sufficiently large,

ii) the ratio $(a_{sni}^{(k)} - a_{snf}^{(k)})/(a_{sni}^{(k)} - a_{sni}^{(k+1)})$ tends to a limit (depending on b) when $k \to \infty$, and

iii) the minimal value of the multiplier of the periodic orbits of period k for $a \in [a_{snf}^{(k)}, a_{sni}^{(k)}]$ tends to a limit (also depending on b) when $k \to \infty$.

Proof. As a first step, for a given value of a we consider a vector field $x' = h(x)$ defined on an interval $[-m(a), m(a)]$ such that the time-1 flow $\varphi_{t=1}^h$ of h in that interval differs from F_a by a quantity $\mathcal{O}(a^2)$. This vector field can be obtained by the usual periodic suspension and averaging technique (see, e.g., [55]) based on [56]. If a is negligible in front of $m(a)$ the map F_a differs from the identity by a quantity $\mathcal{O}(m(a)^2)$ and, hence, the difference between F_a and $\varphi_{t=1}^h$ is $\mathcal{O}(\exp(-c/m(a)^2))$ for some $c > 0$. This will be $\mathcal{O}(a^2)$ if we take $m(a) = \mathcal{O}(|\log(a)|^{-1/2})$ which is, indeed, much larger than a for a sufficiently small. It is also clear that the same interval $[-m(a), m(a)]$ can be used for some range of smaller values of a, with the same bounds. Later we shall be more precise on the size of that range.

Any point $p \in [F_a^{-1}(m(a)), m(a)]$ can be parametrized by a "local time" $z \in [0, 1]$ such $\varphi_{t=z}^h(F_a^{-1}(m(a))) = p$. Due to the errors in the approximation and the size of the vector field, the error in z can be bounded by $\mathcal{O}(a^2|\log(a)|)$. As we shall see, it is necessary to bound all the errors in time. Then, any point q in the circle, say from the vicinity of $m(a)$ to the vicinity of $2\pi - m(a)$ can be parametrized as follows. Compute preimages of q under F_a until it lands in $[F_a^{-1}(m(a)), m(a)]$, for the first time, at a point p. Let j be the number of required preimages. Then, the parameter associated to q will be $j + z$. The point $F_a^{-1}(m(a))$ can be seen as the "origin" of the parametrization. But it is clear that this origin is arbitrary and later it will be changed to a more convenient place. For any point in an interval of the form $[r, F_a(r)]$ we can refer to the parameter simply as z, without explicit mention of j if it is not necessary.

It is also clear that preimages of points in $[F_a^{-1}(m(a)), m(a)]$ under F_a will reach the vicinity of points "to the left" of $x = 0$ but at a small distance from $x = 0$, for the first time, under $\tilde{j}$ iterates and we can associate to one of these points a parameter of the form $-\tilde{j} + \tilde{z}$. The condition for periodicity is to have a point to the left of $x = 0$ with (fractional part of the) parameter $\tilde{z}$ such that when it returns nearby after making a tour to the circle, it has (fractional part of the) parameter equal to z with $z = \tilde{z}$. Any equivalent formulation can be used. Then this point will have period $j + \tilde{j}$.

The steps to impose the periodicity condition are as follows:

1. First we take a small quantity m, independent of a, and consider a point of parameter z in $[m, F_a(m)]$. It is not restrictive to assume that m has parameter $z = 0$ (by redefining the origin of z) and that the point $x = m$ is mapped, by iteration under F_0 to the point of $x = -m$. Otherwise one can do a tiny change in m (of the order of m^2). By iteration under F_0 (note that that map does not depend on a) of the point of parameter z we reach a point close to $-m$. The final one has parameter $\tilde{z} := z + g(z)$, where $g(z)$ measures the "distortion" produced by the fact that F_0 (in the "outer" part, away from $x = 0$) generically differs from a flow. By construction $g(0) = 0, g(1) = 0$. Let N_0 be the number of iterates, depending only on bf. As it is fixed, independent of a, the error in position due to the use of F_0 instead of F_a is $\mathcal{O}(a)$ and also the error in time $\mathcal{O}(a/(bm^2)) = \mathcal{O}(a)$. The map $z \mapsto \tilde{z}$ can be named as "outer" or "gluing" map.
2. Then we consider iterations between the vicinity of $m(a)$ and the vicinity of m, but again using F_0 instead of F_a. The number of iterates, N_1, is constant (it depends only on bf) for

relatively large ranges of a. Indeed, if a point near m lands near $m(a)$ under $F_0^{-N_1}$, in one more iterate under F_0^{-1} will be close to $m(a)-bm(a)^2$. If we write this value as $m(a')$ one has $a'=a\mathcal{O}(\exp(-2b|\log(a)|^{1/2}))$, as shown by a simple computation. Then, for a relatively large range below a' we shall need N_1+1 iterates instead of N_1 and so on. The errors in position and time due to the use of F_0 instead of F_a will be bounded later. In a completely similar way we can consider the number of iterates, N_{-1} required to go from the vicinity of $-m$ to the vicinity of $-m(a)$ under F_0 and to derive the corresponding error bounds.

3. Next we consider the passage from the vicinity of $-m(a)$ to the vicinity of $m(a)$. To this end we use the flow approximation and then we bound the errors due to the difference between F_a and $\varphi^h_{t=1}$. For concreteness we consider as point near $m(a)$ the point $F_0^{-N_1}(m)$ and as point near $-m(a)$ the point $F_0^{N_{-1}}(-m)$. As discussed, these points do not depend on a (at least for relatively large ranges of a; going below these ranges requires to increase them by 1 unit and then they can be used again in a relatively large domain in a). But the flow φ^h_t certainly depends on a. Let us denote as $t(a)$ the time of passage from $F_0^{N_{-1}}(-m)$ to $F_0^{-N_1}(m)$. It is clear that $t(a)$ increases when a decreases.
4. Finally let us take a point with parameter $z\in[0,1)$ near m. It returns to a point with parameter equal to $z+N_0+g(z)+N_{-1}+t(a)+N_1$ plus the errors mentioned in 1., 2. and 3. above that we denote simply as E. To have a periodic point of period k the new parameter must be $k+z$. Generically the function g is not identically zero (see also the comments concerning Fig. 42 right, below). Let $g_1=\min_{z\in[0,1]}g(z)\le 0$, $g_2=\max_{z\in[0,1]}g(z)\ge 0$, and, for simplicity, let us introduce $N=N_0+N_{-1}+N_1$. Therefore the largest value of a to have a point of period k (that is $a=a^{(k)}_{sni}$) is obtained when $N+g_2+t(a)+E=k$, while the smallest one (that is $a=a^{(k)}_{snf}$) is obtained when $N+g_1+t(a)+E=k$.

To bound the errors in the different steps we recall that in 1. they are $\mathcal{O}(a)$. Concerning 2., as we use F_0 instead of F_a we have an error of size a at each iterate. Let $x_0,x_1,x_2,\dots$ the points in an orbit of F_0 between the vicinity of $m(a)$ and the vicinity of m. A local error a when computing x_1 will be amplified by

$$\Pi_{j=1}^{N_1-1}DF_0(x_j)=\Pi_{j=1}^{N_1-1}(1+2bx+\mathcal{O}(x^2))=\exp\left(\sum_{j=1}^{N_1-1}(2bx+\mathcal{O}(x^2))\right),$$

where the sum can be estimated by the integral $\int_{m(a)}^{m}2bx\,dx/(\hat{b}x^2)$, where $\hat{b}$ is slightly less than b and $\hat{b}x^2$ is a lower estimate for a vector field which approximates F_0 (but going slower). An upper bound for the integral is $-2.5\log(m(a))$ and, hence, the amplification of error is bounded by $m(a)^{-2.5}$. We can proceed in a similar way for the errors originated when we compute $x_2,x_3,\dots$, but a very rough bound as if all errors originate at x_1 is enough. We should multiply by N_1 which can be bounded by $\int_{m(a)}^{m}dx/\hat{b}x^2<1/\hat{b}m(a)$. Finally this error in position should be converted to error in time, but the rough approximating field is $\mathcal{O}(m^2)$, independent of a. Summarizing, the total error introduced in the step 2. is largely bounded by $\mathcal{O}(am(a)^{-3.5})$. This applies for the N_1 and N_{-1} iterates.

Now we should estimate $t(a)$ and bound the errors with respect to the dominant term. The point $F_0^{N_{-1}}(-m)$ is close to $-m(a)$, it can be considered as independent of a and the same thing happens for $F_0^{-N_1}(m)$, close to $m(a)$. As also $m(a)$ can be considered as independent on the concrete value of a for a relatively large range of values of a, we can just compute the time to go from $-m(a)$ to $m(a)$ and modify it by a fixed quantity $\Delta = \mathcal{O}(1)$ with error $\mathcal{O}(a)$. Letting aside Δ the time $t(a)$ is estimated as

$$\int_{-m(a)}^{m(a)} \frac{dx}{h(x)}.$$

The field $h(x)$ can be written as $a + bx^2 + x^3\hat{h}(x)$, where $\hat{h}(x)$ is a analytic function starting at degree 0 (or higher). The integrand in the above integral can be written as

$$\frac{1}{h(x)} = \frac{1}{a+bx^2} - \frac{x^3\hat{h}(x)}{(a+bx^2)^2} + \frac{(x^3\hat{h}(x))^2}{(a+bx^2)^3} + \dots\ .$$

The first part of the integral gives $(\pi - 2\tan^{-1}(\sqrt{a/b}/m(a)))/\sqrt{ab} = \pi/\sqrt{ab} - \mathcal{O}(m(a))$ and this is the dominant part. The other terms involve integrands of the form $x^j/(a+bx^2)^n, n \geq 2, j \geq 3(n-1)$, whose integral is zero if j odd because of the symmetry. The first non-zero integral corresponds to $j = 4, n = 2$ and the value is $2m(a) + \mathcal{O}(a^{1/2})$. That is, there is a part depending on $m(a)$ and the part depending on a tends to zero if $a \to 0$. It is immediate to check that this is also the behavior for all other terms.

The errors due to the difference between F_a and $\varphi^h_{t=1}$ can be bounded by $\mathcal{O}(a^2 t(a))$, negligible in front of terms $\mathcal{O}(a^{1/2})$. Also the errors due to the definition of z can be neglected by the same reason.

Summarizing, the total expression for the error $E(b)$ in time in our estimates, including the non-dominant term in $t(a)$, contains Δ and powers of $m(a)$. The remaining terms are $\mathcal{O}(a^{1/2})$ and $\mathcal{O}(a|\log(a)|^d$ for some positive d. It is clear that for a small enough the dominant part is $\mathcal{O}(a^{1/2})$. We reach the conditions

$$\frac{\pi}{\sqrt{ba^{(k)}_{sni}}} = k - N - E(b) - g_2 + \mathcal{O}((a^{(k)}_{sni})^{1/2}), \qquad \frac{\pi}{\sqrt{ba^{(k)}_{snf}}} = k - N - E(b) - g_1 + \mathcal{O}((a^{(k)}_{snf})^{1/2}).$$

From this i) and ii) follow. It can happen that g has several minima (resp. maxima) at which a saddle-node bifurcation gives rise to (resp. destroys) a sink. The relevant interval is the one corresponding to first creation and last destruction.

To prove iii) we consider that, for $a \in [a^{(k)}_{snf}, a^{(k)}_{sni}]$ we are looking for a fixed point z^* of a map of the form $z \to z + g(z) - \gamma$ for $\gamma \in [g_1, g_2]$, that is $g(z^*) = \gamma$. The stability is given by $1 + dg/dz(z^*)$ plus corrections which tend to zero as $a \to 0$. Hence, the minimum multiplier tends to $1 + \min_{z\in[0,1]} dg/dz(z)$. □

As an illustration of the results of proposition B.1 we consider the Arnold map on the circle [57] that we write in the form

$$F_a(x) = x + a + b(1 - \cos(x)),$$

perhaps the simplest example satisfying the conditions (18). For a fixed value $b = 0.8$ we have computed domains of a for which periodic sinks are found. The results are shown in Fig. 42 left for a wide range of the period k.

Concretely in Fig. 42 left we plot, as a function of $\log(k)$,

1. The value of $\log(a^{(k)}_{snm}) + 2\log(k) - 2.5$, seen as the lower curve. The value $a^{(k)}_{snm}$ is the mean value between $a^{(k)}_{sni}$ and $a^{(k)}_{snf}$. The term -2.5 has been added to display the three lines in a suitable vertical range.

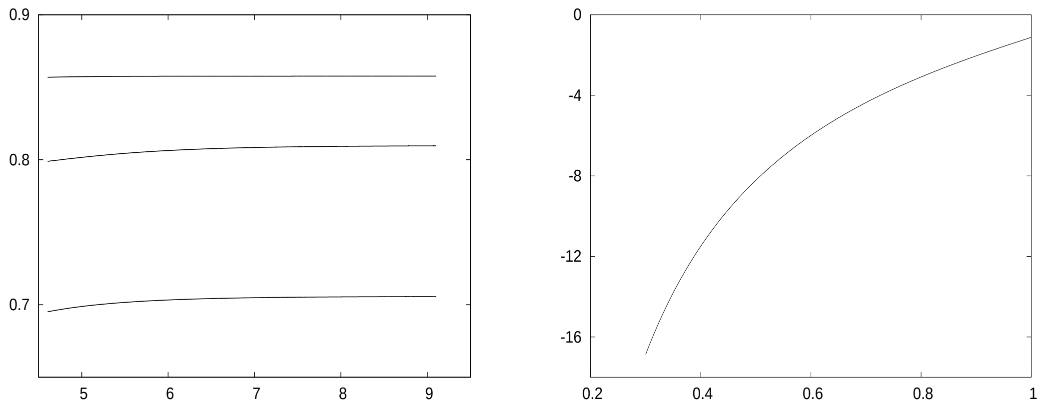

Figure 42: An illustration of the accumulation and scaling of sinks near a saddle-node for the Arnold map of the circle. Left: limit behavior of $(a_{sni}^{(k)}+a_{snf}^{(k)})/2$, $a_{sni}^{(k)}-a_{snf}^{(k)}$ and the minimum of the eigenvalue in a sink interval as a function of $\log(k)$. See the text for details. Right: the behavior of the amplitude $\Delta g = g_2 - g_1$ of the g function as a function of b. The variables plotted are $b, \log(\Delta g)$.

2. The value of $\log(\Delta a_{sn}^{(k)}) + 3\log(k)$, seen as the middle curve, where $\Delta a_{sn}^{(k)} = a_{sni}^{(k)} - a_{snf}^{(k)}$.
3. The value of the multiplier for $a \in [a_{snf}^{(k)}, a_{sni}^{(k)}]$ at which it reaches a minimum, seen as the upper curve.

The three lines show clearly the tendency to a limit.

On the right part of Fig. 42 we display the amplitude $\Delta g = g_2 - g_1$ of g as a function of b. To this end, given a value of b we have computed a point x_0, close to $m = 0.01$, such the image under F_0^{n+1} is $-x_0$. Hence, the interval $[x_0, F_0^n(x_0)]$ is mapped to $[F_0^{-1}(-x_0), -x_0]$ under F_0^n. A high order vector field $x' = h(x)$ (depending on b) has been obtained so that for $x \in (-\tilde{m}, \tilde{m})$, with $\tilde{m}$ slightly larger than m, $\varphi_{t=1}^h(x)$ coincides with $F_0(x)$ except by tiny roundoff errors (below 10^{-16}). Then we follow the procedure described before to obtain g. Given $z \in [0,1]$ we compute $\tilde{z}$ such that $\varphi_{t=\tilde{z}}(F_0^{-1}(-x_0)) = F_0^n(\varphi_{t=z}(x_0))$ and define $g(z) = \tilde{z} - z$. The extreme values of g, g_1 and g_2, as defined above, have been computed and this gives Δg. The plot shows $\log(\Delta g)$ as a function of b.

The expected result is to have a dominant term in Δg of the form $\exp(-c/b)$ for some constant $c > 0$. This follows from the standard time-periodic suspension and averaging technique (see again [55]). Indeed, the map F_0 differs from the identity by $\mathcal{O}(b)$ and it can be approximated by an autonomous flow up to $\exp(-c/b)$ terms. If we only consider the autonomous flow effect one would have $g(z) = 0$. The exponentially small terms are the responsible of having $g(z) \neq 0$. As shown in [33] upper bounds for these terms are related to the closest singularity to the real axis of the solutions, in our case of the limit scaled field $x' = 1 - \cos(x)$, which tend to the critical point $x = 0$. If the distance from the singularity to the real axis is δ then $c = 2\pi\delta$. In general the real bounds are close to the upper ones, as discussed at the Appendix in [22], where a method to check this condition is also presented. In the present example the closest singularity has imaginary part equal to 1. Hence, it should not be seen as a surprise that, with the data displayed in Fig. 42 right the values of $-b\log(\Delta g)$, when fitted by polynomials of increasing order, give an independent term which approaches 2π.

Similar examples with functions $f(x)$ which are not even have been also considered, with the same kind of results.

References

[1] A.A. Andronov and L.S. Pontryagin. *Coarse systems.* Doklady Akademii Nauk SSSR, 1937, 14(5), 247–250.

[2] A.A. Andronov, E.A. Leontovich, I.I. Gordon and A.G. Mayer. *Qualitative Theory of the Second Order Dynamical Systems.* Nauka, Moscow, 1966 (in Russian). [Engl.transl.: Israel program of sci. transl., Jerusalem, 1971].

[3] A.A. Andronov, E.A. Leontovich, I.I. Gordon and A.G. Mayer. *Theory of Bifurcations of Dynamical Systems on a Plane.* Nauka, Moscow, 1967 (in Russian). [Engl.transl.: Israel program of sci. transl., Jerusalem, 1973].

[4] A.A. Andronov and A.A. Vitt. *Zur Theorie des Mitmehmens von van der Pol.* Atch. Elektrotech., 1930, 16(4), 280–288.

[5] L.P. Shilnikov, A.L. Shilnikov, D.V. Turaev and L.O. Chua. *Methods of qualitative theory in nonlinear dynamics.* Part I, World Scientific, 1998; Part II, World Scientific, 2001.

[6] H. Dulac. *Sur les cycles limites.* Bull. Soc. Math. France, 1923, 51, 45–188.

[7] E.A. Leontovich. *On a birth of limit cycles from a separatrix loop.* Soviet Math. Dokl., 1951, 78(4), 641–644.

[8] E.A. Leontovich. *Birth of limit cycles from a separatrix loop of a saddle of a planar system in the case of zero saddle value.* Preprint VINITI, 1988, 114 (in Russian).

[9] R. Roussarie. *On the number of limit cycles which appear by perturbation of separatrix loop of planar vector fields.* Bol.Soc. Math. Brasil, 1986, 17(2), 66–101.

[10] D.V. Turaev. *On a case of bifurcations of a contour composed by two homoclinic curves of a saddle.* Methods of the qualitative theory of differential equations, Ed. Gorki, 1984, 162–175.

[11] D.V. Turaev. *On bifurcations of dynamical systems with two homoclinic curves of the saddle.* Ph.D. Thesis, Nizhny Novgorod State University, 1991.

[12] M.V. Shashkov and D.V. Turaev. *On the complex bifurcation set for a system with simple dynamics.* Int. J. Bifurcation and Chaos, 1996, 13(2), 175–182.

[13] D.V. Turaev and L.P. Shilnikov. *On bifurcations of a homoclinic figure-eight for a saddle with a negative saddle value.* Soviet Math. Dokl., 1987, 44(2), 422–426.

[14] V.S. Afraimovich and L.P. Shilnikov. *On small periodic perturbations of autonomous systems.* Soviet Math. Dokl., 1973, 5, 734–742.

[15] V.S. Afraimovich and L.P. Shilnikov. *The annulus principle and problems on interaction of two self-oscillation systems.* Prikladnaja Matematica i Mekhanika, 1977, 41, 618–627.

[16] V.S. Afraimovich and L.P. Shilnikov. *Invariant two-dimensional tori, their breakdown and stochasticity.* Methods of the qualitative theory of differential equations, Ed. Gorki, 1983, 3–26. English translation in Am. Math. Soc. Transl. Ser. 2, 149 (1991), 201–212.

[17] H. Broer, C. Simó and J.C. Tatjer. *Towards global models near homoclinic tangencies of dissipative diffeomorphisms.* Nonlinearity, 1998, 11, 667–770.

[18] A.L. Shilnikov, L.P. Shilnikov and D.V. Turaev. *On some mathematical topics in classical synchronization.* Bifurcation and Chaos, 2004, 14, 2143–2160.

[19] A.D. Morozov and L.P. Shilnikov. *Towards mathematical theory of synchronization of oscillations.* Soviet Math. Dokl., 1975, 223(6), 1340–1343.

[20] A. Neishtadt. *Passage through a separatrix in a resonance problem with slowly-varying parameter.* Appl. Math. Mech., 1975, 39(4), 594–605.

[21] A. Neishtadt. *Passing through resonances in a two-frequency problem.* Dokl. Akad. Nauk SSSR, 1975, 221(2), 301–304

[22] C. Simó and A. Vieiro. *Dynamics in chaotic zones of area preserving maps: close to separatrix and global instability zones.* Phys. D, 2011, 240(8), 732–753.

[23] J. Guckenheimer and P. Holmes. *Nonlinear Oscillations, Dynamical Systems and Bifurcations of Vector Fields.* Springer-Verlag, New York, 1988.

[24] S. Wiggins. *Introduction to Applied Nonlinear Dynamical Systems and Chaos.* Springer-Verlag, New York, 1990.

[25] A. Litvak-Hinenzon and V. Rom-Kedar. *Symmetry breaking perturbations and strange attractors.* Phys. Rev. E, 1997, 55(5), 4964–4978.

[26] M. Bosch, C. Simó. *Attractors in a Shilnikov-Hopf scenario and a related one-dimensional map.* Physica D, 1993, 62, 217–229.

[27] J.P. Carcassès, C. Mira, M. Bosch, C. Simó and J.C. Tatjer. *"Crossroad area-spring area" transition (I). Parameter plane representation.* Int. J. Bifur. and Chaos, 1991, 1(1), 183–196.

[28] J.P. Carcassès, C. Mira, M. Bosch, C. Simó and J.C. Tatjer. *"Crossroad area-spring area" transition (II). Foliated parametric representation.* Int. J. Bifur. and Chaos, 1991, 1(2), 339–348.

[29] G.M. Zaslavsky and N.N. Filonenko. *Stochastic instability of trapped particles and conditions of applicability of the quasi-linear approximation.* Sov. Phys.-JETP, 1968, 27, 851–857.

[30] B.V. Chirikov. *A universal instability of many-dimensional oscillator system.* Phys. Rep., 1979, 52, 264–379.

[31] G.N. Piftankin and D.V. Treschev. *Separatrix maps inHamiltonian systems.* Russian Math. Surveys, 2007, 2(62), 219–322.

[32] C. Simó and A. Vieiro. *Some remarks on the abundance of stable periodic orbits inside homoclinic lobes.* Phys. D, 2011, 240(24), 1936–1953.

[33] E. Fontich and C. Simó. *The Splitting of Separatrices for Analytic Diffeomorphisms.* Erg. Th. & Dyn. Systems, 1990, 10, 295–318.

[34] N.K. Gavrilov and L.P. Shilnikov. *On three-dimensional dynamical systems close to systems with a structurally unstable homoclinic curve.* Part 1, Math.USSR Sb., 1972, 17, 467–485 ; Part 2, Math.USSR Sb, 1973, 19, 139–156.

[35] S. Newhouse and J. Palis. *Cycles and bifurcation theory.* Astérisque, 1976, 44–140.

[36] O.V. Stenkin and L.P. Shilnikov. *Homoclinic Ω-explosion and hyperbolicity domains.* Math. Sbornik, 1998, 189(4), 125–144.

[37] K. Alligood, E. Sander and J. Yorke. *Explosions: global bifurcations at heteroclinic tangencies* Ergod. Th. & Dynam. Sys., 2002, 22, 953–972.

[38] S.V. Gonchenko and O. Stenkin. *Homoclinic Ω-explosion: hyperbolicity intervals and their bifurcation boundaries.* To appear in the book "Nonlinar Dynamics: new approaches" (Springer, 2012).

[39] S.V. Gonchenko. *On a two parameter family of systems close to a system with a nontransversal Poincaré homoclinic curve. I.* Methods of Qualitative Theory of Differential Equations; Ed. Gorky St. Univ., 1985, 55–72. English transl. in: Selecta Math. Sovietica, 1990, 10.

[40] S.V. Gonchenko and A. Komlev Yu. *Bifurcations and chaos in cubic maps of the plane.* Methods of Qualitative Theory of Differential Equations; Ed. Gorky St. Univ., 1988, 33–40 (in Russian).

[41] J.C. Tatjer. *Bifurcations of codimension two near homoclinic tangencies of second order.* In Proceedings of the European Conference on Iteration Theory, 1992, 306–318, World Sci. Publishing, Teaneck,NJ.

[42] S.V. Gonchenko, L.P. Shilnikov and D.V. Turaev. *On models with non-rough Poincaré homoclinic curves.* Phys. D, 1993, 62(1-4), 1–14.

[43] S.V. Gonchenko, L.P. Shilnikov and D.V. Turaev. *Homoclinic tangencies of an arbitrary order in Newhouse domains* Itogi Nauki Tekh., Ser. Sovrem. Mat. Prilozh., Temat. Obz., 1999, 67, 69–128 ; English transl. in J.Math.Sci., New York, 2001, 105(1), 1738–1778.

[44] P.M. Cincotta, C.M. Giordano and C. Simó. *Phase space structure of multidimensional systems by means of the Mean Exponential Growth factor of Nearby Orbits (MEGNO).* Physica D, 2003, 182, 151–178.

[45] F. Ledrappier, M. Shub, C. Simó and A. Wilkinson. *Random versus deterministic exponents in a rich family of diffeomorphisms.* J. Stat Phys., 2003, 113, 85–149.

[46] L.J. Díaz, I.L. Rios and M. Viana. *The intermittency route to chaotic dynamics.* In Global Analysis of dynamical systems, Taylor & Francis 2001, Chapter 11, 309–327.

[47] L.J. Díaz, J. Rocha and M. Viana. *Strange attractors in saddle-node cycles: prevalence and globality.* Inv. Math., 1996, 125, 37–74.

[48] M. Hénon. *A two-dimensional mapping with a strange attractor.* Comm. Math. Phys., 50(9), 1976, 69–77.

[49] M. Benedicks and L. Carleson. *The dynamics of the Hénon map* Ann. of Math. (2), 133(1), 1991, 73–169.

[50] L. Mora and M. Viana. *Abundance of strange attractors* Acta Math., 1993, 171, 125–150.

[51] C. Simó. *On the Hénon-Pomeau attractor* J. Stat Phys., 1979, 21, 465–494.

[52] S.V. Gonchenko, L.P. Shilnikov and D.V. Turaev. *Dynamical phenomena in systems with structurally unstable Poincaré homoclinic orbits.* Interdisc. J. Chaos, 1996, 6(1), 15–31.

[53] S.V. Gonchenko and L.P. Shilnikov. *Invariants of* Ω*-conjugacy of diffeomorphisms with a structurally unstable homoclinic trajectory.* Ukrainian Math. J., 1990, 42(2), 134–140.

[54] S.V. Gonchenko, L.P. Shilnikov and D.V. Turaev. *On dynamical properties of multidimensional diffeomorphisms from Newhouse regions.* Nonlinearity, 2008, 21, 923–972.

[55] H. Broer, R. Roussarie and C. Simó. *Invariant circles in the Bogdanov-Takens bifurcation for diffeomorphisms.* Ergod. Th. & Dynam. Sys., 1996, 16, 1147–1172.

[56] A.I. Neishtadt. *The separation of motions in systems with rapidly rotating phase.* Prikladnaja Matematika i Mekhanika, 1984, 48, 133–139.

[57] V.I. Arnold. *Small denominators I.* Transl. Amer. Math. Soc. 2nd. series, 1965, 46, 213–284.